Measurement of the W boson charge asymmetry in proton-proton collisions at $\sqrt{s} = 8$ TeV and developments towards the upgrade of the ATLAS Muon Spectrometer

Tai-Hua Lin

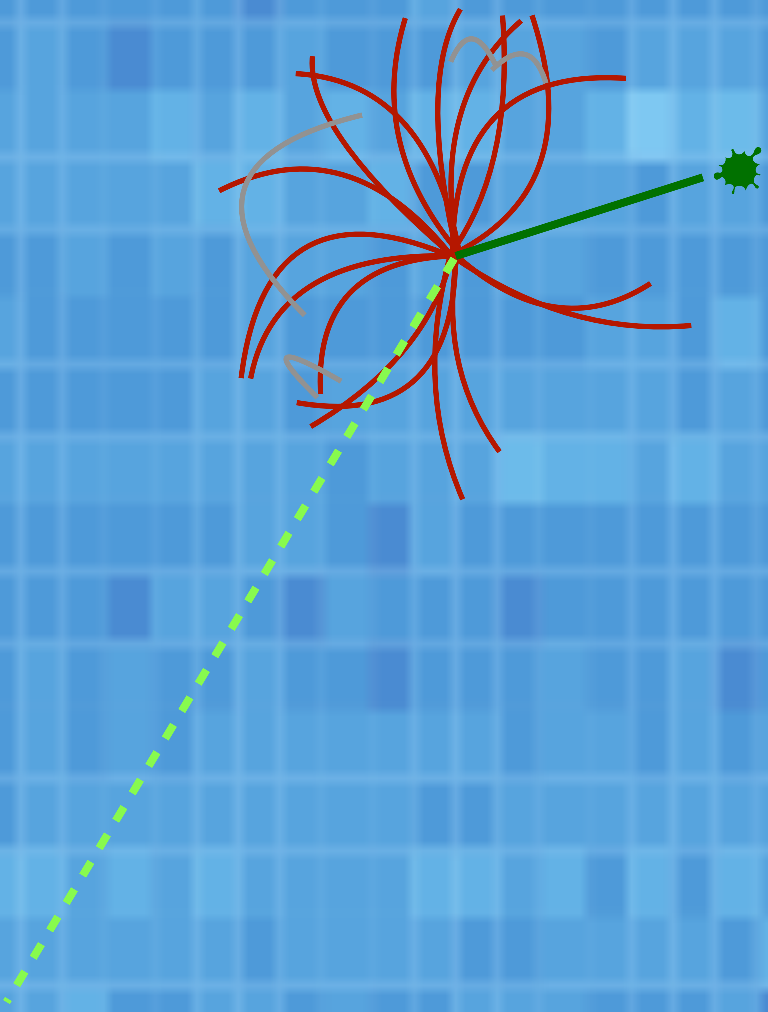

Johannes Gutenberg-Universität Mainz

Measurement of the W boson charge asymmetry in proton-proton collisions at $\sqrt{s} = 8$ TeV and developments towards the upgrade of the ATLAS Muon Spectrometer

Dissertation
zur Erlangung des akademischen Grades doctor rerum naturalium
(Dr. rer. nat.)
im Fach Physik
eingereicht an der
Johannes Gutenberg-Universität Mainz
von

Tai-Hua Lin

Doktorprüfung am 5 März 2018

Abstract

The measurement of the W boson production cross-section in proton proton collisions at the Large Hadron Collider (LHC) provides an excellent probe of the structure functions of the proton. In this thesis, a first measurement of this production cross-section in the muon decay channel at a centre of mass energy of 8 TeV with the ATLAS detector is presented.

Special attention is drawn to the resulting charge asymmetry, which has been derived as a function of the muon pseudorapidity. This constrains significantly the u and d quark momentum fractions in the proton, thus providing an important input for several high precision measurements, conducted at the LHC. The overall muon charge asymmetry from the W boson yields $A_\mu = 0.18263 \pm 0.00147(\text{syst.}) \pm 0.00021(\text{stat.})$, which is the most precise measurement at the LHC using one single decay channel.

In order to allow for similar high precision measurements during the high luminosity phase of the LHC after 2020, the muon system of the ATLAS detector has to be upgraded, especially the forward region of the muon detector. Therefore prototype detectors for this upgrade project have been developed, constructed and tested. Results of the construction process and the relevant performance studies are also presented here.

Zusammenfassung

Die Messung des W-Boson-Produktionsquerschnitts bei Proton-Proton-Kollisionen am Large Hadron Collider (LHC) liefert eine hervorragende Möglichkeit die Strukturfunktionen des Protons zu untersuchen. In dieser Arbeit wird eine erste Messung des Produktionswirkungsquerschnitts im Myon-Zerfallkanal von W-Bosonen in Proton-Proton Kollisionen bei einer Schwerpunktsenergie von 8 TeV mit dem ATLAS Detektor vorgestellt.

Besonderes Augenmerk wird auf die daraus resultierende Ladungsasymmetrie gelegt, die als Funktion der Myon-Pseudorapidity abgeleitet wurde. Dies beschränkt signifikant die Impulsanteile des u- und d-Quarks im Proton, sodass wichtige Grundlagen für mehrere hochpräzise Messungen, die am LHC durchgeführt werden, gelegt werden können. Die gesamte Ladungsasymmetrie des Myons aus der W Boson Produktion ergibt sich zu $A_\mu = 0.18263 \pm 0.00147(\text{syst.}) \pm 0.00021(\text{stat.})$, was die bisher genauste Messung am LHC in diesem Zerfallskanal ist.

Um in der Hochluminositätsphase des LHC nach dem Jahr 2020 ähnliche Hochpräzisionsmessungen zu ermöglichen, muss das Myonsystem des ATLAS-Detektors, vor allem im Vorwärtsbereich, aufgerüstet werden. Deshalb wurden im Rahmen dieser Arbeit Prototyp-Detektoren für solche Anwendungen konstruiert und getestet. Es werden auch die Ergebnisse des Bauprozesses und die relevanten Leistungsstudien dargestellt.

Contents

1 Introduction

> *There is nothing new to be discovered in physics now. All that remains is more and more precise measurement. ... Beside two little dark clouds on the clear blue sky of physics.*[a]
>
> — **mis-attributed to Lord Kelvin,**
> Nineteenth-Century Clouds over the
> Dynamical Theory of Heat and Light
>
> ---
>
> [a] These two clouds (ether + ultraviolet catastrophe) turned out to bring the new physics of the 20th century: the theory of relativity and quantum mechanics.

Most physics analyses at the Large Hadron Collider (LHC) concentrate on the direct search for physics signatures beyond the Standard Model. Since no striking hints for such new particles or interactions have been found in recent years, precision measurements come more and more into the focus of research efforts. One of the most prominent examples is the precision measurement of the W boson mass, which has been recently published by the ATLAS Collaboration, yielding a value of $m_W = 80370 \pm 19$ MeV [11]. Together with the knowledge of the masses of the Z boson, the Higgs boson and the top-quark as well as the precise value of the electroweak mixing angle, the internal consistency of the Standard Model can be tested. Deviations of the expected relations would reveal physics beyond the Standard Model in an indirect way.

In order to improve the precision on m_W, the structure functions of the proton have to be known to highest precision. In particular, the knowledge of the momentum fractions of the u and d quarks within the proton has to be enhanced. One possible approach to achieve such improvement, is a precision measurement of the charge dependent production cross-section of W bosons in proton proton collisions at the LHC. In particular, the angular dependence on the W boson production plays here a crucial role.

Within this thesis, the first measurement of the $W^{\pm}$ production cross-section at a centre of mass energy of 8 TeV has been performed, using the full data-set of the year 2012, recorded by the ATLAS detector. The final results of this measurement are currently being prepared for publication.

In order to efficiently select W boson candidate events in the available data-set, the $W \rightarrow \mu\nu$ decay channel has been chosen. While the ATLAS detector can directly reconstruct the kinematics of the muon, the situation is more complicated in the case of the neutrino. Here, a quantity commonly known as missing transverse energy, $E_{\mathrm{T}}^{\mathrm{miss}}$, has to be introduced, which uses the calorimetric information of the ATLAS detector. In this thesis, new algorithms for the reconstruction of $E_{\mathrm{T}}^{\mathrm{miss}}$ have been developed and extensively tested. They also built the basis for the previously mentioned W boson mass measurement.

The precision of the W boson charge asymmetry measurement can be further improved during the high luminosity run of the LHC. However, here an upgrade of the ATLAS muon detector must first be installed in 2018. Within this thesis, significant contributions to the design, the construction and the tests of a new prototype detector for this upgrade project have been made. These have been published in a reviewed journal article. [72]

The thesis is structured as follows: In Section 2, a brief introduction to the theoretical description of the W boson production in proton proton collisions is given. In Section 3 the Large Hadron Collider, as well as the ATLAS detector is described, followed by an introduction to the physics objects and the data-sets that have been used in this thesis. The newly developed algorithms for the reconstruction of $E_{\mathrm{T}}^{\mathrm{miss}}$ are summarized in Section 4. The actual analysis and measurement of the W boson charge asymmetry is discussed in Section 5. Section 6 summarizes the construction and the performance tests of the prototype detector for the new small wheel. The thesis concludes with Section 7, where a brief outlook is also given.

2

The Standard Model

2.1 Overview

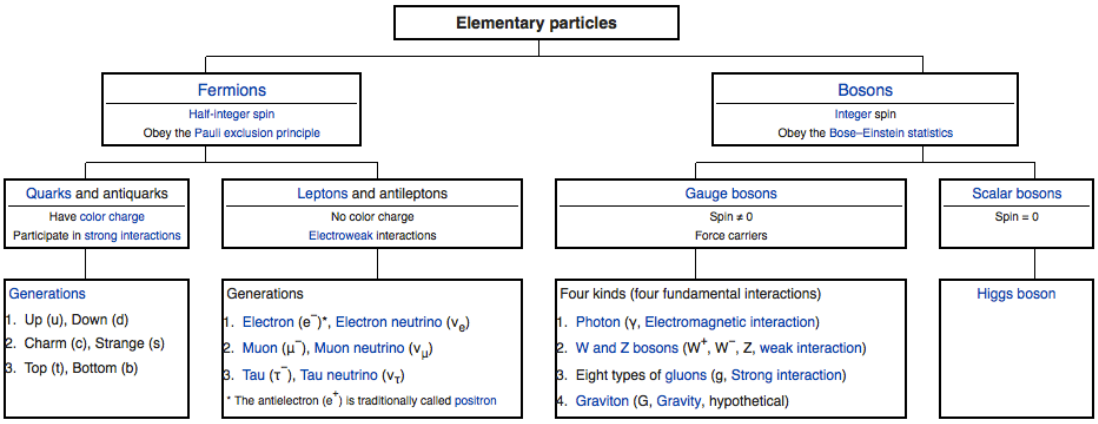

Figure 2.1: The overview of elementary particles within the Standard Model [98]

A brief introduction in the Standard Model of particle physics is described in the following. A more detailed reference can be found in Reference [94].

The Standard Model of particle physics classifies all of the elementary particles and their interactions via the electromagnetic, weak and strong forces. The elementary particles can be categorised by their spin into two groups, bosons and fermions. Fermions are the particles with odd half integer spin (so obey the Pauli exclusion principle) and they are the building blocks of all matter. Bosons are the force carriers that mediate the strong, weak, and electromagnetic fundamental interactions and have integer spin.

The matter particles can be categorised by which forces they interact with: quarks participate in the strong and the electroweak interactions, while leptons interact only via the electroweak force, i.e. the combination of electromagnetic and weak force. The force carrier for the electromagnetic interaction is the photon; the carriers for the weak force are the $W^{\pm}$ and Z bosons; for the strong interaction they are the gluons. Some extended theories try to describe gravity within the same framework and predict a graviton as a mediator. However, those quantum gravity theories often have serious theoretical problems and hence are not part

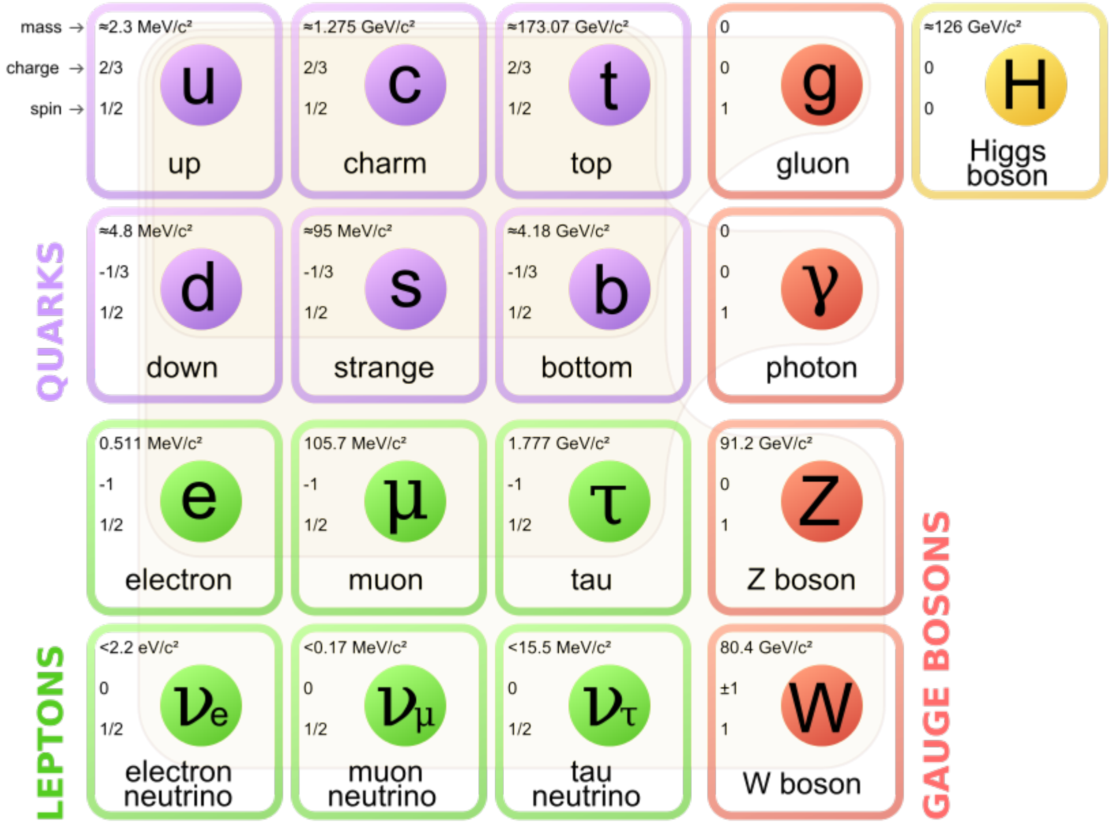

Figure 2.2: The building block of the Standard Model. [98]

of the Standard Model of Particle Physics. The categorisation of the elementary particles is shown in Fig. 2.1 and a summary of the building blocks is shown in Fig. 2.2.

Particles that interact with the electromagnetic force carry electric charge. For the strong interaction, a somewhat analogous property (or quantum number), named colour charge is introduced. All quarks and gluons carry a colour charge, but in nature these are always found in bound states which are "colourless" or "white". Also all free particles in nature are "colourless".

The quarks form composite particles, so called hadrons. These can be divided into two types: baryons and mesons. Three quarks (or three anti-quarks) in a bound state together are called baryons, and a quark and anti-quark pair is called a meson. Exotic mesons which composed of four quarks were discovered at LHCb in 2016, so called tetraquarks, which is different to the default definition of a meson which is formed by a quark and anti-quark pair. [4]

The proton bound state is composed of two valence up quarks and one valence down quark with an electric charge of 1. The neutron bound state has one valence up quark and two valence down quarks with 0 electric charge. The structure of the proton depends on the energy scale at which it is probed. Further details will be described in the following sections.

2.2 W Boson Production at the LHC and Parton Distribution Functions

The proton structure can be probed via its interactions with other particles - either with leptons as in deep inelastic scattering experiments [84] or with other protons as at the LHC. The production of the W boson from the proton proton collisions at the LHC is the key to resolving the proton's constituents. A diagram illustrating the production of the W boson from a proton proton collision is shown in Fig. 2.3, and is known as the Drell-Yan processes.

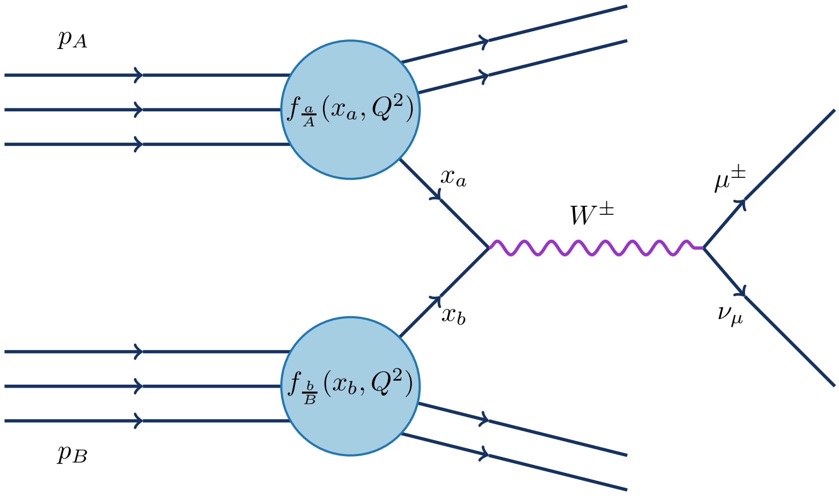

Figure 2.3: The production of the W boson from a proton (p$_A$) proton (p$_B$) collision at the LHC. $f_{\frac{a(,b)}{A(,B)}}(x_{a(,b)}, Q^2)$ are the parton distribution functions which define the probability to find a parton of a certain momentum fraction $x_{a(,b)}$ in the proton p$_{A(,B)}$.

The momentum transfer between the proton and the probe is usually expressed by Q. For low momentum transfer between the proton and the probe ($Q \lessapprox 1$GeV), the proton behaves like a point-like particle and its substructure cannot be resolved. The static properties like electric charge, quantum numbers are determined by the three valence quark point-like constituents. With higher momentum transfers ($Q > 1$GeV), finer aspects of the proton structure can be resolved. The gluons which are emitted from the valence quarks can split into quark and anti-quark pairs, so-called sea quarks. The valence quark from one proton and the anti-sea quark from another proton can interact and produce the W boson. Most of the W^+ bosons are produced with one up quark and an anti-down quark; most of the W^- boson are produced with one down quark and an anti-up quark at the LHC. Therefore measuring the ratio of the production of W^+ and W^- boson can help us to understand the details of the proton structure. [77]

In order to qualitatively measure the proton structure, the square of the momentum transfer between two protons at the LHC, Q^2 is defined as the scale of the hard scattering process, which is directly related to the momenta of the incoming partons and the W mass (M_W^2) in the case of W boson production:

$$Q^2 = sx_a x_b = M_W^2 \tag{2.1}$$

where x_a and x_b are the momentum fractions of hadron A and B carried by partons a and b, respectively. $\sqrt{s}$ is the centre of mass energy of the colliding beam.

The fraction of momentum carried by a given parton when expressed as a probability distribution, is called a parton distribution function (PDF). The probability to find a parton (a) of a certain momentum fraction x_a of the proton p_A is expressed by $f_{\frac{a}{A}}(x_a, Q^2)$, and is the mathematical term of the parton distribution function. The PDF of parton b is labelled as $f_{\frac{b}{B}}(x_b, Q^2)$.

To calculate the production cross section of the W boson, the factorization theorem which was first postulated by Drell and Yan is used. [52] [77] In hadronic collisions, the production cross section can be described by the product of two terms: a high energy regime and a low energy regime. For the larger momentum transfers of the proton and proton interactions at short distances (the high energy regime), the interaction of two protons can be evaluated using perturbative QCD calculations. And for the lower momentum transfers of the protons interaction at the long distance (the low energy regime), parton distribution functions (PDFs) are used to describe the proton structure in a phenomenological way as the perturbative QCD calculations are no longer applicable.[88] Further details about PDFs are given in the next section.

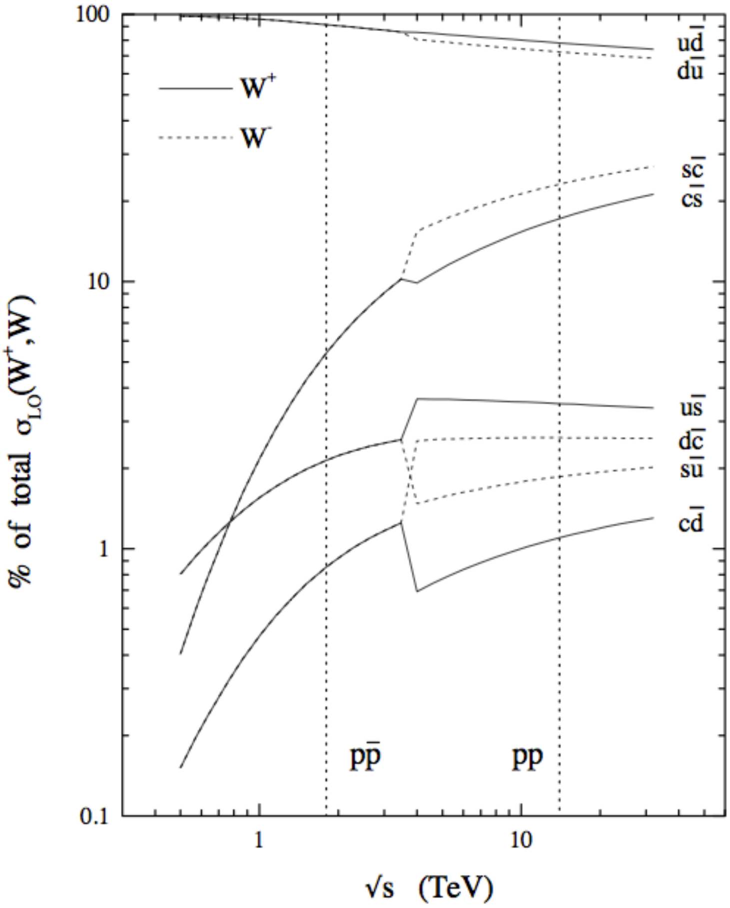

Figure 2.4: The total cross section in proton-proton and proton-antiproton collisions as a function of the centre of mass energy at the leading order in perturbative QCD. The different parton flavour decomposition of the W^+ and W^- is shown. [76]

The calculation of the W boson production cross section using the factorization theorem is shown in Equ. 2.2:

$$\sigma(pp \rightarrow W+X) = \sum_{n=0}^{\infty} \alpha_s^n(\mu_R^2) \int dx_a dx_b f_{\frac{a}{A}} \left(x_a, \mu_F^2\right) f_{\frac{b}{B}} \left(x_b, \mu_F^2\right) \times \hat{\sigma}^n_{ab \rightarrow W+X} \left(x_a x_b s, \mu_R^2, \mu_F^2\right) \tag{2.2}$$

where $f_{\frac{a}{A}}$ and $f_{\frac{b}{B}}$ are the PDFs for parton a (or b) in hadron A (or B). The partonic cross section is expressed by: $\hat{\sigma}^n_{ab \rightarrow W+X}$. The somewhat arbitrary factorisation and renormalisation scales are typically set to the W mass, $\mu_F = \mu_R = m_W$. This calculation of the W boson production is available up to the next to next leading order accuracy (NNLO) or $\alpha_s^2(\mu_R^2)$.

Figure 2.5: The first order W boson production for $W^+ \to \mu^+\nu$ and $W^- \to \mu^-\bar{\nu}$

The W boson production in high energy proton-proton collisions at the LHC with the ATLAS detector is studied to understand the previously mentioned properties of the proton. Fig. 2.4 shows the contributions to the total cross section from the various sub-production processes at leading order from the annihilation of quark-antiquark pairs. The charge of the W boson depends on the incident partons. The requirement of charge conservation leads to an interaction between an up-type and a down-type quark. The valence-sea scattering of up and down quarks are the dominant mechanism for W production in proton proton collisions, $u\bar{d} \to W^+$ for positive charge production and $d\bar{u} \to W^-$ for negative charge production. The production process of the W boson at leading order (tree level) is shown in the Feynman diagram in Fig. 2.5

The second most dominant process is the sea-sea scattering of charm and strange quarks which forms about 10% of the total cross section of W bosons at leading order. The contribution from the valence-sea scattering of up and strange quarks and other cross family interactions are Cabibbo suppressed [94] and form a few percent of the total production cross section.

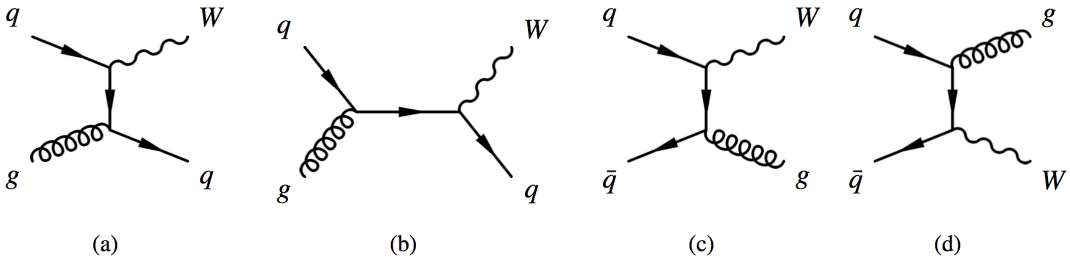

Figure 2.6: The sub-processes of W boson production at next to leading order. [96]

About 30% of the W boson production comes from $gq \to Wg$, $g\bar{q} \to W\bar{g}$ or $q\bar{q} \to Wg$. These sub-processes of W boson production at next to leading order with the associated gluon or quark emission are shown in Fig. 2.6. The emission of gluons and other strongly interacting particles can be observed as the non-zero transverse momentum of W bosons ($p_{T,w}$) which is peaked at a few GeV with a tail to the higher values of the spectrum. [96], [88]

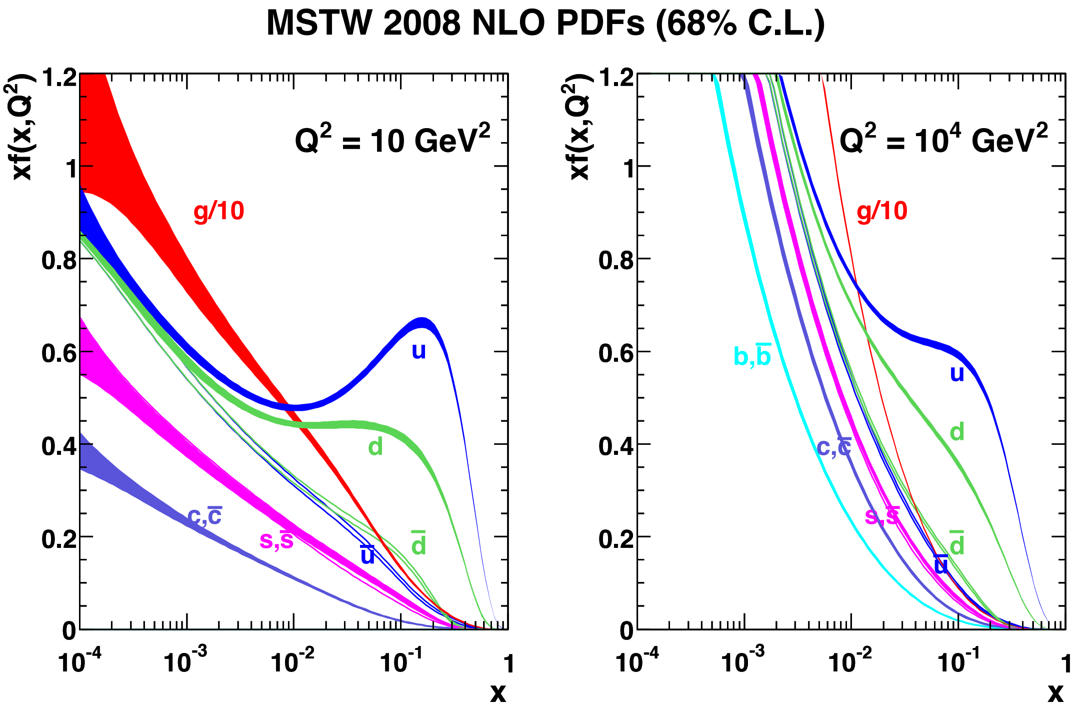

Figure 2.7: The probability to find a given quark or gluon species inside the proton is shown in the parton distribution function at the momentum transfer scale Q as a function of the fraction x of the proton energy carried by the parton. [75]

By summing over all contribution of partons, all the quantum numbers of the proton must be recovered: charge 1, baryon number 1, strangeness 0. The sum rules express the requirement of the net number of each valence quark:

$$\begin{aligned}
\int_0^1 [u(x) - \bar{u}(x)] &= 2 \\
\int_0^1 \left[d(x) - \bar{d}(x)\right] &= 1 \\
\int_0^1 [s(x) - \bar{s}(x)] &= 0
\end{aligned} \tag{2.3}$$

where $u(x) = u_v(x) + u_s(x)$ and $d(x) = d_v(x) + d_s(x)$, v represents the valence quark and s the sea quark. The functions $u(x)$, $d(x)$ and $s(x)$ are the probability distribution of the up quark, down quark and strange quark respectively.

As mentioned PDFs must be obtained phenomenologically from data using a global fit. There are several fits which relay on different assumptions and data from different experiments, such as CT10, CT14, NNPDF, and MSTW. [60] [55] [58] [75]

The results of the PDF from the MSTW 2008 fitting group are shown in Fig. 2.7. Two different energy scales are simulated with Q^2 = 100 GeV^2 and Q^2 = 10000 GeV^2. The structure of the proton is seen to depend on the energy scale. The contribution to the PDF from sea quarks and gluons increases with higher energy, especially at the low x-fraction. Since the LHC is a proton proton collider the quark is usually valence and so has a higher momentum fraction and the anti-quark comes from the sea and so has a lower momentum fraction. Therefore at least one of the partons should carry a significant fraction of the momentum of the proton. Therefore the production process usually involves a valence quark.

2.3 W Boson Charge Asymmetry

The production of a positively charged W boson (W^+) mainly depends on the annihilation of an up quark (u) in one proton and an anti-down quark ($\bar{d}$) in another proton. In the case of the production of the negatively charged W boson (W^-), it mainly depends on the annihilation of a down quark (d) in one proton and an anti-up quark ($\bar{u}$) in the other proton.

Due to the differences between the u quark and d quark momentum distributions in the proton there results a difference (or asymmetry) in the production cross sections of the W^+ and W^-. Almost all the W bosons are produced with some boost due to conservation of momentum and there being a higher momentum fraction of the valence quarks than the sea quarks. In the case of W^+, the valence quark (up quark) carries more momentum than the sea quark (anti-down quark), $x(u) > x(\bar{d})$, therefore W^+ are produced preferentially in the direction of the up quark. And in the case of the W^-, the down quark carries more momentum than the anti-up quark, $x(d) > x(\bar{u})$, therefore W^- are produced preferentially in the direction of the down quark. A longitudinal boost of the W boson can be expressed using "rapidity": $y_{W^+} = (1/2)\text{ln}(x(u)/x(\bar{d}))$ and $y_{W^-} = (1/2)\text{ln}(x(d)/x(\bar{u}))$. [77] For the proton-proton collisions, there are more up quarks produced than down quarks. Therefore the asymmetry between the cross-sections will vary as a function of the rapidity (a detailed definition is given in Sec. 3.2.1) of the W boson. More

W^+ bosons will be observed in higher rapidity regions than W^-. Experimentally the rapidity is not a well-measured quantity due to the unobserved neutrino. Therefore the pseudorapidity (η_μ) of the decay lepton can be taken as a proxy observable. The details of the experimental measurement will be described in Sec. 5.

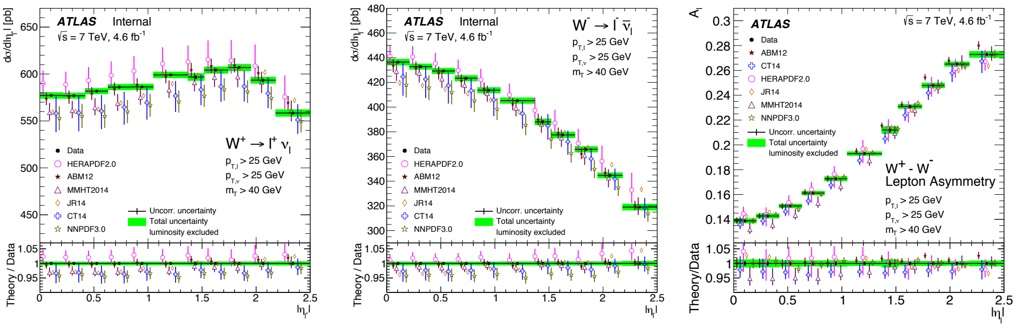

(a) $W^+ \to \mu^+\nu$ Fidu. XSec (b) $W^- \to \mu^-\bar{\nu}$ Fidu. XSec (c) W Charge Asymmetry

Figure 2.8: The fiducial cross section ($W^+ \to \mu^+\nu$ and $W^- \to \mu^-\bar{\nu}$) and W charge asymmetry was performed at a centre of mass energy of 7 TeV at the ATLAS experiment. [34]

The previous measurement of the W charge asymmetry as a function of η_μ at the LHC was performed at a centre of mass energy of 7 TeV as shown in Fig. 2.8(c). Fig. 2.8(a) and Fig. 2.8(b) show the fiducial cross sections of W^+ and W^- as functions of η_μ . The production rate of W^+ is relatively higher in the larger η_μ region than of W^- as shown in Fig. 2.8(c). In this thesis the very first results at a higher collision energy and with higher statistics is performed. Measurements of the W charge asymmetry had also been performed in proton and anti-proton collisions at a $\sqrt{s} = 1.96$ TeV using the D0 Detector at the Tevatron. [68] For the measurement at the Tevatron, there is no overall W^+ and W^- asymmetry, but one can be observed as a function of the decay lepton pseudorapidity. W^+ bosons are preferentially boosted in the proton direction and W^- bosons are preferentially boosted in the anti-proton direction at D0/CDF.

2.4 Monte Carlo event generators

Several general purpose Monte Carlo generators are used for comparison to the measured data in this thesis, like PowhegPYTHIA 8 [10] [9] [90] , and SHERPA. [83] Both PowhegPYTHIA 8, and SHERPA use the CT10 PDF-sets [87] and use a leading order calculation which is combined with a higher order pertubative QCD correction. SHERPA also includes the effects of a multiparton hard process with a multijet final state. Those Monte Carlo generators provide fully exclusive simulations of high energy particles collisions. Monte Carlo generators are built from several components which describe the physics starting from short distance scales up to the scale of hadron formation and decay. The physics components of the short distance (higher momentum transfer) can be reliably computed in QCD perturbation theory. The implementation of primary-hadron decays into stable ones is based on the hadronization models. Monte Carlo event generators include in addition soft hadron physics models for the underlying events and minimum-bias interactions. A review of Monte Carlo Event generator programs used at the LHC is detailed in Reference [39].

The ATLAS Experiment

3

3.1 LHC

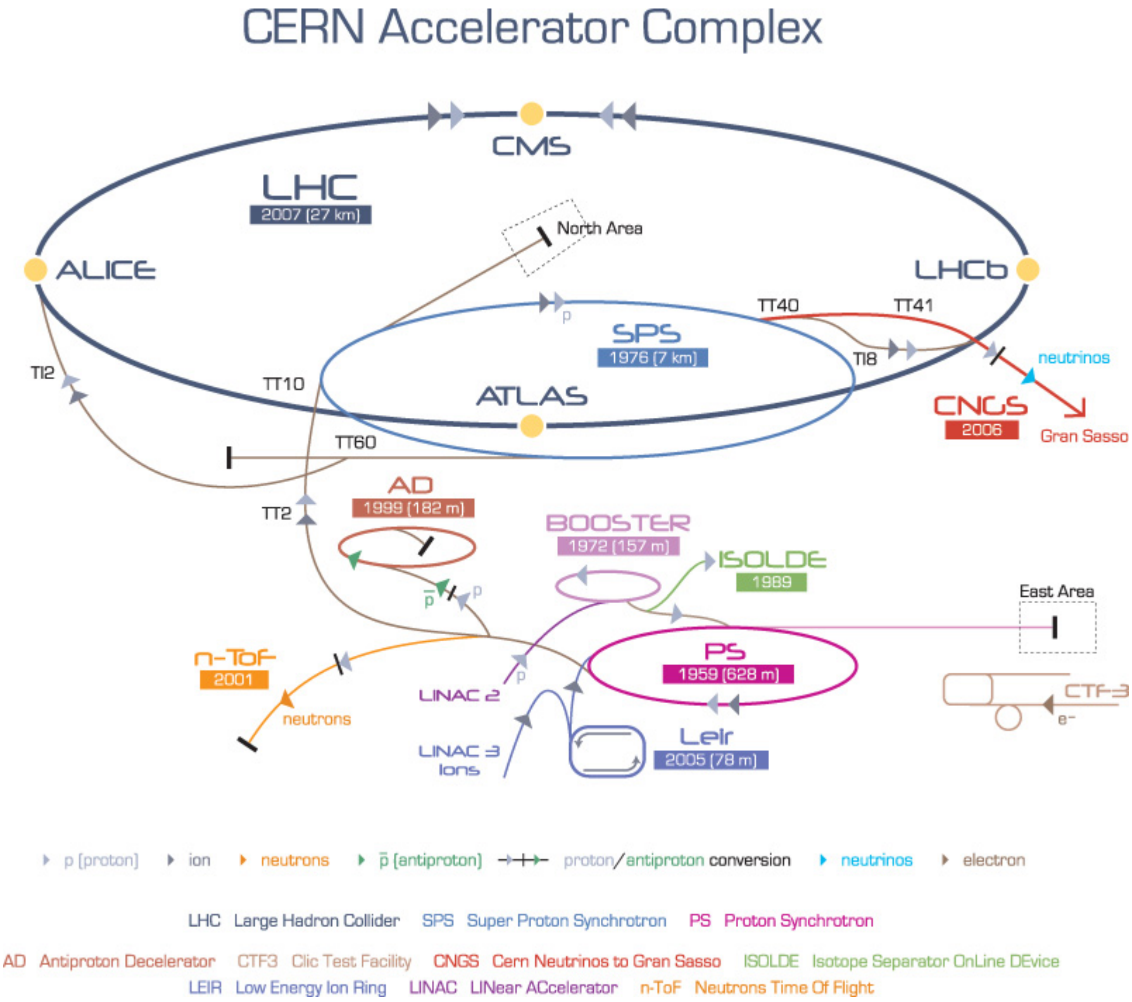

Figure 3.1: Schematic diagram of the LHC. [71]

The scientific purpose of the LHC (Large Hadron Collider) is to explore the inner structure of matter and the forces that govern its behaviour. Protons or heavy ions (lead) can be accelerated and their energy boosted in a 27 km in circumference ring under ground. The schematic diagram of the LHC is shown in Fig. 3.1. There are four collision points with four different detectors: ATLAS (A Toroidal LHC ApparatuS), CMS (Compact Muon Solenoid detector), LHCb (Beauty Experiment), ALICE (A Large Ion Collider Experiment). In order to collide protons, they have to be generated from hydrogen gas with their electrons removed by passing through an electric field. Protons are accelerated in the order of an linear accelerator (Linac 2), the Proton Synchrotron (PS) and the Super Proton Synchrotron (SPS). Two bunches of protons can collide in the four different interaction points and the particles after collisions can be detected by four different detectors.

3.2 ATLAS Detector

ATLAS is a "onion type" detector with cylindrical and forward-backward symmetry with respect to the interaction point, as shown in Fig. 3.2. Each subdetector is designed to perform a specific task. The purpose is to identify and to precisely measure the energies and momenta of all the particles produced in the proton-proton collisions. [49] The subdetectors from inside to outside are Inner Detector, Calorimetry and Muon Spectrometer.

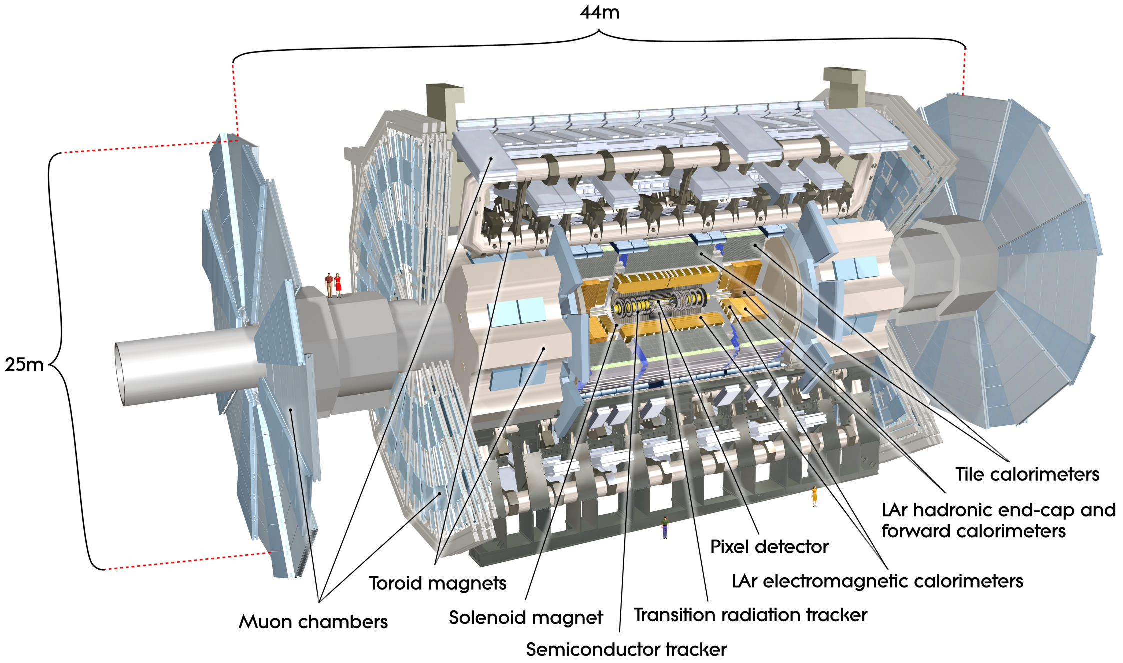

Figure 3.2: Cut-away view of the ATLAS Detector [49]

3.2.1 The Coordinate System

In accelerator physics, the z (longitudinal) axis is usually taken as the axis along the beam pipe and the origin of the coordinate system is set to be at the nominal interaction point. The transverse plane is the plane perpendicular to the beam pipe. The azimuthal angle between the tangent to the track at the distance of closest approach to the origin and the z axis is labelled ϕ. [95] Particles are produced with a range of velocities along the z axis and it is desirable to have measured quantities which are Lorentz invariant to boosts in this direction.

One such quantity is the transverse mass, M_T, which is defined in Equ. 3.1 in terms of the momenta of the particles in the transverse plane (p_x and p_y), and the rest mass, M.

$$M_T^2c^4 = p_x^2c^2 + p_y^2c^2 + M^2c^4 \tag{3.1}$$

The rapidity of a particle, y, is defined in Equ. 3.2 in terms of the energy and momentum along the z-axis, p_z. Differences in rapidity are Lorentz invariant.

$$y = \frac{1}{2}ln\left(\frac{E + p_zc}{E - p_zc}\right) \tag{3.2}$$

The rapidity of the particle produced by the collision can help us to identify the angle and the direction of the emission. [56] When particles with very high energy are produced, most of the momentum is in the transverse plane with relatively little in the z direction. The rapidity approaches zero for these high energy particles. In the case that particles are directed close to the beam pipe, the rapidity approaches to positive or negative infinity as $E \approx \pm p_zc$.

It is difficult to measure the total momentum and energy of a particle precisely and therefore a more convenient measure, the pseudorapidity (η) is introduced and defined in Equ. 3.3 in terms of the polar angle (which can be very precisely measured). For highly relativistic particles (such as electrons or muons) the pseudorapidity and the rapidity are equivalent. A detailed discussion of the relationship between rapidity and pseudorapidity is presented in [56].

$$\eta = -\ln\left(\tan\frac{\theta}{2}\right) \tag{3.3}$$

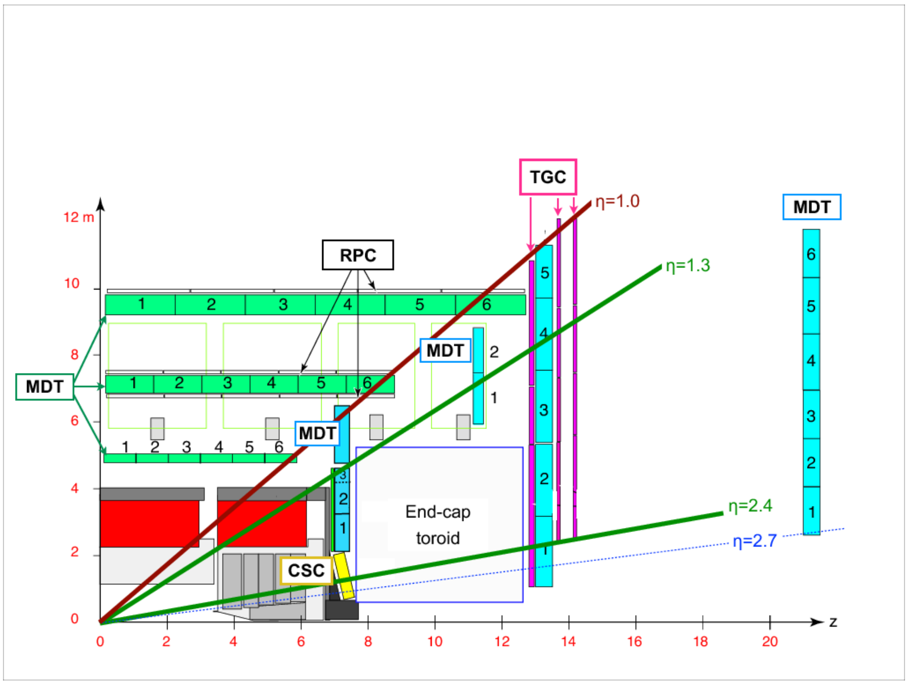

(a) ATLAS η coverage

Figure 3.3: The schematic view for the pseudorapidity coverage for the case of the muon detector [49]

where $\theta = cos\frac{p_z}{p}$ is the angle between the particle track and the beam pipe.

Fig. 3.3(a) shows the coverage of pseudorapidity for the case of the muon spectrometer. The barrel region of the muon detector approximately covers the range $-1 < \eta < 1$.

3.2.2 The Magnet System

Charged particles follow spiraling trajectories in the magnetic field. The measurement of the momenta of these charged particles can determined by the curvature of their trajectories. Then the energies of these charged particles can be derived.

The choice of the magnetic field configuration defines the basic detector design. Two typical magnet configurations are solenoidal and toroidal, which respectively generate parallel and perpendicular magnetic fields relative to the beam axis.

Solenoid for the Inner Detector

The central solenoid provides an axial magnetic field of 2 T for the Inner Detector. In order to place the central solenoid in front of the LAr electromagnetic calorimeter and to achieve the desired calorimeter performance, careful minimization of the material is required. To avoid two vacuum walls, the central solenoid and LAr electromagnetic calorimeter are placed into a single common vacuum vessel. [57]

Toroids for the Muon Detector
The toroidal magnetic field for the muon spectrometer is generated by three air-core toroids (two end-cap toroids and one barrel toroid with magnetic fields of 1 T and 0.5 T respectively).

3.2.3 Inner Detector

The Inner Detector (ID) is used to measure the trajectories of charged particles emerging from the collisions. The ID is designed to provide excellent momentum resolution for charged particles above a given threshold of the transverse momentum p_T and provide the sign of their charges. The high tracking ability of the ID can distinguish between the primary and the secondary vertices where a particle produced in a collision further decays into a new set of particles.

The particle flux decreases from the particle source, varying from hit rates of $10^8 \text{cm}^{-2}\text{s}^{-1}$ at a radius of $r = 50.5$ mm (innermost layer of the Pixels); to 5×10^6 $\text{cm}^{-2}\text{s}^{-1}$ at $r = 299$ mm (innermost layer of the SCT); and 5×10^5 $\text{cm}^{-2}\text{s}^{-1}$ at $r = 1000$ mm (end of TRT), as shown at Fig. 3.4. [46]

The layout of the Inner Detector, as shown in Fig. 3.5, covers the pseudorapidity (see Equ. 3.3) region $|\eta| < 2.5$.

Pixel Detectors There are three layers of silicon pixel detectors which provide the highest detection granularity in the innermost part of ATLAS. The pixel sensors are 250 μm thick silicon detectors using oxygenated n-type wafers with readout pixels on the n^+-implanted [1] side. The nominal pixel size is 50×400 μm^2 resulting in an estimated particle occupancy[2] of 10^{-4} per pixel and LHC bunch crossing. There are approximately 80 million readout channels. [49] [92]

---

[1] The n^+-implants allow the detector to operate with good charge collection efficiency after type inversion, even below the depletion voltage, because the depletion zone grows from the pixel side.

[2] Particle occupancy is the average fraction of collisions in which a signal channel registers a signal

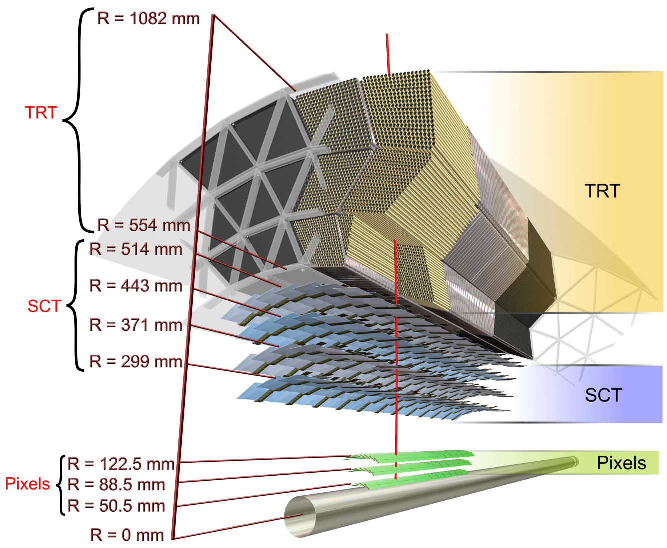

Figure 3.4: The ATLAS inner tracking system [49]

Semiconductor Trackers (SCT) The Semiconductor Tracker uses silicon microstrips for tracking the charged particles. There are four cylindrical double layers of silicon microstrips sensors. A silicon microstrips layer consists of two single-sided p-in-n sensors which are glued back to back (one axial and one with 40 mrad stereo angle) with AC-coupled readout strips. The strip pitch was determined by the required digitising precision, granularity, particle occupancy and noise performance. To maintain an adequate noise performance after degradation due to radiation damage, the silicon sensors (both of the pixel detectors and the SCT) must be kept at a low temperature to keep the leakage current low (approximately –5 to +10^{o}C). [30]

Transition Radiation Tracker (TRT) In the outermost region of the ID, the transition radiation tracker is used, which consists of gaseous straw tube detectors. There are on average 36 axial straws (which means each track traverses approximately 36 axial straws) of 4 mm diameter contained in the barrel TRT modules within their support structure. Each straw is a small cylindrical gas-containing chamber, with an anode wire in the center, and the wall of straw acting as a cathode. The straw is filled with a Xenon-based gas mixture. Apart from tracking, the TRT is capable of identifying particles, particularly electrons and pions. [49]

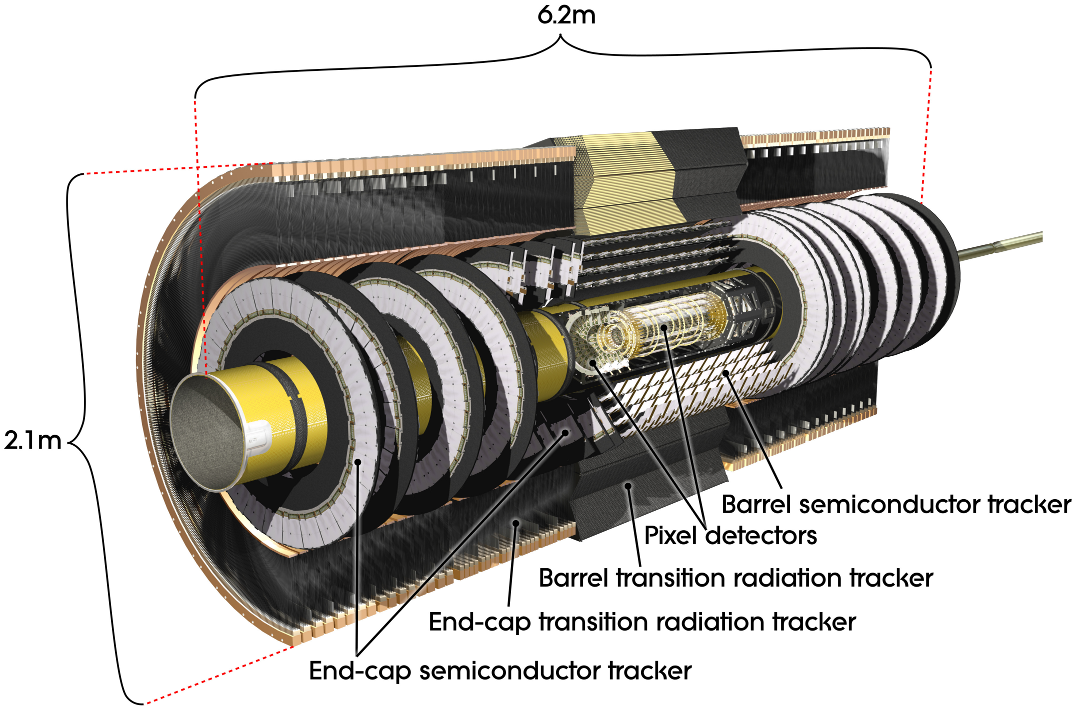

Figure 3.5: The ATLAS Inner Detector [49]

3.2.4 Calorimetry

Outside the Inner Detector, the next layers are the sampling calorimeters[3], which are used to measure the energies of the incident particles. The principle of calorimetry is the incident particle interacts with a shower material or absorber and produces a shower of secondary particles. The calorimeters provide good containment for electromagnetic and hadronic showers, and also limit punch-through, which means particles leaking out of the calorimeter, into the muon system.

Electromagnetic Calorimeter The electromagnetic calorimeter is a lead/liquid-argon (LAr) detector covering the pseudorapidity region of $|\eta| < 1.475$ for the barrel and $1.375 < |\eta| < 3.2$ for the two end-caps. When high-energy electrons, photons or other neutral particles pass through the lead, an electromagnetic shower is produced whose intensity is proportional to the incident energy. The active material, argon, is ionized by the shower and produces a current which is also proportional to the energy of the incoming particle. [49]

---

[3] Sampling calorimeter made of alternating layers of passive(absorber)/active(decector) materials.

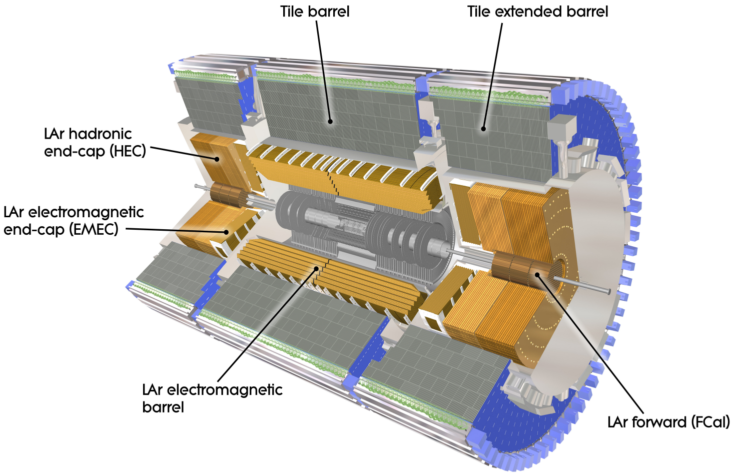

Figure 3.6: The ATLAS calorimetry [49]

Hadronic Calorimeters The hadronic calorimeters measure energies of all hadronic particles in clusters. In ATLAS, there are three different types of hadronic calorimeters:

- Tile Calorimeter, Tiles are the scintillating plastic plates used as the sampling materials in this sub-detector. Steel plates are used as the absorbing material. The tile calorimeter is located in the barrel region in a pseudorapidity range $|\eta| < 1.7$.

- Hadronic End-cap Calorimeter (HEC), for the hadronic end-cap calorimeter, copper is used as the absorbing material and liquid argon is used as the sampling material. The HEC is located in the end-cap region in a pseudorapidity range $1.5 < |\eta| < 3.2$.

- Forward Calorimeter (FCal), two different materials are used for absorbing in the forward calorimeter. Copper is used in the central region which is near the interaction points for electromagnetic measurements. Tungsten is used in the outer region for hadronic energy measurements. Liquid argon is used for sampling materials in the whole FCal with pseudorapidity coverage $3.1 < |\eta| < 4.9$. [49]

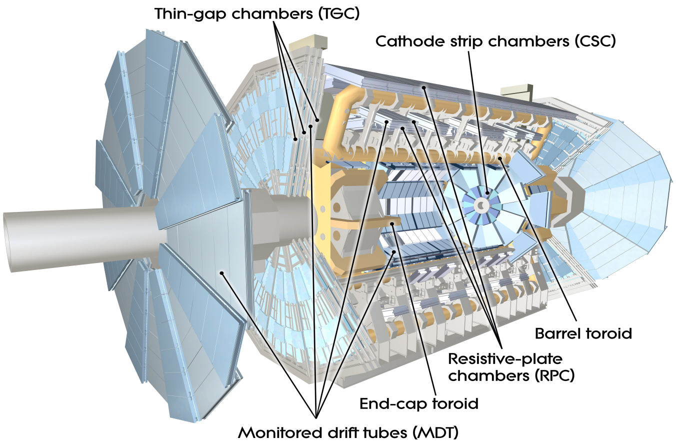

Figure 3.7: The ATLAS Muon Spectrometer [49]

3.2.5 Muon Spectrometer

The Muon spectrometer is designed to identify, trigger and accurately measure the momenta of muons. A high magnetic field is necessary for good muon momentum resolution and triggering capability. The Muon Spectrometer is the outermost part of the ATLAS detector and is composed of four main parts.

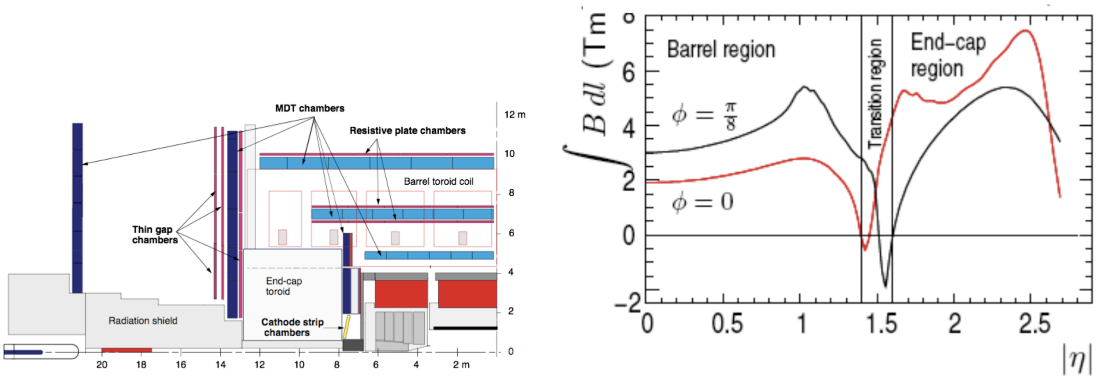

(a) Cross Section

(b) Magnetic Field

Figure 3.8: A cross section of the all muon sub-detectors in x-y view is shown in the left plot. The magnetic field distribution of the muon detector as a functions of η is shown in the right plot. The transition region between end-caps and barrel is around $1.2 < |\eta| < 1.7$ [82]

- **Monitored Drift Tube Chambers (MDTs):** The monitored drift tube chambers measure the precise track coordinates which are required to get the momentum in both the barrel and end-cap regions.

- **Cathode Strip Chambers (CSCs):** The cathode strip chambers complement the higher pseudorapidity region of MDTs.

- **Resistive Plate Chambers (RPCs):** Resistive Plate Chambers covering a pseudorapidity region $|\eta| < 2.4$ are used in the barrel region as the trigger system to select events with muon candidates.

- **Thin Gap Chambers (TGCs):** Thin Gap Chambers are the trigger chambers used in the end-cap regions where they have to sustain higher particle rates.

Fig. 3.8(a) shows the positions of the four different muon sub-detectors and their relative position from the toroid. There are three layers of the tracking detector (MDTs and CSCs) for precise momentum measurements. Then there are two different fast trigger chambers (RPCs and TGCs) for muon triggering. Air-core toroids are used to minimise the effect from multiple scattering. The resolution of the muon momentum is degraded in the transition region between barrel and end-cap as shown in Fig. 3.8(b) due to the low magnetic field integration. [82]

3.2.6 Trigger and Data Acquisition

At a bunch crossing rate of 40 MHz and an average of 23 inelastic proton-proton interactions per bunch crossing, raw data is generated at a rate of 60 TB/s while the rate for event storage is 200 Hz (the average event size is around 1MB) [57]. The online data acquisition system must reduce the rate of incoming raw data by at least three orders of magnitude.

Therefore a trigger system is needed to select all good event candidates, reject most of the background events and be flexible for new physics [38]. The Data Acquisition System (DAQ) is responsible for buffering the event data from the readout electronics at the level 1 trigger accept (L1A) rate. The ATLAS trigger system has three levels, level 1 trigger, level 2 trigger and event filter.

Level 1 Trigger (L1)

The L1 trigger is implemented using custom-made electronics. It uses algorithms to search for signatures from high-p_T muons, electrons/photons, jets and τ-leptons decaying into hadrons. The L1 Trigger also selects events with large $E_{\mathrm{T}}^{\mathrm{miss}}$ and large total transverse energy. The detector readout system works in two steps:

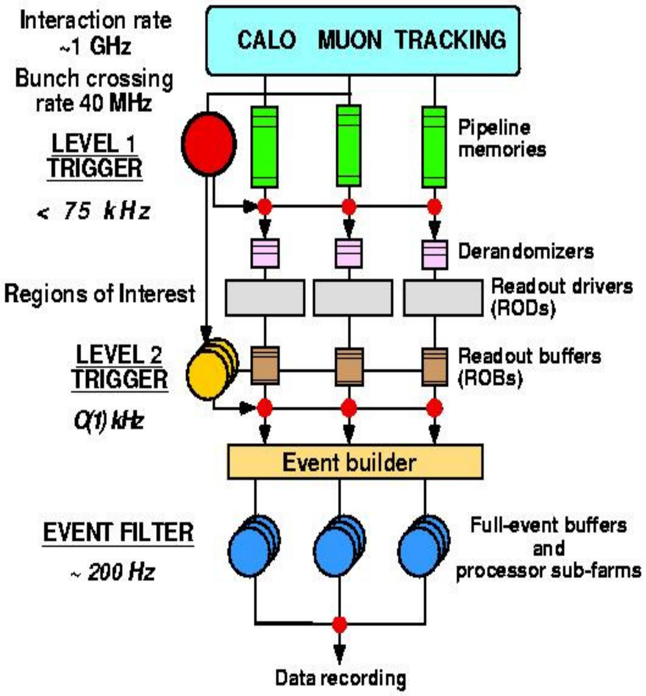

Figure 3.9: Block diagram of the ATLAS Trigger system [49]

1. L1 accepts events, sends L1A (Level 1 Accepted). The maximum L1A rate is 75 kHz.

2. define the region of interest (RoI).

The L1 decision must reach the front-end electronics within 2.5 μs after the bunch-crossing time.

Level 2 Trigger (L2) and **Event Filter (EF)**
The L2 and EF together form the High-Level Trigger (HLT), which is based on commercially available computers and networking hardware. The L2 trigger uses the Regions-of-Interest (RoI) from L1 to limit the amount of data transferred from the detector readout. The EF uses offline analysis procedures on fully-built events to further reduce the event rate which then is recorded for subsequent offline analysis.

3.2.7 Physics Objects

The decay products of the proton-proton collisions can be reconstructed from the signals they leave in the ATLAS sub-detectors described in the previous sections. These reconstructed decay products are classified into different families called “physics objects”. [45] An overview of the physics objects which can be used for physics data analysis is shown in Fig. 3.10.

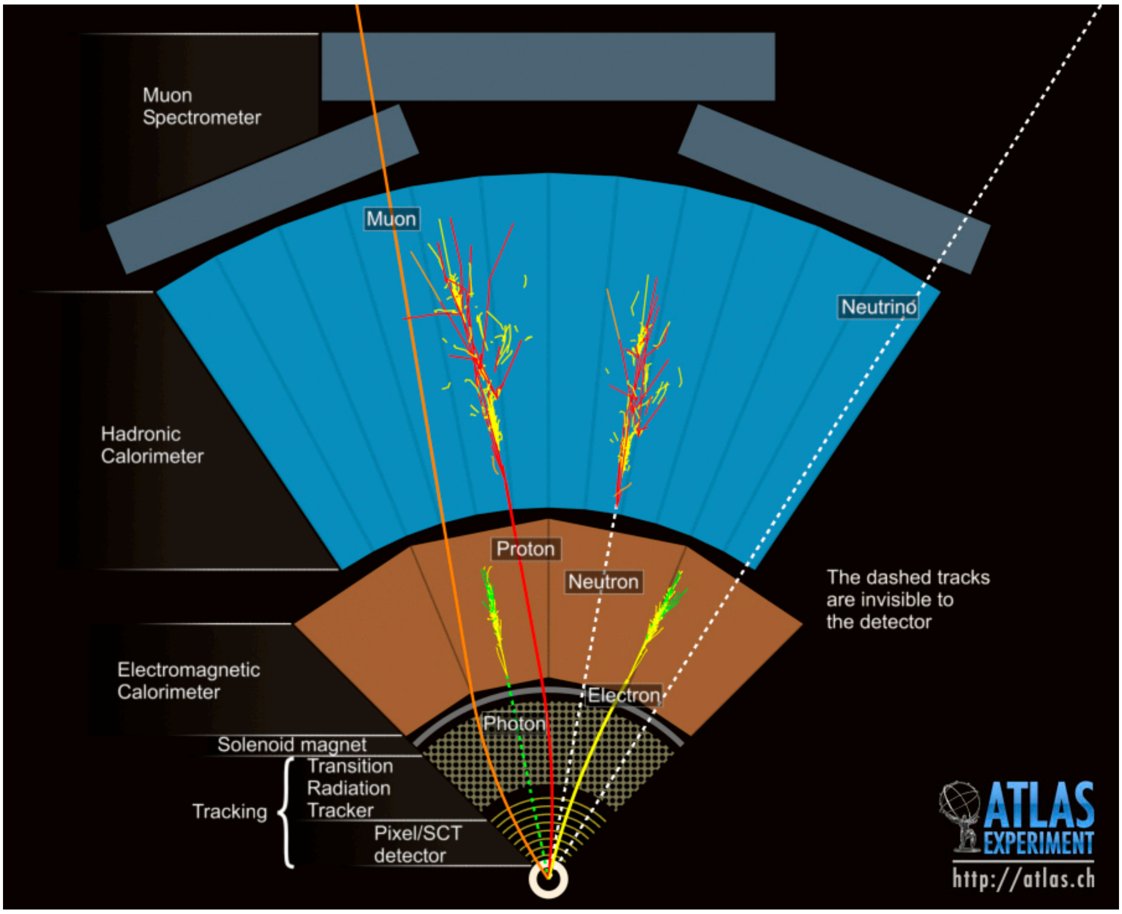

Figure 3.10: An overview of the physics objects that can be reconstructed in the ATLAS detector. [49]

The six main physics objects generally used in analyses are Inner Detector tracks, calorimeter clusters, particle jets, electrons, muons and $E_{\mathrm{T}}^{\mathrm{miss}}$. These are each described in more detail below:

- **Inner detector tracks:** All charged particles leave tracks in the inner detector, which are reconstructed from the individual interactions (hits) the particle makes with each detector element. The transverse momentum of the charged particle can be determined from the curvature of the

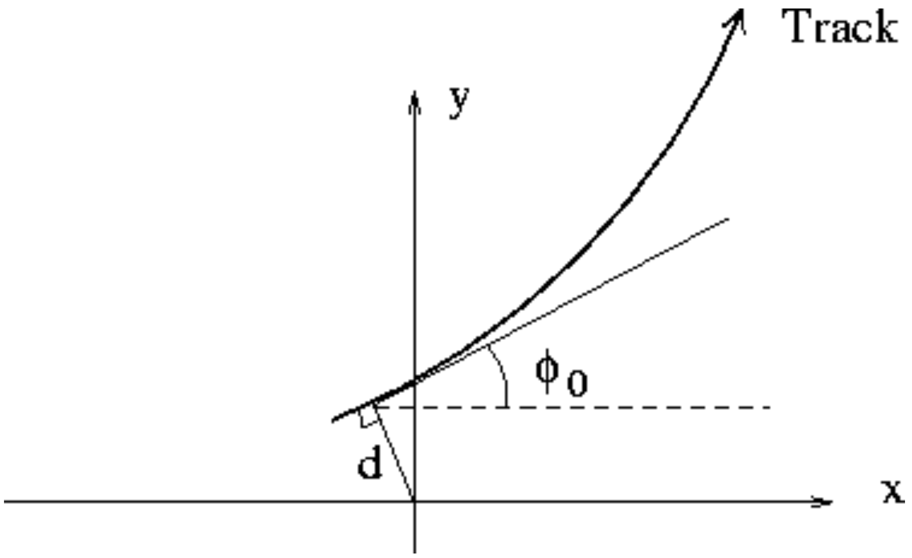

(a) Track Geometry

Figure 3.11: A schematic sketch of the definition of the track geometry [95]

track in the magnetic field. The charge of the particle is then determined from the direction of the curvature of the track. Tracks originating from a similar point in the detector are associated to a common vertex using an iterative vertex finding algorithm using information on track position, curvature and transverse momentum. The vertex with the largest sum of track transverse momentum is labelled the primary vertex. [48] [97] For the track of the charge particle, d_0 is defined as the nearest distance between track and the primary vertex and z_0 is defined as the distance between the track and the primary vertex projected along the beam pipe (z-axis), as shown in Fig. 3.11(a).

- **Clusters:** Some particles, e.g. electrons and photons, deposit most of their energy while they pass through the calorimeter cells in the lateral and longitudinal directions. A group of these energy deposits is called a cluster. Calorimeter cells are combined topologically. A three dimensional group of cells is clustered from a seed cell. The seed cell is defined as the cell with energy four times higher than the noise, and the secondary cells are all cells adjacent to the seed cell. The energy of secondary cells have to be at least two times higher than the noise. [89] The energy of the cluster is the sum of deposited energy in these calorimeter cells and is calibrated using the energy outside the cluster and dead material in the calorimeter. Two cluster calibration methods are commonly used: the local hadron calibration (LC) and electromagnetic (EM) calibration. [70]

- **Particle jets:** Quarks and gluons hadronise forming "jets" of particles in the detector. These jets are reconstructed with clusters measured in the electromagnetic and hadronic calorimeter using one or more jet finding algorithms. Jets with the algorithm, *AntiKt4LCTopo* [42], are used for all the studies in this thesis. *AntiKt4LCTopo* jets are reconstructed from three-dimensional topological clusters of the energy deposits in the calorimeter using the anti-k_t algorithm [42] with distance parameter R = 0.4. The local cluster weighting (LCW) calibration is used to account for different calorimeter responses to electrons, photons and hadrons. A jet energy scale (JES) correction is also applied to correct for jet-level effects by restoring the energy of reconstructed jets to that of the MC generator-level jets. [18] The probability that a jet originated from the primary vertex is assessed using an index called the jet vertex fraction (JVF), which is defined in Equ. 3.4. This is a measure of how much of the jet's momentum originated from tracks associated to the primary vertex.

$$\mathrm{JVF} = \frac{\sum_{\text{PV tracks in jet}} p_{\mathrm{T}}{}^{\text{track}}}{\sum_{\text{All tracks in jet}} p_{\mathrm{T}}{}^{\text{track}}} \tag{3.4}$$

- **Electrons:** The electrons are reconstructed both with tracks registered in the inner detector and clusters in the electromagnetic calorimeter. The momentum and the geometric information are combined using information from both sub-detectors.

- **Muons:** The muons are constructed with the inner detector (ID) tracks and the tracks reconstructed in the muon spectrometer (MS), sometimes with the additional information of the energy deposited in the electromagnetic calorimeter.

  There are four types of reconstructed muons used in ATLAS analyses [23].

  - ⋆ Combined: muon tracks exist both in the ID and the MS.

  - ⋆ Segment tagged: muon tracks exist in the ID and are extrapolated to match one local track segment in the MS. Those muons usually have low transverse momentum or are in the barrel to end-cap transition range.

- Standalone: muon tracks exist only in MS which extends the coverage to $|\eta| < 2.7$.

- Calo-tagged: muon tracks exist in the ID and their energy deposited in the Calorimeter is matched to the muon minimum ionization energy.

Two main algorithms are commonly used at ATLAS to combine and reconstruct the four types of muons for physics analysis. These are the "staco" and "third-chain" [23] muon algorithms. The performance of the "staco" and "third-chain" muon algorithms is shown in Fig. 3.12. Two "dips" are observed in the pseudrapidity plots. At pseudrapidity η_μ =0, it is the feet region of the ATLAS detector where there is no full ϕ coverage. The transition region between barrel and end-cap is found at pseudorapidity $\eta_\mu = \pm 1$. The non-uniform shape of the muon pseudorapidity distribution is due to the rapidity distribution of Z boson events, which have been used in the corresponding Monte Carlo sample for this Figure.

In order to check the performance of the two different algorithms, a selection of the Z boson decaying to two muons is chosen as the two muons can be very well identified. The rapidity and pseudorapidity are chosen as the parameter of interest as they are the relevant parameters for the W charge asymmetry analysis. The data and Monto Carlo show better agreement for the "third-chain" muon algorithm than the "staco" algorithm. The third-chain algorithm was newly introduced for 8 TeV analyses, and is a combination of the various algorithms used at 7 TeV. The difference between the two algorithms is shown in Fig. 3.13. The two algorithms agree to within 5%. The "third-chain" muon algorithm is chosen for the studies of missing transverse momentum and W charge asymmetry in this thesis.

- $E_{\mathrm{T}}^{\mathrm{miss}}$: The missing transverse momentum is reconstructed using the concept of momentum conservation in the transverse plane. $E_{\mathrm{T}}^{\mathrm{miss}}$ is created when a produced particle passes through the detector without

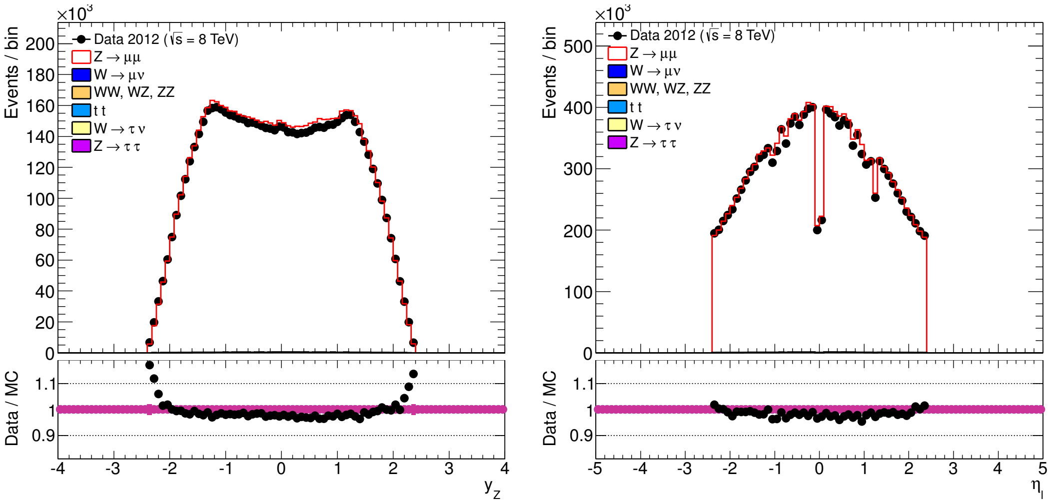

(a) Staco Muon Rapidity (b) Staco Muon Pseudorapidity

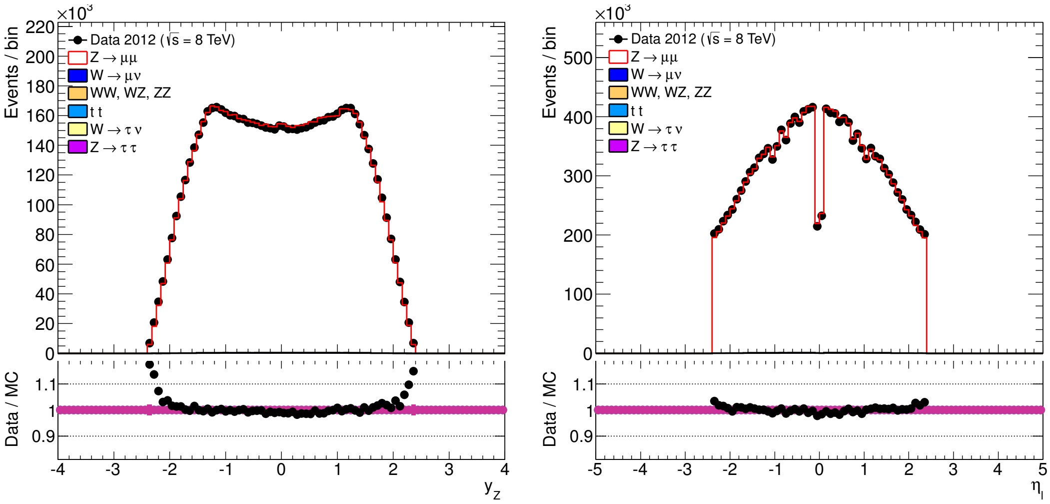

(c) Third Chain Muon Rapidity (d) Third Chain Muon Pseudorapidity

Figure 3.12: Control plots after $Z \to \mu\mu$ event selection to show the performance of the staco and third chain muon algorithms.

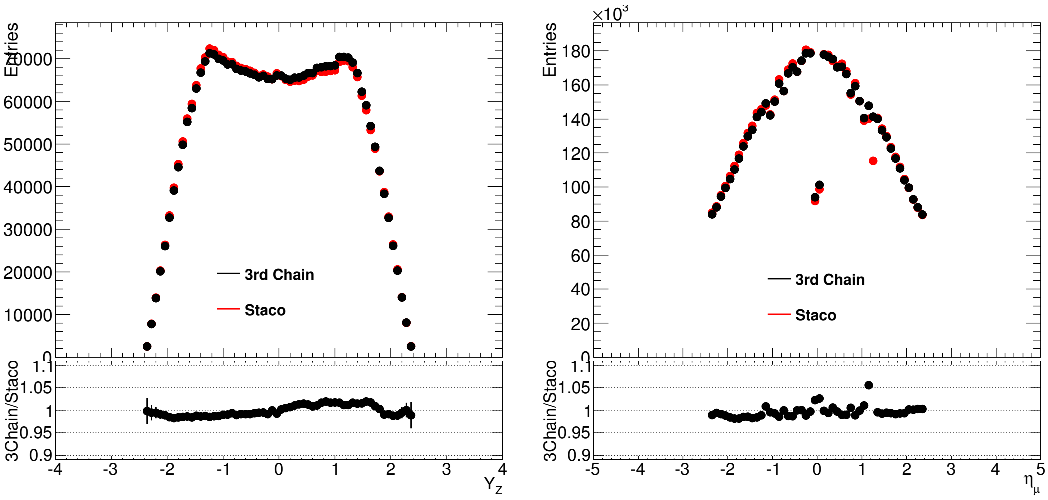

(a) Muon Rapidity (b) Muon Pseudorapidity

Figure 3.13: Comparison plots between the third chain muon algorithm and the staco muon algorithm.

interacting (such as a neutrino). The detailed reconstruction will be described in Chapter 4.

3.3 Data and MC samples

3.3.1 Collision data

The analysis was performed using ATLAS data collected in 2012, when the LHC delivered proton-proton collisions at $\sqrt{s} = 8$ TeV. The integrated luminosity recorded by ATLAS in 2012 was 20.3 fb^{-1} with a relative uncertainty of 1.9%. Only data taken during stable beam conditions and with a fully operating magnet system, tracking, calorimeter and muon sub-detectors, as defined by the ATLAS data quality group, are considered. The data used in this analysis is spread over 10 'periods', the total integrated luminosities of which are summarised in Tab. 3.1.

3.3.2 MC samples and cross-sections

In this analysis extensive use is made of simulated data generated using Monte-Carlo tools. The simulated datasets (or 'Monte-Carlo samples')

Period	Total integrated luminosity (fb^{-1})
A	0.79402
B	5.09466
C	1.40602
D	3.28839
E	2.52628
G	1.27481
H	1.44493
I	1.01626
J	2.59634
L	0.83977
Total:	20.28148

Table 3.1: Total integrated luminosities of the ATLAS 2012 data-taking periods.

are generated using a variety of generators—namely POWHEG [10, 9], PYTHIA 8.170 [91, 90], MC@NLO [59], JIMMY [41], SHERPA [61] and HERWIG [51] — to simulate the physical processes. These are further processed to model the effects of the ATLAS detector using a Geant4-based simulation [7]. The effect of additional proton-proton collisions occurring in the same bunch-crossing as the collision of interest (in-time pile-up) and in the previous and subsequent bunch crossing (out-of-time pile-up) are included in the Monte-Carlo simulation for the samples used in this analysis [31].

The principal purpose of these Monte-Carlo samples is to model the contamination of the 'signal' process from other 'background' processes, which might have similar experimental signatures. Another main purpose of the Monte-Carlo samples is to correct the measured data for the effects of the detector, such that a close-as-possible comparison may be made with theoretical predictions.

The signal Monte-Carlo samples used in the W asymmetry analysis detailed in Chapter 5 are listed in Tab. 3.2 together with the total numbers of events in each sample and corresponding cross-sections. The cross-section for the Powheg+Pythia8 and Sherpa samples corresponds to a NLO theory calculation (with a 'k-factor' scaling to the total cross section at NNLO). The main signal MC in the W asymmetry analysis is Powheg+Pythia8, while Sherpa is used for some systematic checks.

Process	Generator	Dataset	ε_{filter}	σ[pb]	$\sigma \times BR \times$ ε_{filter}[pb]	Evt [M]
			muon channel samples			
$W^+ \to \mu^+\nu$	PowhegPythia8	147801	1.0	7116(5%)	7116	23
$W^- \to \mu^-\bar{\nu}$	PowhegPythia8	147804	1.0	5069(5%)	5069	17
$W \to \mu\nu$	Sherpa	147775	1.0	12186(5%)	12186	40

Table 3.2: The signal Monte-Carlo samples used in the presented analysis.

Process	Generator	ε_{filter}	σ[pb]	$\sigma \times BR \times$ ε_{filter}[pb]	Evt [M]
$Z \to \mu\mu$ $M > 60$ GeV, 2μ filter	Powheg+Pythia8	0.5661	1149.5(5%)	650.7	50
$Z \to \mu\mu$ $M > 60$ GeV, 1μ filter	Powheg+Pythia8	0.3093	1149.5(5%)	355.5	20
$Z \to \mu\mu$ $M > 60$ GeV, $veto - \mu$ filter	Powheg+Pythia8	0.125	1149.5(5%)	143.7	3
$Z \to \mu\mu$ $20 < M < 60$ GeV	Powheg+Pythia8	0.267	387.05(5%)	103.34	10
$Z \to \mu\mu$ $8 < M < 20$ GeV	Powheg+Pythia8	0.00678	1948.3(5%)	13.21	3
Z $\to \tau\tau$ Np0	Alpgen+Herwig+Jimmy	0.0396	876.2(5%)	34.698	5.5
Z $\to \tau\tau$ Np1	Alpgen+Herwig+Jimmy	0.0472	190.8(5%)	9.0049	2.5
Z $\to \tau\tau$ Np2	Alpgen+Herwig+Jimmy	0.0530	60.0(5%)	3.1791	0.5
Z $\to \tau\tau$ Np3	Alpgen+Herwig+Jimmy	0.0590	17.4(5%)	1.026	0.2
Z $\to \tau\tau$ Np4	Alpgen+Herwig+Jimmy	0.0675	4.7(5%)	0.315	0.03
$t\bar{t}$	McAtNloJimmy	0.5427	252.9(5.7%)	137.25	15
W$^+ \to \tau\nu$	PowhegPythia8	1.0	7116(5%)	7116	23
W$^- \to \tau\nu$	PowhegPythia8	1.0	5069(5%)	5069	17
W$\to \tau\nu$	Sherpa	1.0	12186(5%)	12186	7
WW	Herwig	0.382	70.4(10%)	26.89	2.5
ZZ	Herwig	0.211	7.2(4.2%)	1.52	0.2
WZ	Herwig	0.306	20.3(4%)	6.21	1
$\gamma\gamma \to \mu\mu$ $7 < M < 20$	Pythia8	0.0242	105(40%)	2.54	0.5
$\gamma\gamma \to \mu\mu$ $20 < M < 60$	Pythia8	0.330	18.62(40%)	6.15	0.5
$\gamma\gamma \to \mu\mu$ $60 < M < 200$	Pythia8	1.0	1.89(40%)	1.89	0.5

Table 3.3: The background Monte-Carlo samples used in the presented analysis.

The Monte-Carlo samples for the various background contributions are listed in Tab. 3.3. The filter-efficiency information is taken from the ATLAS database [13]. The $t\bar{t}$ cross-sections correspond to NNLO+NNLL predictions. [2].

In order to cover the entire kinematic range studied in the analysis, several background samples are merged together with respect to their luminosity. To take $Z \to \mu\mu$ Powheg+Pythia8 samples as an example, three samples for the mass region $Z_m > 60$ GeV are produced with different filters on lepton p_T and the sum of them gives a non-filtered sample. Due to the different filter efficiencies for $Z \to \mu\mu$ samples, the values for the cross-sections, given in Tab. 3.3 are different.

The ZZ and WZ cross-section are taken from an MCFM theory calculation [81], [1].

4

Reconstruction of the Missing Transverse Momentum

The neutrinos from the W boson decays can not be seen directly by the ATLAS detector, but their presence can be inferred by assuming that the transverse momentum of all final state particles should vector sum to zero. The negative of the vector sum of the transverse momentum of observed particles is called the missing transverse momentum, or $E_{\mathrm{T}}^{\mathrm{miss}}$. The missing transverse momentum can be associated to the neutrino transverse momentum in W boson decays. The basic method to derive the missing transverse momentum is to take the negative vector sum over all the momentum from physics objects which are detected in the transverse plane. Several methods have been studied in this thesis to optimise the performance of missing transverse momentum in proton-proton collisions at a centre of mass energy of 8 TeV in 2012 at the ATLAS detector.

4.1 Reconstruction Methods

The decay processes of W and Z bosons in the transverse plane are illustrated in Fig. 4.1. The transverse momemtum of vector bosons is due to initial state radiation.

The transverse momentum of the W bosons can be calculated as the vector sum of the decay muon and neutrino, shown in Equ. 4.1. The momentum from the initial state radiation of quarks and gluons balances the transverse momentum of the W boson and is boosted in the opposite direction, the so called "hadronic recoil". Therefore the hadronic recoil can be obtained by the vector sum over the transverse momentum of all the other particles except the muon and neutrino.

$$\vec{p_T}(W) = \vec{p_T}^{\mu^{\pm}} + \vec{p_T}^{\nu} = -\vec{\mathrm{HR}} \tag{4.1}$$

The transverse momentum of the neutrino can be deduced by the negative vector sum over the hadronic recoil and the muon transverse momentum, i.e.

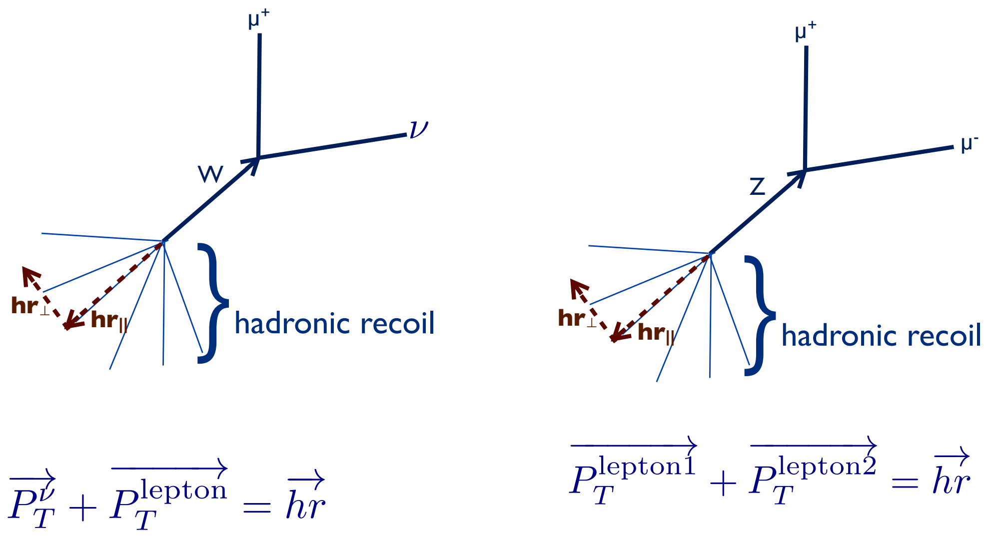

(a) W Boson

(b) Z Boson

Figure 4.1: The decay processes of the W and Z bosons, as shown in the transverse plane indicating the momentum balance between the boson and the hadronic recoil.

the negative vector sum over all the particles' momentum in the transverse plane. As the transverse momentum of neutrinos (p_T^{ν}) can be associated with the missing transverse momentum ($E_{\mathrm{T}}^{\mathrm{miss}}$), the formula can be written as:

$$E_{\mathrm{T}}^{\mathrm{miss}} := \vec{p_T}^{\nu} = -(\vec{\mathrm{HR}} + p_T^{\mu^{\pm}}) \tag{4.2}$$

For 7 TeV collisions the missing transverse momentum was defined to be the negative of the vector sum over the momentum of calorimeter clusters. [96]. This clusters-based method assumes calorimeter clusters represent all the hadronic activity of particles including the charged electrons and non-charged neutrons and photons. For an analysis with 8 TeV collision data, the method would suffer from contamination from additional proton-proton collisions occurring in the same bunch-crossing (in-time pile-up) and those collisions in the preceding and following bunch-crossing (out-of-time pile-up) due to the higher luminosity. As it is difficult to distinguish the clusters from the primary decay process or the pile-up, several track based methods to reconstruct the hadronic recoil are studied as tracks are more easily associated to the primary vertex. The basic tracks based method used is to negatively vector sum over primary vertex tracks in the inner detector. In this thesis, several reconstruction method are studied and optimised to achieve the best performance:

- Track based method
- Tracks and clusters association method
- Improvement of general $E_{\mathrm{T}}^{\mathrm{miss}}$ for all physics processes

The decay of the Z boson to two muons is a similar process to W boson decays, but with two clear signal muons which balances the hadronic recoil, as shown in Equ. 4.3, therefore the hadronic recoil can be precisely calibrated using Z boson decays.

$$\vec{p}_T(Z) = p_T^{l+} + p_T^{l-} = -\vec{\mathrm{HR}} \tag{4.3}$$

The hadronic recoil alogrithms which are developed in Sec. 4.2 and Sec. 4.3 can be the input for the general $E_{\mathrm{T}}^{\mathrm{miss}}$ for all physics processes in Sec. 4.4.

4.2 Track Based Method

The motivation to use tracking information in the calculation of the hadronic recoil (rather than only calorimeter cluster information), is that pile-up rejection is much better for tracks then clusters, since tracks can be easily associated to the primary vertex of the collision. It is assumed that the number of tracks, and their momentum distributions are representative of the overall hadronic activity.

The nominal track based missing transverse momentum (TrackMET) is the negative vector sum over all the momentum of selected tracks from the primary vertex. The primary vertex tracks are required to be above a certain momentum threshold to avoid noise and be within the tracking detector geometry. The exact track requirements are listed as follows:

- Track $p_T > 500$ MeV, the track transverse momentum has to be above the threshold of the minimal $p_T = 500$ MeV which the standard ATLAS tracking algorithms can reconstruct.
- Track $|\eta| < 2.5$, the track pseudorapidity is within the extension of the ATLAS tracker.

- Track $d_0 < 1.5$ mm, the nearest distance between the track and the primary vertex has to be within 1.5 mm.

- Track $z_0 \cdot \sin\theta < 1.5$ mm, the distance between the track and the primary vertex in the longitudinal plane has to be within 1.5 mm.

- Track Pixel Hits ≥ 1, track passes at least one out of three pixel layer.

- Track SCT Hits ≥ 6, track passes at least six out of eight SCT layers.

where track d_0 and z_0 are the transverse and longitudinal impact parameters with respect to the primary vertex respectively. The number of hits in the pixel and semiconductor tracker is required to be greater or equal to 1 and 6 respectively to ensure tracks originate from the collision, and not from cosmic rays.

The electron momentum as measured with clusters in the calorimeter has a better resolution than when measured with tracks in the inner detector. Therefore the momentum of electron tracks is replaced with the electron cluster momentum measured in the calorimeter for the track based missing transverse momentum.

Since the information from neutral particles cannot be measured using tracks in the inner detectors, jets are included to improve the track based missing transverse momentum, the so called "TrkMET+Jets" in this thesis. Jets are selected to be above a certain momentum threshold (optimised to be above 20 GeV for this algorithm) to ensure only good quality jets are included. In order to reduce the jets originating from the pile-up vertices, the jet vertex fraction of selected jets has to be above 25% (JVF> 0.25, Jet Vertex Fraction is defined as in Equ. 3.4). If the tracks are associated to the selected jets, the track transverse momentum is replaced by the jet transverse momentum to avoid double counting.

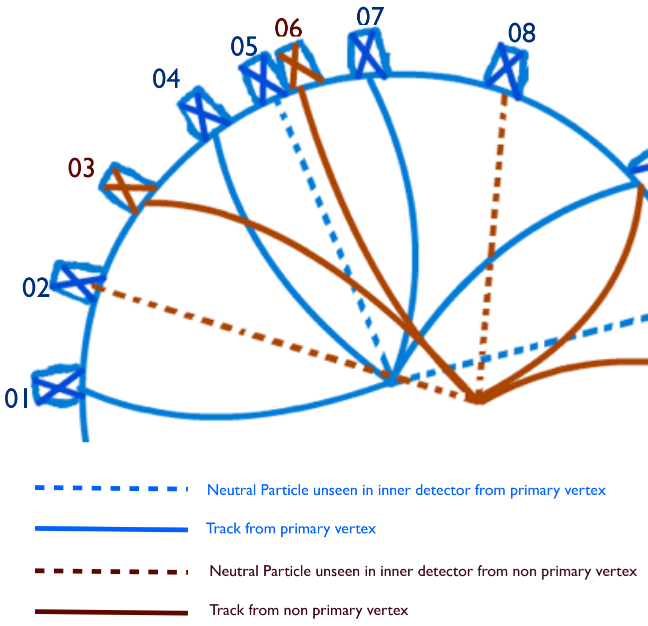

Figure 4.2: A schematic plot to indicate the track and cluster association method. The red crossed cells (eg. 03, 06 and 11) are subtracted from the improved cluster-based hadronic recoil as they most likely originate from pile-up vertices. If the clusters are associated to the primary vertex track and the secondary vertex track, they are kept.

4.3 Tracks and Clusters Association Method

To take advantage of the better pile-up rejection of tracks and not to lose all the information from neutral particles, the cluster-based method is modified to remove those clusters which are associated to secondary vertex tracks in order to reduce the contribution from pile-up but keep the neutral particles' contribution. The key features of the tracks and clusters association method are expressed in the schematic plot, Fig. 4.2. The association of the track and cluster is done by iterating over all the tracks and searching the cluster within a optimised $\Delta R_{\mathrm{trk,cl}}$ cone which is defined in terms of the angular difference between track and cluster in the transverse plane ($\Delta\phi$) and the difference between the two in pseudorapidity ($\Delta\eta$):

$$\Delta \mathrm{R}_{\mathrm{trk,cl}} = \sqrt{\Delta\phi^2_{\mathrm{trk,cl}} + \Delta\eta^2_{\mathrm{trk,cl}}} \tag{4.4}$$

The optimal size of the $\Delta \mathrm{R}_{\mathrm{trk,cl}}$ cone is determined from the performance of the hadronic recoil in terms of its pile-up dependence and the response of the boson transverse momentum. The details will be discussed in Sec. 4.3.4.

To take $Z \rightarrow \mu\mu$ events as example, the average number of the total tracks per event is around 300. The number of tracks originating from the primary vertex is typically around 20 tracks per events. There are around 400 clusters per event and around 200 clusters after subtraction of those clusters which are associated to the non-primary vertex tracks. The detailed distributions are shown in Fig. 4.3.

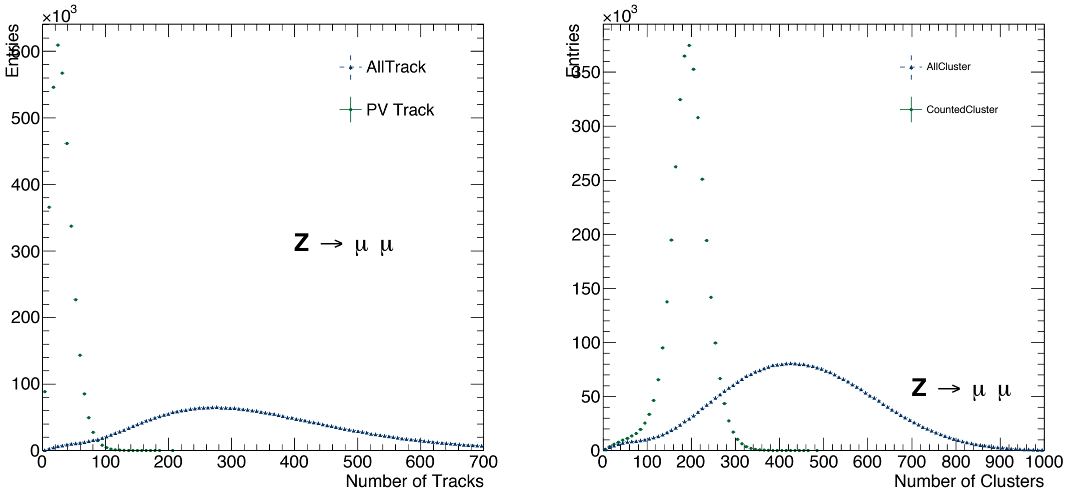

Figure 4.3: The distribution of the number of the primary vertex tracks and all tracks per event is shown in the left plot. The distribution of the number of the clusters which are selected after the subtraction of the contribution from non-primary vertices and the total number of clusters is shown in the right plot.

Those clusters which are associated within the $\Delta \mathrm{R}_{\mathrm{trk,cl}}$ cone with the secondary tracks are removed from the negative vector sum of cluster transverse momentum. If the cluster is both associated to the primary and secondary tracks, this cluster is included in the hadronic recoil calculation. All the clusters without any association are also included.

The tracks and clusters association method combines the advantage of good rejection of pile-up when using only tracking information but without losing all the information of neutral particles. In order to optimise the association algorithm and gain the best performance, several studies were done and will be described in more detail in the following sections:

- The depth of the cluster seed for the association.
- Different types of the cluster calibration.
- The treatment for the clusters without any association.
- The size of the cone for the track and cluster association.
- The priority of the association criteria.

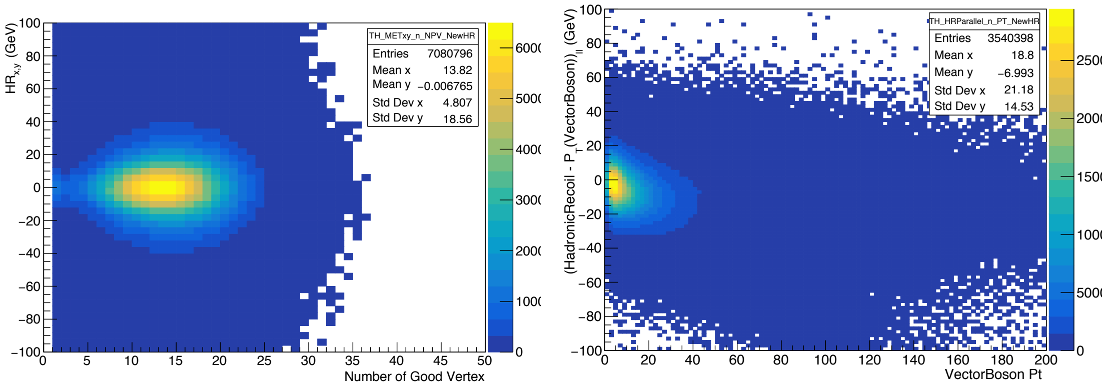

(a) HR in bins of good vertices

(b) HR projected to $p_{T,Z}$ in bins of $p_{T,Z}$

Figure 4.4: An example of the hadronic recoil distribution in bins of the number of good vertices is shown in the left plot. And the difference of the projected hadronic recoil toward the vector boson transverse momentum and Z boson transverse momentum is shown in the right plot.

The performance of the hadronic recoil can be checked with respect to two criteria, pile-up dependence and vector boson response (balance between vector boson transverse momentum and hadronic recoil). The resolution with respect to the number of vertices tests the pile-up dependence. The response of the hadronic recoil with respect to the vector boson transverse momentum tests the balance between vector boson transverse momentum and hadronic recoil.

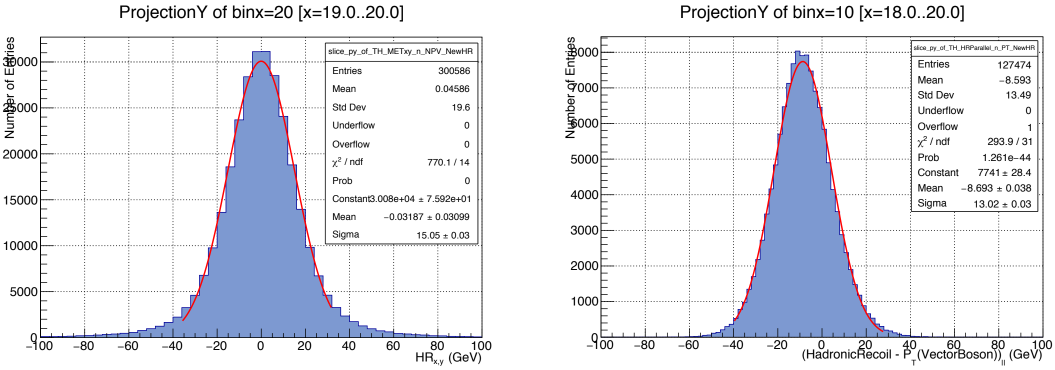

(a) σ of HR in the bin of 20 good vertices (b) Mean of HR in the bin of $p_{T,Z} = 10$GeV

Figure 4.5: Example of the fitting of the hadronic recoil distribution in the bins of 20 well reconstructed vertices is shown in the left plot. And the fitting results of the difference of the projected hadronic recoil toward the vector boson transverse momentum in the bin of Z boson transverse momentum at 10GeV is shown in the right plot.

The two performance plots used to test the pile-up dependence of the hadronic recoil can be derived from the two dimensional distribution of hadronic recoil (x- and y- component of hadronic recoil) versus the number of well reconstructed vertices after collisions, number of “Good Vertex” in the plots, as shown in the left of Fig. 4.4. The number of well reconstructed vertices after collisions is defined as the primary vertex which has at least three tracks associated with it. It is assumed that the hadronic recoil distribution in each slice of number of good vertices is Gaussian in form. The resolution (for a particular number of good vertices) is defined to be the width of a fitted Gaussian to the hadronic recoil distribution. The fit is performed only in the region +/- 2.5 RMS from the peak, shown in the left plot of Fig 4.5. If the resolution is constant with increasing number of well reconstructed vertices, it shows that the hadronic recoil is pile-up independent. If the resolution is smaller, the pile-up dependence is generally less.

To check the response of the hadronic recoil, the two dimensional plot of the difference of the projected hadronic recoil toward the vector boson transverse momentum and the vector boson transverse momentum can be plotted and is shown in the right plot of Fig. 4.4. The same technique for fitting the resolution plot is used also for the response plot. The mean of the HR-$p_{T,Z}$ distribution in each $p_{T,Z}$ slice is used as an indicator for the balance between the hadronic recoil and the vector boson transverse momentum. One of the examples after fitting is shown in Fig. 4.5. The response is tested as a function of different vector boson transverse momenta. The priority when determining the selection criteria is to firstly have a good response and then a good resolution. In other words: The width of the hadronic recoil distribution as a measure of its resolution is not directly connected to the sensitivity of the hadronic recoil to the transverse momentum of the vector boson.

4.3.1 The depth of the cluster seed

In order to associate reconstructed tracks and clusters, the particle track is extrapolated to the different layers of the calorimeter i.e. a different depth of the cluster seed, see Sec. 3.2.7. The goal is to find the optimized association location for the extrapolated track and the cluster.

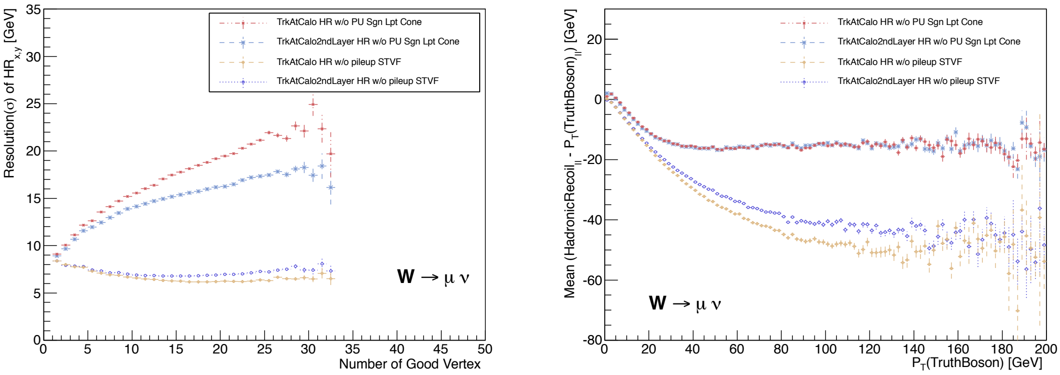

Figure 4.6: The performance plots of the particle track is extrapolated to the different layers of the calorimeter, the first layer of calorimeter (TrkAtCalo) and the second layer of calorimeter (TrkAtCalo2nd). The “stvf” algorithm is also included in the plots with two different extrapolated depth of the cluster seed, which is labelled as “w/o pileup STVF”. And the nominal algorithm is labelled as “w/o PU Sgn Lpt Cone”. For the nominal algorithm, both extrapolated layers show good response, but the extrapolated depth of the cluster seed to the second layer shows better pile-up independence.

Two different extrapolation points for tracks from the inner detector have been tested here: tracks are extrapolated to the first or second layer of the electromagnetic calorimeter (LarEM). Fig. 4.6 presents the results for the different extrapolation points. Both track extrapolation points considered have a similar and good response for the default track-based hadronic recoil algorithm. But the resolution is significantly worse for the extrapolation to the first layer than to the second layer. This is because the core of the electromagnetic shower is seeded and deposited around the second layer of the calorimeter.

4.3.2 Different types of the cluster calibration

The clusters reconstructed using the local hadron (LC) calibration [70] are commonly used for many ATLAS analyses as this local hadron calibration takes into account the invisible, out-of-cluster energies and the energy deposited in the dead material using visible energy deposited in the calorimeter. The alternative option is to use the EM calibration [70] for the clusters. Two different calibration method are tested and shown in Fig. 4.7.

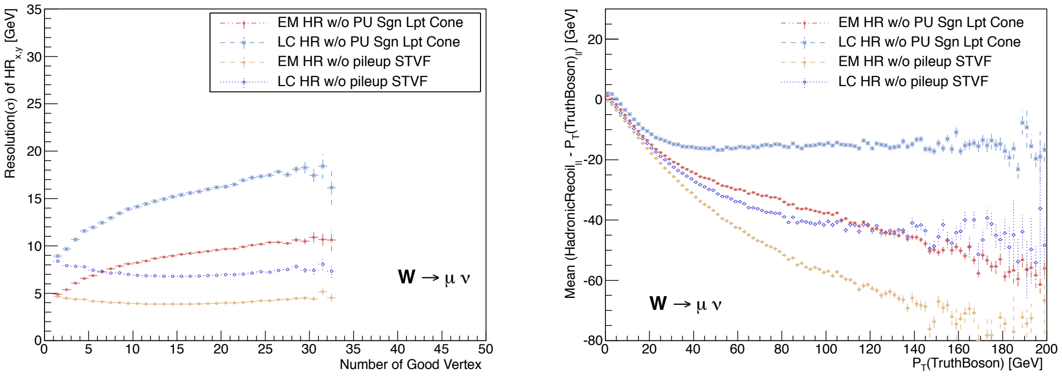

Figure 4.7: The performance plots of using two different cluster reconstruction algorithm, the local hadron calibration (LC) and the EM calibration. The “stvf” algorithm is also included in the plots with two different extrapolated depth of the cluster seed, which is labelled as “w/o pileup STVF”. And the nominal algorithm is labelled as “w/o PU Sgn Lpt Cone”. For the nominal algorithm, the local hadron calibration shows good response but the EM calibration loses accuracy.

The local calibration of the clusters has good response with respect to the vector boson transverse momentum. The hadronic recoil with EM calibrated clusters does not balance the vector boson transverse momentum at higher values. Therefore even if the resolution with EM calibration is better than with LC calibration, the local hadron calibration is chosen for the reconstruction of the hadronic recoil.

4.3.3 The treatment for the clusters without any association

For the default method, all the clusters without any track association are included in the calculation. Those clusters without any associated tracks likely originated from neutral particle interactions. The pile-up contamination to these neutral particles would not be subtracted when using the default method. The fraction of neutral particle cluster energy associated to the primary vertex can be estimated from the tracking information available. The variable “stvf” is defined to be the sum of track transverse momentum associated to the primary vertex divided by the sum of all tracks transverse momentum (Equ. 4.5). The energy of the neutral clusters can then be multiplied by the stvf fraction.

$$\mathrm{stvf} = \frac{\sum \mathrm{P}_{\mathrm{T,\ tracks\ from\ primary\ vertex}}}{\sum \mathrm{P}_{\mathrm{T,\ all\ tracks}}} \tag{4.5}$$

Fig. 4.6 and Fig. 4.7 show a comparison between the default method, without treatment of neutral particles, and the “stvf” method (also showing track extrapolation to different layers and the different cluster calibrations). The “stvf” treatment does significantly improve the pile-up dependence as the number of good vertecies increases, but the hadronic recoil with the stvf fraction applied on the neutral clusters completely loses its balance to the vector boson transverse. Therefore the “stvf” method is not used in the final hadronic recoil reconstruction.

4.3.4 The size of the cone for the track and cluster association

The size of the ΔR cone described in Equ. 4.4 around the track in order to associate the cluster is examined here. Two values of 0.15 and 0.2 are tested. Fig. 4.8 shows the resolution and response plots when using these ΔR values for the association. Both of the cone sizes considered perform similarly in terms of the response, but the 0.15 cone performs slightly better with regards to the resolution in the higher pile-up conditions, especially when the number of well constructed vertices is larger than 20. The size of the cone with $\Delta\mathrm{R} = 0.15$ is chosen for the final reconstruction.

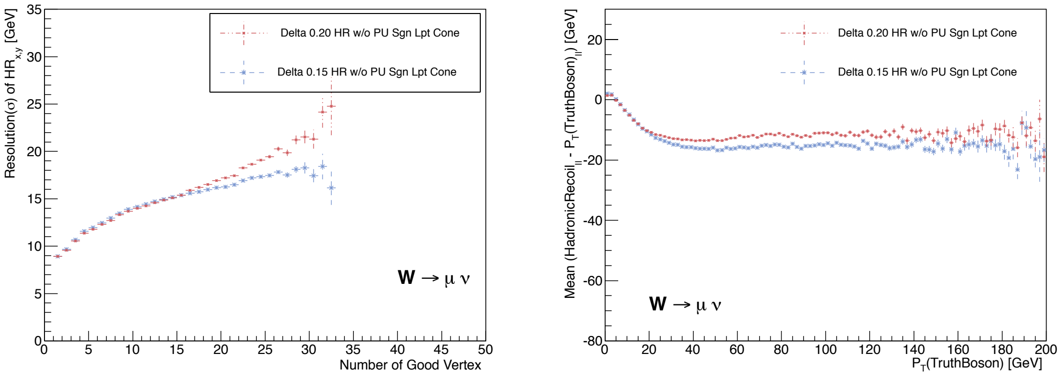

Figure 4.8: The performance plots of two different ΔR cone sizes used for the track and cluster association, ΔR =0.15 and ΔR = 0.2. The ΔR = 0.15 cone size shows better pile-up stability than with ΔR = 0.2. Both of the ΔR cone sizes for the track and cluster association show good response.

This study shows that taking out all the clusters bigger than the ΔR cone 0.15 (eg. 0.2) which are associated to non-primary vertex tracks might possibly remove non pile-up clusters and worsen the pile-up stability.

4.3.5 The priority of the association criteria

In the algorithm described for the previous sections, clusters are kept if they are both associated to primary and secondary tracks. There are also a small percentage of the tracks which are associated to more than one cluster. For the track and cluster association algorithm using the size of the ΔR cone, those clusters which are associated to the same non-primary vertex track will all be subtracted. In order to test more precisely if this algorithm performs well, two more algorithms are introduced for comparison:

- Take out all the clusters in the ΔR cone of size 0.15 which are associated to the non-primary vertex track (nominal).
- Only take out the nearest cluster which is associated to the non-primary vertex track.
- Only take out the cluster with the highest transverse momentum which is associated to the non-primary vertex track in the same cone.

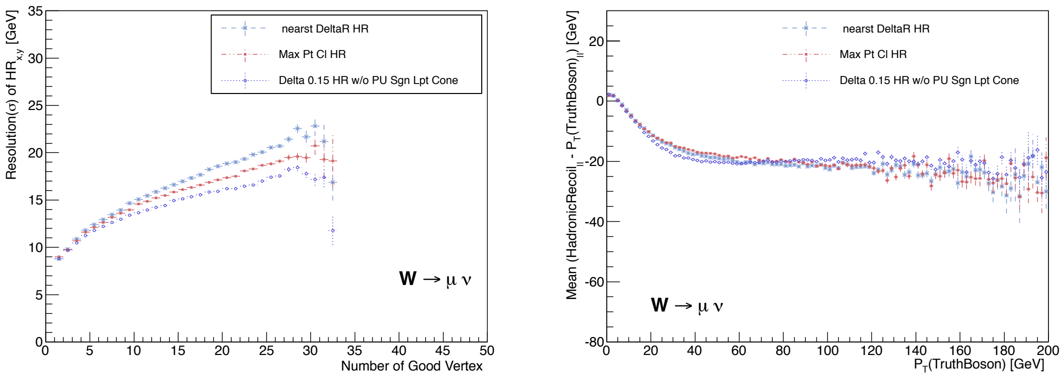

Figure 4.9: The performance plots of track and clusters association with the nearest ΔR (labelled as "nearest DeltaR) or the hightest cluster p_T (labelled as Max Pt Cl). The nominal algorithm which is taking out all the clusters in the ΔR cone of size 0.15 is labelled as "Delta 0.15 HR w/o PU Sgn Lpt Cone". The nominal algorithm shows the best pile-up stability.

The results are shown in Fig. 4.9. For all three algorithms, the response is generally similar and quite stable. The algorithm using a ΔR cone of 0.15 becomes more stable above a vector boson transverse momentum of 30 GeV, and has the best resolution over all three algorithms. The resolution results imply that removing all the clusters within the associated cone better removes the pile-up contamination than just removing a single cluster.

4.3.6 Hadronic Recoil with Data and MC Comparsion

As part of the study to optimize the algorithm of the hadronic recoil obtained using the track and cluster association method, it is crucial to check the performance between the measured data and simulation, as the optimization is mostly done with the simulation.

A comparison between simulation and data in the proton proton collisions obtained at a centre of mass energy of 8 TeV in 2012 in ATLAS is shown in Fig. 4.10. The results are performed using $Z \rightarrow \mu\mu$ events using a subset of the full ATLAS dataset with an integrated luminosity of 4.69 fb^{-1}. Good agreement is seen between data and prediction for the hadronic recoil and pile-up stability distributions.

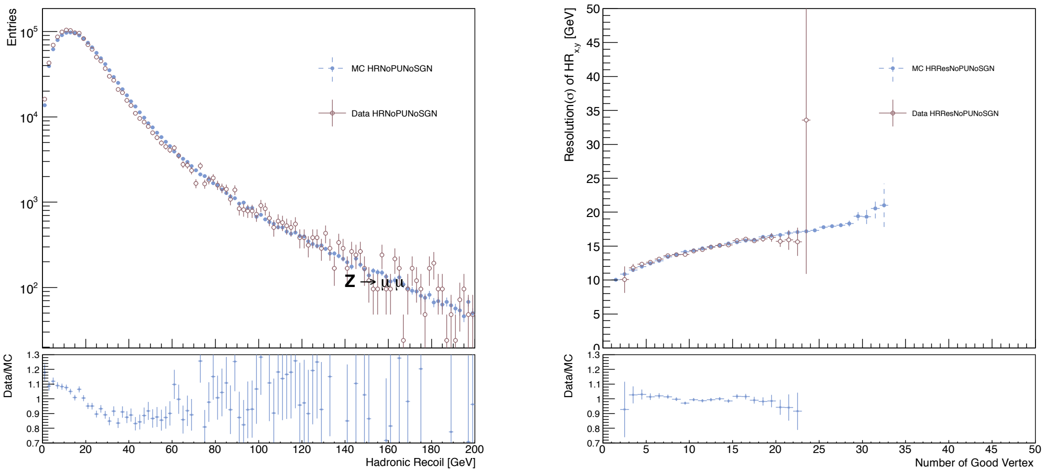

Figure 4.10: Data and MC comparsion plots of the hadronic recoil using the optimised tracks and cluster algorithm of $Z \to \mu\mu$ events. The blue solid dots are the Monte Carlo simulation and the red circles are measured data. The left plot is the distribution of the hadronic recoil and the right plot is the resolution of the hadronic recoil. The ratio plots on the bottom are the ratio of data over MC.

4.4 Improvement of general $E_{\mathrm{T}}^{\mathrm{miss}}$ for all physics processes

It is desirable to have a general algorithm that is suitable for determining the missing transverse momentum in all types of physical process. For this purpose the “`MET_RefFinal`” algorithm was developed. The “`MET_RefFinal`” algorithm is similar in concept to those algorithms discussed in the previous sections. The clusters or tracks which are not associated to any signal objects (for example muons, electrons or jets) are considered to be the “soft term”, which can be related to the hadronic recoil in W and Z events, and the other (already calibrated) physical objects with momentum over a certain threshold are included in the “hard term”. The `MET_RefFinal` algorithm is calculated separately along the x and y axes in the order of electrons, photons, hadronically decaying tau-leptons, jets, muons, and soft term [28]. The order matters as certain detector signals may be for example reconstructed as both electrons and jets.

$$E_{x(y)}^{\mathrm{miss}} = E_{x(y)}^{\mathrm{miss},e} + E_{x(y)}^{\mathrm{miss},\gamma} + E_{x(y)}^{\mathrm{miss},\tau} + E_{x(y)}^{\mathrm{miss,jets}} + E_{x(y)}^{\mathrm{miss},\mu} + E_{x(y)}^{\mathrm{miss,soft}} \tag{4.6}$$

The clusters-based soft term was used in the algorithms developed for ATLAS 7 TeV analyses. Since the pile-up is larger at 8 TeV a track-based soft term was also implemented. Both cluster- and track-based algorithms are compared in the performance studies in Sec. 4.5. The version of `MET_RefFinal` with the track soft term is labelled "METRefFinal_TST" to distinguish this from the original version with the cluster soft term.

4.4.1 Jets Selection

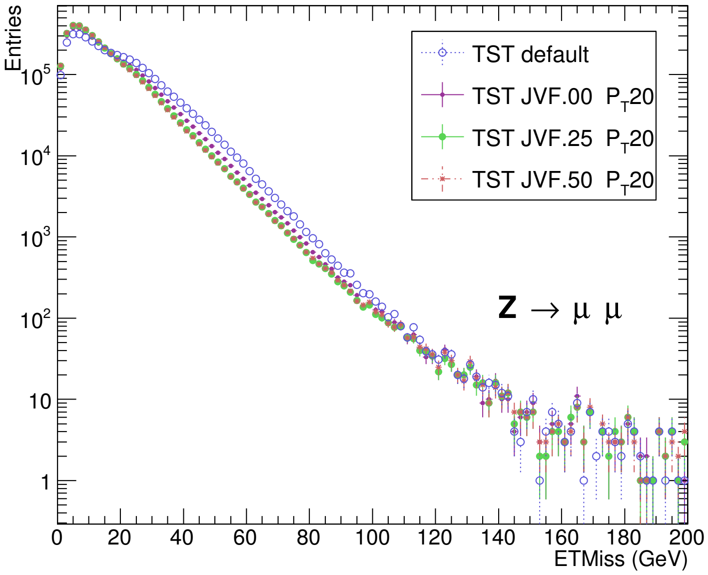

Figure 4.11: Distribution of $E_{\mathrm{T}}^{\mathrm{miss}}$ with varying jet JVF selections: *default* indicates no JVF requirement, other thresholds on |JVF| are as shown. The jet p_{T} threshold is kept at 20 GeV.

If the cluster-based soft term were to be simply replaced with the track-based soft term - a shoulder is seen to appear in the $E_{\mathrm{T}}^{\mathrm{miss}}$ distribution at around 20-40 GeV as shown in Fig. 4.11. The non-smooth $E_{\mathrm{T}}^{\mathrm{miss}}$ distribution results from pile-up jets which form part of the `MET_RefFinal`. In order to optimize the jet selection for the reconstruction of the `MET_RefFinal` with the track soft term, several criteria are tested. The higher energetic jets are less likely to be pile-up jets. The jets with higher jet vertex fraction (JVF, for further details see Sec. 3.2.7) are also less likely to originate from pile-up vertices.

In order to significantly reduce the pile-up contamination, the jet selection is tested with the following parameters:

- The jet p_{T} threshold above: 20 GeV(default), 25 GeV, and 30 GeV.

- The absolute value of JVF above (greater but not equal): 0.00, 0.25, and 0.50. (default value is without any JVF cut)

The shoulder structure of the $E_{\mathrm{T}}^{\mathrm{miss}}$ distribution is removed after the minimum JVF cut (above 0.00) is applied, as shown in Fig. 4.11. The JVF can be zero if no track originating from the primary vertex is associated to a jet. The results show that the structure comes from the inclusion of jets without any primary tracks associated to them. Fig. 4.12 shows more details of the effect of the different JVF cuts with the $E_{\mathrm{T}}^{\mathrm{miss}}$ response to the Z boson transverse momentum scale (left plot) and the $E_{\mathrm{T}}^{\mathrm{miss}}$ resolution with respect to the number of good vertices. The response of the $E_{\mathrm{T}}^{\mathrm{miss}}$ behaviour is similar regardless of the JVF cut applied. The resolution is significantly improved after a 0.25 JVF cut is applied and remains similar above this value. Hence, a cut of $|\text{JVF}| > 0.25$ is chosen for the $E_{\mathrm{T}}^{\mathrm{miss}}$ jet selection.

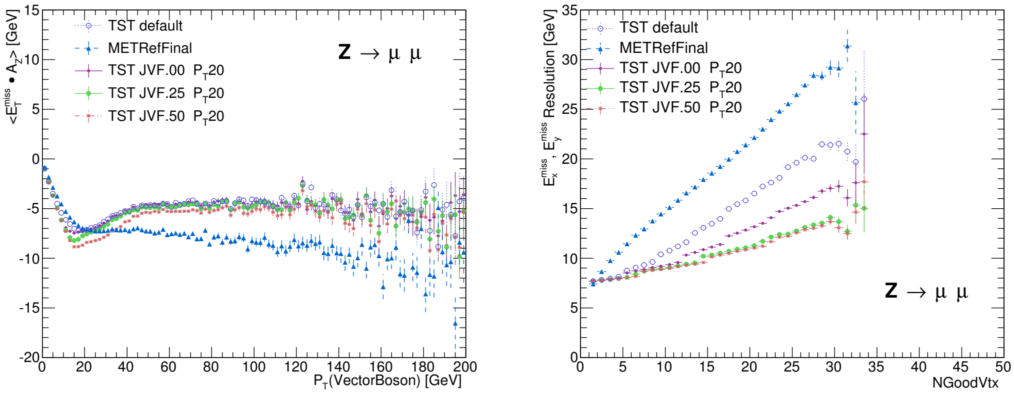

(a) Scale, inclusive jets

(b) Resolution, inclusive jets

Figure 4.12: Scale (left) and resolution (right) of $E_{\mathrm{T}}^{\mathrm{miss}}$ in $Z \to \mu\mu$ events with an inclusive jet selection. The selection of jets contributing to the $E_{\mathrm{T}}^{\mathrm{miss}}$ is the same as in figure 4.11. The `MET_RefFinal` scale distribution does not appear to "recover" at $p_{\mathrm{T}} > 20$ GeV due to the muon terms not being corrected for energy loss in the calorimeters.

Three different jet p_{T} thresholds are applied to test the performance of the response and resolution, as shown in Fig. 4.13. The higher jet p_{T} threshold does not improve the response but worsens the performance. Based on this, the jet p_{T} threshold over 20 GeV is chosen as default.

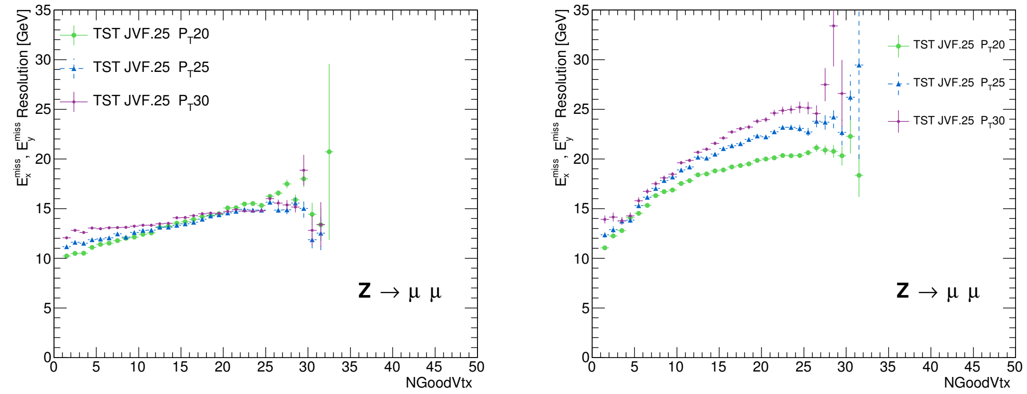

(a) Resolution, 1 central jet (b) Resolution, 1 forward jet

Figure 4.13: Resolution of $E_{\mathrm{T}}^{\mathrm{miss}}$ in $Z \to \mu\mu$ events with central (left figure) or forward (right figure) jet selection, where jets are classified as central if $|\eta| < 2.4$ and forward otherwise. The |JVF| cut is fixed at 0.25, and the p_{T} threshold is varied from 20 GeV to 30 GeV.

4.4.2 Truth Jets Matching

A study is performed to determine if the chosen cuts (p_{T} and JVF) are optimal with respect to selecting the jet of interest from the hard scatter or "true jet". A reconstructed jet is defined to be matched to a truth jet if the ΔR between them is less than 0.4. Only the truth jets with momentum above 7 GeV are used for the matching due to the poor jet energy resolution below this scale.

The fractions of events selected in which the reconstructed jet is matched to a truth jet were computed, for different choices of JVF and p_{T} cuts. Tab. 4.1 shows:

- The number of events in which there is one reconstructed central jet passing the selection. (labelled 1 Central JVF (all));
- The number of reconstructed events containing exactly one truth jet with $p_{\mathrm{T}} > 7$ GeV;
- The number and fraction of reconstructed events containing exactly one jet passing both the truth matching ($\Delta R < 0.4$ to a truth jet with $p_{\mathrm{T}} > 7$ GeV) and the jet (jet vertex fraction and the jet p_{T}) selection;

- The number and fraction of reconstructed events containing exactly one jet passing the truth matching but failing the jet (jet vertex fraction and the jet p_{T}) selection;

- The number and fraction of reconstructed events containing exactly one jet failing the truth matching but passing the jet (jet vertex fraction and the jet p_{T}) selection.

In the table “JVF” refers to events passing both the jet vertex fraction and the jet p_{T} selection requirements. As shown, the chosen selection criteria of $|\mathrm{JVF}| > 0.25$ and $p_{\mathrm{T}} > 20$ GeV selects 73.0% of truth-matched events while rejecting 20.3%. For the selected events, 19.1% contain an unmatched jet. The optimal selection criteria reduces significant amount of the fraction of jet failing the truth matching while is compared to the default selection from 47% to 19% as shown in the last column in Tab. 4.1. The study of the fraction of the selected jet matching to the truth jet shows that the optimal selection criteria improves the agreement with the truth jets in $E_{\mathrm{T}}^{\mathrm{miss}}$.

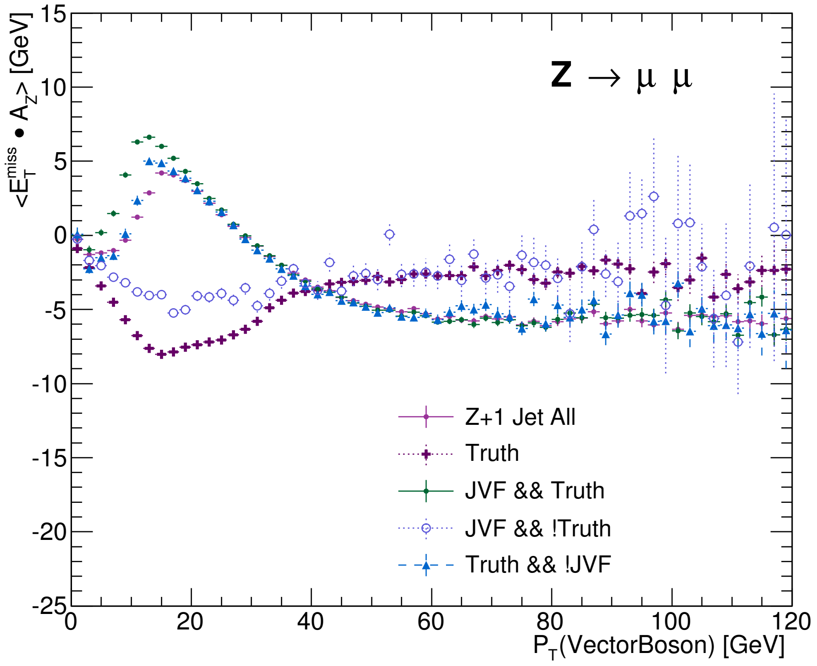

Figure 4.14: Response of $E_{\mathrm{T}}^{\mathrm{miss}}$ with varying truth central jet matching and JVF cut conditions are as shown. The jet p_{T} threshold is kept at 20 GeV, and the thresholds on $|\mathrm{JVF}|$ are at 0.25.

	1 Central JVF(All)	Truth (All)	1 Central Truth && JVF		Truth && fail JVF		1 Central JVF && fail Truth	
			#events	$\frac{(\mathrm{Truth\&\&JVF})}{\mathrm{JVF(All)}}$	#events	$\frac{(\mathrm{Truth\&\&!JVF})}{\mathrm{Truth(All)}}$	#events	$\frac{(\mathrm{!Truth\&\&JVF})}{\mathrm{JVF(All)}}$
JVF >0.00, $p_{\mathrm{T}} > 20$ GeV	926317	932957	586623	63.3%	247266	26.5%	434457	47.0%
JVF >0.25, $p_{\mathrm{T}} > 20$ GeV	786997		574584	73.0%	189623	20.3%	150330	19.1%
JVF >0.50, $p_{\mathrm{T}} > 20$ GeV	701534		537419	76.6%	163233	17.5%	61172	8.7%
JVF >0.00, $p_{\mathrm{T}} > 25$ GeV	666642		507743	76.2%	174224	18.7%	166761	25.0%
JVF >0.25, $p_{\mathrm{T}} > 25$ GeV	584992		499241	85.3%	146424	15.7%	44276	7.6%
JVF >0.50, $p_{\mathrm{T}} > 25$ GeV	545696		474646	87.0%	134739	14.4%	22860	4.2%
JVF >0.00, $p_{\mathrm{T}} > 30$ GeV	492395		415600	84.4%	125835	13.5%	68929	14.0%
JVF >0.25, $p_{\mathrm{T}} > 30$ GeV	454038		410512	90.4%	113800	12.2%	20204	4.4%
JVF >0.50, $p_{\mathrm{T}} > 30$ GeV	436306		396941	91.0%	106607	11.4%	14838	3.4%

Table 4.1: Number and fraction of reconstructed jets passing selections on Jet Vertex Fraction and transverse momentum, matched and unmatched to a truth jet with $p_{\mathrm{T}} > 7$ GeV in $Z \rightarrow \mu\mu$ events with a single central jet. Central jets are required to have $|\eta| < 2.4$. Jets with $p_{\mathrm{T}} > 50$ GeV are also considered to pass the JVF selection. Only jets retained at full calibration after $E_{\mathrm{T}}^{\mathrm{miss}}$ overlap removal are considered.

Fig. 4.14 shows the $E_{\mathrm{T}}^{\mathrm{miss}}$ response for each of the five selections listed above. All $Z \to \mu\mu$ events selected with one jet (purple dots in the plot) follow the same trend as events with truth jet matched (green dots in the plot). The response can be represented with the chosen selection criteria. The response compared to all the truth (blue crosses in the plot) tends to be stable when vector boson transverse momentum is above 40 GeV and the balance is within ± 5 GeV below 40 GeV.

4.4.3 Optimized All Physics Objects Selection

The final optimized selection for all the terms to reconstruct the "METRefFinal_TST" is as following:

- **Jet Term,** $E_{x(y)}^{\mathrm{miss,jets}}$ Jets with algorithm, *AntiKt4LCTopo* [42], is used for constructing the hard term of the missing transverse momentum. Jets used to calculate the jet term in the missing transverse momentum need to fulfil:
  - Jets with calibrated p_T greater than 20 GeV.
  - The jet vertex fraction (JVF) is greater than 0.25 for the central jets ($|\eta| < 2.4$). The JVF cut is not applied when the jet p_T is greater than 50 GeV in any detector η region.
- **Electrons Term,** $E_{x(y)}^{\mathrm{miss},e}$ Electrons used to construct the hard term of the missing transverse momentum are calibrated at the EM scale with the recommended calibration tool [16].
- **Muons Term,** $E_{x(y)}^{\mathrm{miss},\mu}$ The muon reconstruction algorithm *third-chain muons* as described in Sec. 3.2.7 is used for the missing transverse momentum. Muons in the missing transverse momentum calculation are calibrated with the same tool used for muon performance [25]. Muons are required to satisfy p_T greater than 5 GeV in order to be included in the $E_{\mathrm{T}}^{\mathrm{miss}}$ reconstruction. The contribution of muon energy deposited in the calorimeter is also taken into account for the muon reconstruction in the $E_{\mathrm{T}}^{\mathrm{miss}}$.

- **Track Soft Term,** $E_{x(y)}^{\text{miss,soft}}$ The track soft term is calculated using the same method as the track based method which was described in Sec. 4.2 but excluding all the tracks associated to the hard physics objects in order to avoid double counting. Tracks used to construct the soft term are required to fulfil the following selection:

    - $p_{\mathrm{T}} > 0.5\,\mathrm{GeV}$
    - $|\eta| < 2.5$
    - $n_{\text{pixel hits}} > 0$
    - $n_{\text{SCT hits}} > 5$

  The selection of tracks are matched to the primary hard-scatter vertex (PV) are:

    - $|z_0 \sin\theta| < 1.5\,\mathrm{mm}$
    - $|d_0| < 1.5\,\mathrm{mm}$

The final performance can be seen in the previous Fig. 4.12 with green dotted curves. The chosen selection criteria of “METRefFinal_TST” improves the response around 5 GeV at higher Z boson transverse momentum region compared to the old `MET_RefFinal` algorithm. The pile-up dependence of the resolution improves around 20 GeV compared to the old `MET_RefFinal` algorithm while the number of well reconstructed vertices is below 35.

4.5 Hadronic Recoil Performance in different event configurations

In order to validate the method to construct the hadronic recoil, the hadronic recoil studies on the W and Z events in both electron and muon decay channels are performed using the three algorithms already described:

- The track and cluster associated hadronic recoil (HR w/o PU & SgnLpt Cone)

- The hadronic recoil derived from the default `MET_RefFinal` with cluster soft term (HR `MET_RefFinal`)

- The hadronic recoil derived from TrackMET with jet correction (HR TrkMET + Jets)

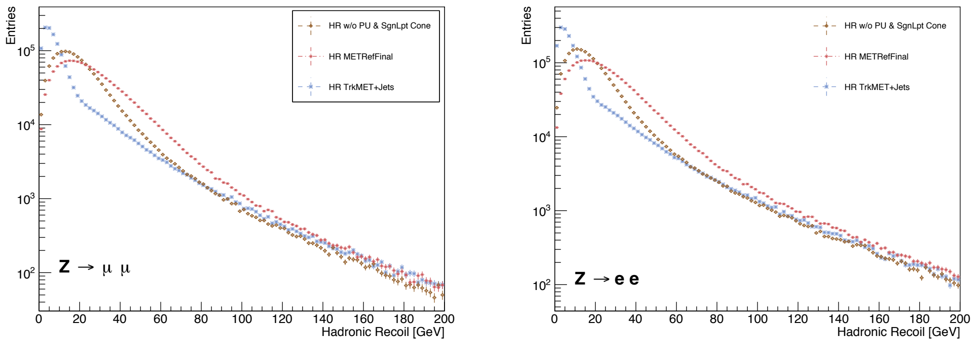

(a) $Z \to \mu^+\mu^-$ (b) $Z \to e^+e^-$

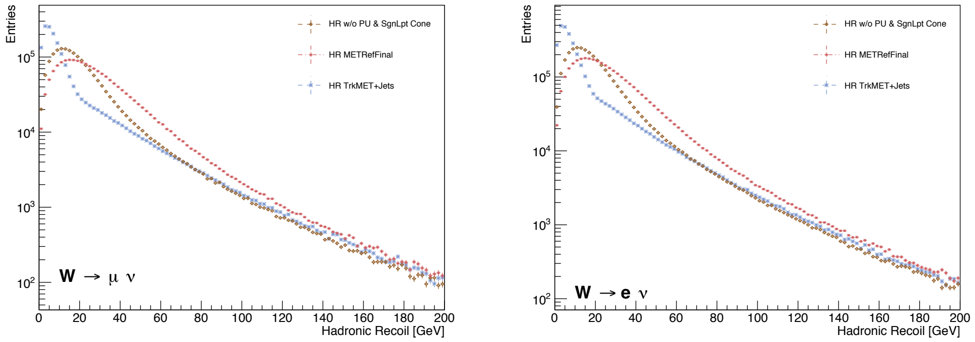

(c) $W \to \mu\nu$ (d) $W \to e\nu$

Figure 4.15: Hadronic recoil distributions for Z and W boson events in both the muon and electron decay channels. Three different algorithms are shown to compare their performance. The hadronic recoil derived from TrackMET with jet correction (HR TrkMET + Jets) has a visible transition at 20 GeV which is due to the selection of the jet p_{T} .

The hadronic recoil definition in terms of $E_{\mathrm{T}}^{\mathrm{miss}}$ is shown in Equ. 4.2. The first performance studies are done with Monte Carlo simulated at the detector reconstruction level with the PowhegPythia8 generator. The hadronic recoil distributions for Z and W events are shown in Fig. 4.15. The hadronic recoil distribution for both W and Z events have a similar behaviour. However there are differences between these three different hadronic recoil methods. The hadronic recoil reconstructed from the `MET_RefFinal` has the broadest distribution. A transition behaviour is visible at 20 GeV for the hadronic recoil reconstructed from the TrackMET with jets correction, because the selected jets have a threshold at 20 GeV which is not smoothly corrected for in the lower transverse momentum region.

The resolution plots which are used to test the pile-up dependence are shown in Fig. 4.16. TrackMET with jets correction clearly has the least pile-up dependence. The hadronic recoil reconstructed from the `MET_RefFinal` suffers a lot from pile-up contamination. The track and cluster associated hadronic recoil is a bit worse than TrackMET + jets but still tends to be stable at higher pile-up.

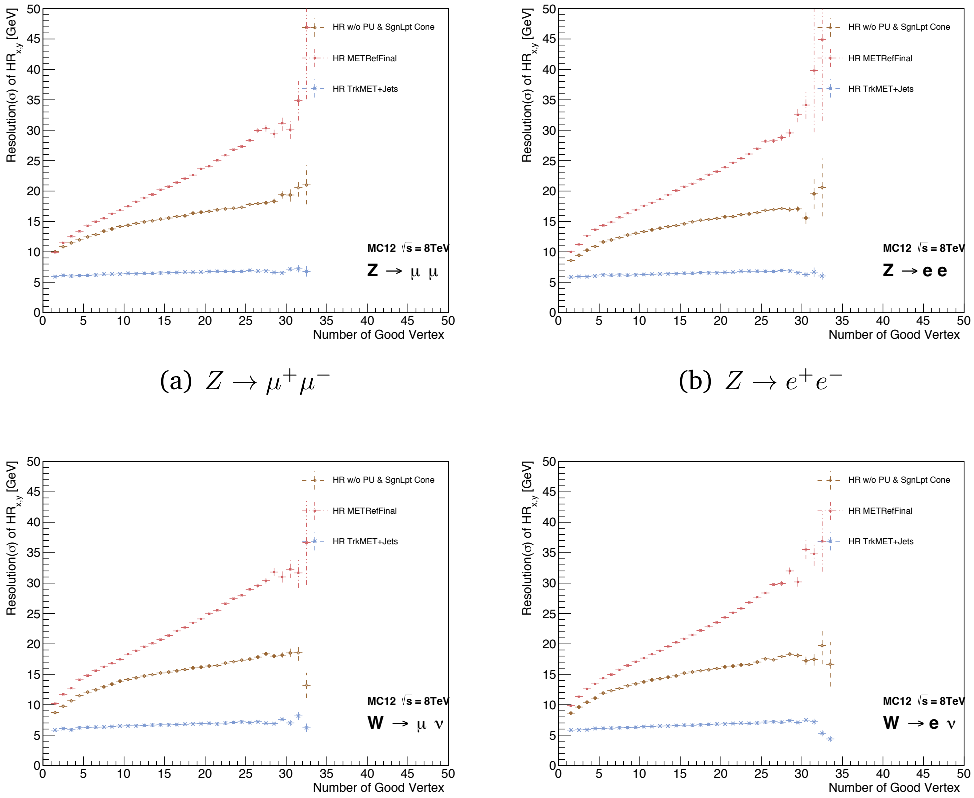

(a) $Z \to \mu^+\mu^-$ (b) $Z \to e^+e^-$

(c) $W \to \mu\nu$ (d) $W \to e\nu$

Figure 4.16: The performance plots to show the pile-up stability for Z and W boson events. Three different algorithms are shown to compare their performance. The hadronic recoil derived from TrackMET with jet correction (HR TrkMET + Jets) has best pile-up stability. The track and cluster associated hadronic recoil also performs well, but the hadronic recoil derived from the default `MET_RefFinal` with cluster soft term (HR `MET_RefFinal`) has high pile-up dependence.

The last important performance measure is the hadronic recoil response with respect to the vector boson transverse momentum which is shown in Fig. 4.17. All methods are quite stable at the higher vector boson transverse momentum region. But there is a sharp transition for the TrackMET with the jets correction. The transition point is again due to the selection of the jets. It is important to note that the strong dependence of the hadronic recoil determination for all chosen methods has only a little sensitivity on the transverse momentum of the vector boson for $p_{T,(V=W/Z)} < 20$ GeV.

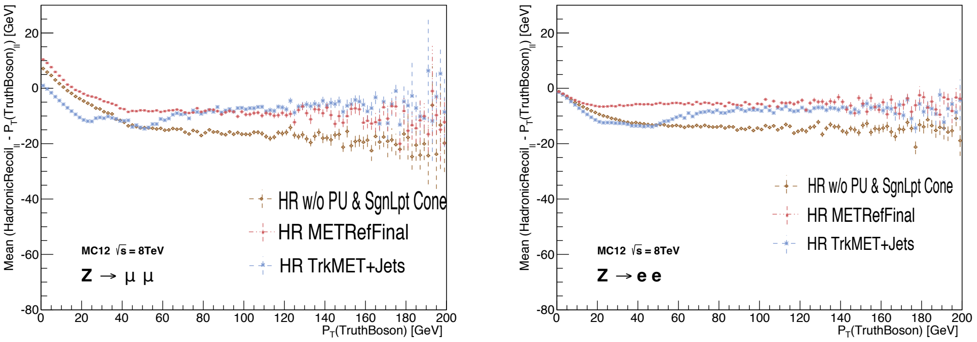

(a) $Z \to \mu^+\mu^-$ (b) $Z \to e^+e^-$

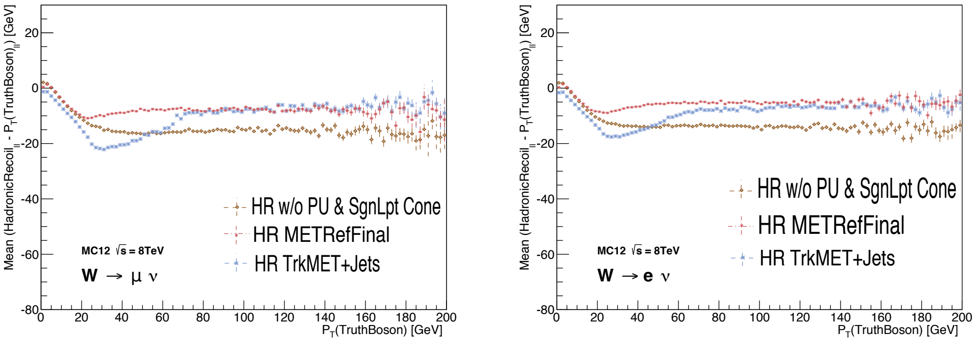

(c) $W \to \mu\nu$ (d) $W \to e\nu$

Figure 4.17: The performance plots to show the hadronic recoil response to the vector boson transverse momentum for Z and W boson events. Three different algorithms are shown to compare their performance. All three algorithms show a good response to the vector boson transverse momentum. But the hadronic recoil derived from TrackMET with jet correction (HR TrkMET + Jets) has a sharp transition at around 20 GeV of the vector boson transverse momentum which shows the instability of this algorithm.

In order to test if the hadronic recoil is biased towards the decay-leptons, a dedicated study has been performed in W boson events. [96] The performance plots are shown in Fig. 4.18 for the three different hadronic recoil definitions and for the muon and electron decay channels. The performance plots of Fig. 4.18 represent the mean difference between hadronic recoil and truth boson transverse momentum as a function of the azimuthal difference between the truth lepton and truth boson. The plots show that the measured values of the hadronic recoil projected perpendicularly on the vector boson transverse momentum is maximally biased when the lepton and W directions are orthogonal; the bias is 0 when the lepton and W are aligned. For the muon decay channel, the bias when the lepton and W direction are orthogonal reduces to around 500 MeV for the track and cluster associated hadronic recoil and the TrackMET with jet corrections compared to the hadronic recoil from `MET_RefFinal`. The effect in the muon channel is not significant between the hadronic recoil from `MET_RefFinal` and track and cluster association method.

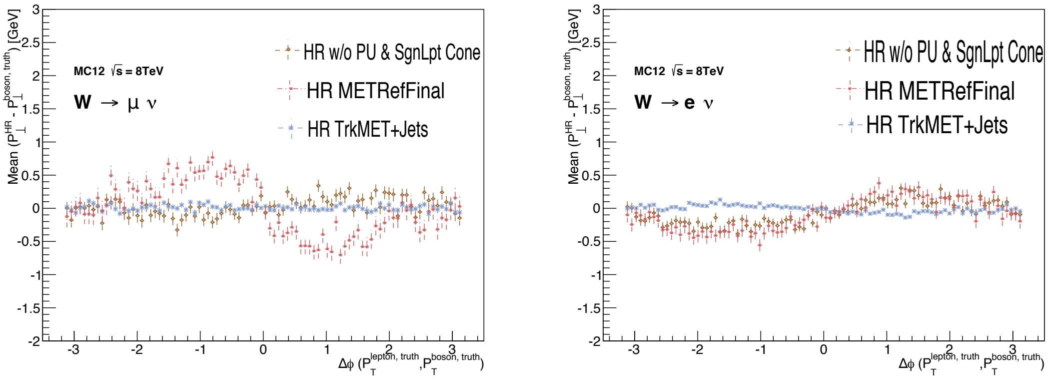

Figure 4.18: Hadronic recoil of W boson with truth comparison as a function of the angle between lepton and W boson transverse momentum. Three different algorithms are shown to compare their performance.

4.6 Summary of the Missing Transverse Momentum

Several algorithms of the track based missing transverse momentum are tested and have less pile-up dependence with respect to the cluster based missing transverse momentum. The optimization of the jet selection for the general missing transverse momentum (METRefFinal_TST) reconstruction fixes the bump at the lower end of the $E_{\mathrm{T}}^{\mathrm{miss}}$ distribution and improves its performance. The track and cluster association method provides a stable response with respect to the W and Z boson transverse momentum and has a good resolution, even with higher pile-up. Although the track and cluster association method appears a better candidate than the MetRefFinal_TST, further studies evaluating the systematic uncertainties are needed before it can be used in high precision physics analysis, such as the upcoming measurements of the W Boson mass. Hence, it was chosen to use MetRefFinal_TST for the measurements described in Chapter 5.

5

Measurements of the W boson charge asymmetry

As discussed in Sec. 2.3, the charge asymmetry of W bosons significantly constrains the up and down quark momentum fractions in the proton, which provides an important input for several high precision measurements which are currently performed at the LHC. [22]

The measurement of the W boson charge asymmetry is performed in the muon decay channel of the W boson, $W \to \mu\nu$. The signature of such events is one high p_{T} muon and missing transverse energy. The hadronic decay channel of the W boson ($W \to q\bar{q}$) cannot be used at the LHC due to the enormously large background contribution. The production cross section of the W bosons (with both positive charged lepton decay $W^+ \to \mu^+\nu$ and negative charged lepton decay $W^- \to \mu^-\bar{\nu}$) is measured in a first step. Since all correlations between systematic uncertainties can be evaluated, the charge asymmetry can be derived from these measurements in a second step.

The total cross section (σ_{tot}) of the W Boson is obtained using the following relation:

$$\sigma_{\text{tot}} \times \text{BR}(W \to \mu\nu\ ) = \frac{N_{\text{data}} - N_{\text{bg}}}{\mathcal{L} \cdot \text{A}_{\text{w}} \cdot \text{C}_{\text{w}}} \tag{5.1}$$

N_{data} is the number of candidate events measured in data. N_{bg} is the number of background events estimated using both Monte Carlo and data driven techniques. The factor, C_{w}, corrects for detector effects and is estimated by simulated events of $W \to \mu\nu$ decays using a full detector simulation. C_{w} is the ratio of the reconstructed events passing all detector-level selection criteria over the theoretical expected events in the fiducial phase space. It is formally defined as:

$$\text{C}_{\text{w}} = \frac{N_{\text{rec, all reco cuts}}}{N_{\text{gen, fid cuts}}}, \tag{5.2}$$

where: $N_{\text{rec, all reco cuts}}$ is the sum of event weights of events passing all analysis cuts (Cuts are discussed in Sec. 5.1) And $N_{\text{gen, fid cuts}}$ is the sum of event weights of events passing fiducial cuts (truth definition and fiducial volume are discussed in this section).

The acceptance factor $\mathrm{A_w}$ is used to extrapolate from the measurement region (i.e. a fiducial volume) to the full phase space and is estimated with Monte Carlo event generators, however, no detector simulation is needed. $\mathrm{A_w}$ is the ratio of the theoretically expected events in the fiducial phase space over all the theoretically expected events. It is defined by

$$\mathrm{A_w} = \frac{N_{\text{gen, fid cuts}}}{N_{\text{gen, no cuts}}}, \tag{5.3}$$

where $N_{\text{gen, no cuts}}$ is the sum of event weights without any kinematic and fiducial cuts applied.

BR$(W \to \mu\nu)$ is the branching ratio of the $W \to \mu\nu$ decay. The number of selected events in data (N_{data}) is firstly measured. And the expected/estimated backgrounds events (N_{bg}) is subtracted from the measured events to get the number of signal events, appropriately weighted and described in more detail in Sec. 5.2. The final production cross section can be obtained from the number of signal events divided by the product of the integrated luminosity ($\mathcal{L}$), the detector acceptance ($\mathrm{A_w}$) and the correction factor ($\mathrm{C_w}$). The integrated luminosity recorded by ATLAS for 8 TeV proton proton collisions is 20.28 pb^{-1}.

The fiducial phase space is defined at generator level by the following cuts on the p_T, absolute pseudorapidity, $|\eta|$ of the decay-muon, the p_{T} of the neutrino, and the W transverse mass, m_T.

- $p_{\mathrm{T}}^{\mu} > 25$ GeV
- $p_{\mathrm{T}}^{\nu} > 25$ GeV
- $|\eta_{\mu}| < 2.5$
- $m_{\mathrm{T}} > 40$ GeV

The selection criteria used to select $W \to \mu\nu$ events in data will be given in the following section.

The corresponding production cross section within the fiducial phase space of the measurement, the so-called fiducial cross section (σ_{fid}) can be derived from the total cross section by multiplying by the acceptance, $\mathrm{A_w}$,

$$\sigma_{\text{fid}} \times \mathrm{BR}(W \to \mu\nu\ ) = \frac{N_{\text{data}} - N_{\text{bg}}}{\mathcal{L} \cdot \mathrm{C_w}} \tag{5.4}$$

The production cross section of the W boson is also measured as a function of the pseudorapidity of the decay muon. The W charge asymmetry is defined in terms of the W^+ and W^- fiducial cross-sections.

The total production cross section, differential in η_μ , in a particular bin i, is given by the following expression:

$$\left(\frac{d\sigma_{\text{tot}}}{d\eta_\mu}\right)^i = \frac{N^i_{\text{data}} - N^i_{\text{bg}}}{\mathcal{L} \cdot (\Delta\eta_\mu\ )^i\, \mathrm{A}^i_{\mathrm{w}}\mathrm{C}^i_{\mathrm{w}}}, \tag{5.5}$$

The fiducial production cross section, differential in η_μ , in a particular bin i, is given by the following expression:

$$\left(\frac{d\sigma_{\text{fid}}}{d\eta_\mu}\right)^i = \frac{N^i_{\text{data}} - N^i_{\text{bg}}}{\mathcal{L} \cdot (\Delta\eta_\mu\ )^i\, \mathrm{C}^i_{\mathrm{w}}}, \tag{5.6}$$

N^i_{data} - N^i_{bg} is the number of signal candidate events measured in data in bin i. The width of bin i is expressed by $(\Delta\eta_\mu\ )^i$. $\mathrm{C}^i_{\mathrm{w}}$ and $\mathrm{A}^i_{\mathrm{w}}$ are the bin-by-bin correction factor and acceptance for bin i.

The muon charge asymmetry variable (A_μ) is finally defined as:

$$\mathrm{A}_\mu = \frac{\sigma^{W^+}_{\text{fid}} - \sigma^{W^-}_{\text{fid}}}{\sigma^{W^+}_{\text{fid}} + \sigma^{W^-}_{\text{fid}}} \tag{5.7}$$

where $\sigma^{W^+}_{\text{fid}}$ and $\sigma^{W^-}_{\text{fid}}$ denote the fiducial cross section of W^+ and W^- production.

The muon charge asymmetry in a particular bin of pseudorapidity, i is defined analogously in terms of the W^+ and W^- fiducial cross-sections in that bin:

$$\mathrm{A}_{\mu,\, i} = \frac{\left(\frac{\sigma_{\text{fid}}^{W^+}}{d\eta_\mu}\right)^i - \left(\frac{\sigma_{\text{fid}}^{W^-}}{d\eta_\mu}\right)^i}{\left(\frac{\sigma_{\text{fid}}^{W^+}}{d\eta_\mu}\right)^i + \left(\frac{\sigma_{\text{fid}}^{W^-}}{d\eta_\mu}\right)^i} \tag{5.8}$$

where the fiducial cross section in the bin i was calculated from Eq. 5.6. The ratio measurement of the W charge asymmetry is defined in order to reduce the contribution of systematic uncertainties that are correlated between W^+ and W^- (for example the luminosity uncertainty completely cancels).

The steps necessary for measuring the W charge asymmetry will be described in detail in the following section. In a first step, it is described how W boson candidate events are selected in the recorded ATLAS data. In a second step, the estimation of the background contamination to the selected data events is detailed. Various data - model comparison plots are then shown, in order to validate the performance of the MC event generators as well as the ATLAS detector simulation. Finally, the correction for detector effects and the associated systematic uncertainties are described in detail.

5.1 Signal Selection

For an event to be considered a genuine $W \to \mu\nu$ candidate event, it must fulfil various selection criteria. During several data taking periods at ATLAS, some detector parts were not working optimally, or the colliding beams were not declared as stable by the LHC operators. In those cases, part or all of a data taking run is not considered suitable for a physics analysis. A so-called "Good Runs List" (GRL) is provided by the ATLAS data quality group, which indicates which lumi blocks are suitable for physics analysis. The application of the GRL is the first selection requirement for data (a GRL is not applied for Monte Carlo). Also it is important to remove events which contain a noise burst in the Liquid Argon Calorimeter (LAr), or with corruption in the Tile Calorimeter as well as possibly incomplete events. [15] Since jets are used during the reconstruction of the missing transverse momentum, it is also necessary to remove the events with jets in problematic calorimeter regions that are not well measured. [17] Therefore, a so-called “Jets Cleaning” is applied. For the common selection for both data and simulation, two selections to reduce the pile-up contribution are applied: there should be at least one primary vertex with at least three associated tracks. The selections described above are summarised in the following:

- Good Runs List (GRL): Event should be in the GRL (Data only)
- veto events with LAr noise burst, reject Tile corrupted events and remove the incomplete events taken during data taking. (Data only)
- at least 1 primary vertex with at least 3 tracks associated
- jet cleaning

5.1.1 $W \to \mu\nu$ selection

The signature of a W boson event used for the charge asymmetry analysis in this thesis is one selected muon and $E_{\mathrm{T}}^{\mathrm{miss}}$ with the optimized algorithm “MET_RefFinal_TST”, see Chapter 4 for more details on $E_{\mathrm{T}}^{\mathrm{miss}}$ studies. The requirement of $E_{\mathrm{T}}^{\mathrm{miss}}$ reduces background events.

For the selection of $W \to \mu\nu$, at least one muon should be triggered by either one of the muon triggers listed below:

- `EF_mu24i_tight`: Here, the transverse momentum of muons at the Event Filter (EF) level is required to be over a threshold of 24 GeV additionally with an isolation requirement (mu24i).
- `EF_mu36_tight`: The transverse momentum of muons at the Event Filter (EF) level is required to be over a hreshold of 36 GeV (mu36).

The single muon trigger `EF_mu24i_tight` fulfils the isolation requirement of $p_T^{cone20}/p_{\mathrm{T}}$ (muon) < 0.12, where p_T^{cone20} is the p_{T} sum of ID tracks in a cone $\Delta\mathrm{R} = \sqrt{\Delta\phi^2 + \Delta\eta^2} = 0.2$ (excluding the muon track itself) and p_{T} (muon) is the muon transverse momentum. More details about the isolation requirement will be described later in this section. The tracks used in the isolation requirement are required to have p_{T} more than 1 GeV and a

z_0, the longitudinal distance between muon and track, has to be within 6 mm. For data up to the run 202668, the z_0 distance cut was changed to be within 10 mm for the isolation requirement in the `EF_mu24i_tight` trigger. [26]

A muon candidate is required to be matched within a ΔR cone to the muon which is triggered.

The tracks of candidate muons are required to pass the criteria listed below:

- $n_{\text{pixel hits}} + n_{\text{dead pixel sensors}} > 0$
- $n_{\text{SCT hits}} + n_{\text{dead SCT sensors}} > 4$
- $n_{\text{pixel holes}} + n_{\text{SCT holes}} < 3$
- Defining $n = n_{\text{TRT hits}} + n_{\text{TRT outliers}}$, if $0.1 < |\eta| < 1.9$ then $n > 5$ and $n_{\text{TRT outliers}} < 0.9n$

Certain requirements are made on the number of hits of the track in the pixel, SCT, and TRT sub-detectors ($n_{\text{pixel hits}}$, $n_{\text{SCT hits}}$, $n_{\text{TRT hits}}$ respectively). A hole is defined as a missing hit in the pixel ($n_{\text{pixel holes}}$) or SCT ($n_{\text{SCT holes}}$), when one would be expected from the track trajectory. The sum of the holes should be less than three. The requirement of hits from all three inner sub-detectors ensures that the tracks originate from the hard scatter and vetoes tracks from cosmic muons. Muon track segments in the inner detector (ID) and the muon spectrometer (MS) are combined using an algorithm which assesses the compatibility of the tracks in both inner detector and muon spectrometer. The fitting for combination of the tracks allows the algorithm to test the compatibility of the calorimeter energy loss with the momentum measurements in the inner detector and muon spectrometer. A related factor for comparison of the momentum measured by the inner detector, muon spectrometer and calorimeter is called momentum balance significance. Several quality criteria can be applied to muon tracks, which remove different amounts of fake tracks (track not originating from the process of interest). In order to achieve a balance between losing signal events and reducing background, the so-called "Medium+" criteria are used. [27] Muons passing all of the above selection criteria are labelled as "good" muons in this analysis.

The isolation requirement which was mentioned briefly in the trigger selection before is also an important selection to veto muons which stem from jets. The isolation factor can be expressed as $I_\mu = p_T^{cone20}/p_{T,\mu}$, the percentage of the sum of the track transverse momentum around the muon in a cone of $\Delta\mathrm{R} = \sqrt{\Delta\phi^2 + \Delta\eta^2} = 0.2$. Some of the background processes with heavy-hadrons decays, or having jets in the final state (such as $t\bar{t}$ production and the multi-jet background) can be rejected with the isolation cut. An isolation cut is applied to the muons at the inner-detector level. The p_T of all the tracks are summed in a cone of radius $\Delta R = 0.2$ around the muon candidate to form the quantity p_T^{cone20} and a cut on the relative isolation $I_\mu < 0.1$ is applied.

A cut on the muon impact parameters (see Sec. 3.2.1 for definition) can also be applied to reduce the contamination from pile-up interactions:

- $|z_0 \sin\theta| < 0.5\,\mathrm{mm}$ (eventually not applied, see below)
- $|d_0/\sigma_{d_0}| < 3$

A study was performed to estimate the impact of applying a cut on the quantity $|z_0 \sin\theta|$, where z_0 is the longitudinal distance between muon track and the primary vertex. Tab. 5.1 shows a comparison of the correction factor C_w obtained from two generators, PowhegPythia8 and Sherpa, when one of the selection cuts is switched off. The model dependence on these correction factors can be estimated by comparing PowhegPythia8 and Sherpa. The difference between the two generators becomes larger when the cut on the muon track $|z_0 \sin\theta|$ selection is applied. Therefore this cut is not used for the default event selection.

The shortest distance between the muon track and the primary vertex, d_0, should be less than three standard deviations (σ) of its uncertainty.

To summarize the $W \to \mu\nu$ candidates selection, the following cuts are applied to require a good event:

- The single-muon triggers
- Trigger Matched

Cut Type	$W^+ \to \mu^+\nu$ ratio pyth./sher.	pythia	sherpa	$W^- \to \mu^-\bar{\nu}$ ratio pyth./sher.	pythia	sherpa
All Cut	1.0294	0.7027	0.6826	1.0284	0.6952	0.6760
No Muon Trk d0	1.0242	0.7072	0.6905	1.0123	0.6954	0.6869
No Muon Iso.	1.0236	0.7045	0.6883	1.0131	0.6931	0.6841
No N$_{trk}$	1.0234	0.7113	0.6950	1.0099	0.6986	0.6918
No Trigger	1.0236	0.7046	0.6883	1.0131	0.6931	0.6841
No Good Muon	1.0236	0.7051	0.6889	1.0136	0.6939	0.6846
No Medium+	1.0224	0.7054	0.6889	1.0132	0.6939	0.6849
No Jet Cleaning	1.0234	0.7049	0.6889	1.0131	0.6936	0.6846
No Muon Trk z0	1.0136	0.7247	0.7150	1.0139	0.7174	0.7075

Table 5.1: The comparison of correction factors with and without the cut of each single event selection.

- Kinematic cuts:
  - $|\eta_\mu| < 2.4$
  - $p_{\mathrm{T}} > 25\,\mathrm{GeV}$
- ID requirement
- $Medium^+$ working point
- Isolation $I_\mu < 0.1$
- Exactly one good (ID+$medium^+$+Isolation+Kinematics) muons
- $|d_0/\sigma_{d_0}| < 3$
- LAr, Tile and Data cleaning
- Jet Cleaning
- $E_{\mathrm{T}}^{\mathrm{miss}} > 25\,\mathrm{GeV}$
- W boson transverse mass cut $W_{m_T} > 40, \mathrm{GeV}$

cuttype	Data	WPlus	WMinus	WSherpa
All	665629213	22871956	15687566	39936634
GRL	665629213	22871956	15687566	39936634
Data Cleaning	664273223	22871956	15687566	39936634
N_{trk}	661396465	22728934	15589379	39726472
Trigger	223045633	9565087	6558924	17013174
$\geq$ one Muon	222954262	9564899	6558794	17012922
p_{T}^{μ}	192078905	8992817	6166850	16130067
η_{μ}	189257064	8815103	6044997	15847203
Medium+	185945778	8804808	6037911	15828321
Muon Trk z0	185945778	8804808	6037911	15828321
Muon Trk d0	155570438	8760290	6007325	15749288
Muon Trk ID	154418071	8745756	5997277	15722093
Muon Iso.	134140503	8722998	5981595	15659407
Trig. Matched	132423067	8722905	5981528	15658912
Jet Cleaning	132232562	8716438	5977138	15642906
$E_{\mathrm{T}}^{\mathrm{miss}}$	92336223	7487488	5134506	12999198
One W Boson	91530693	7487456	5134479	12999072
$\mathrm{W}m_{\mathrm{T}}$	87630430	7399537	5074241	12698664
efficiency %	13.17	32.35	32.35	31.80

Table 5.2: Cut flow for $W \to \mu\nu$ selection for data, W plus MC (PowhegPythia8), W Minus MC (PowhegPythia8), and Sherpa MC.

5.1.2 Cut-flow and Event Selection Efficiency

The cut-flow for the $W \to \mu\nu$ candidates selection which is shown in Tab. 5.2 presents the number of the events after each selection cut sequentially for collision data and Monte Carlo prediction. There are three Monte Carlo predictions used for comparison, the PowhegPythia8 $W \to \mu\nu$ Monte Carlo samples “WPlus”, “WMinus” (separated by charge) and Sherpa v.1.4.1 (not separated by charge). The cut flows presented here are before any calibration has been applied.

The datasets used in this analysis have already had the GRL applied as a pre-selection requirement so no effect is seen in the table. Data cleaning and the Good Run List are only applied on data, the simulated events are not changed by this cut.

The $W \to \mu\nu$ events selection efficiency for data is 13.17% with around 88 million events for both positive and negative charged muon decays. For the prediction, the events selection efficiency for both generators is around 30%.

5.2 Background Estimation

The background estimation is categorized into two parts: The first part described in Sec. 5.2.1 is mainly estimated with Monte Carlo simulation samples which contains the electroweak and $t\bar{t}$ background. The second part described in Sec. 5.2.2 uses a data driven method to estimate the multijet background as it cannot be simulated reliably.

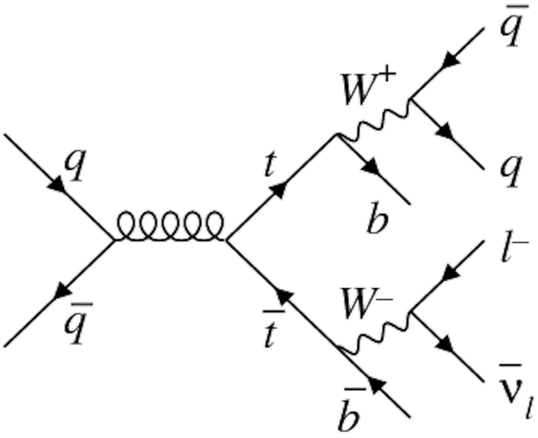

(a)

Figure 5.1: Example of the background process of $t\bar{t}$ is shown in a Feynmann diagram. The processes have one muon at the final state. [5]

5.2.1 Electroweak and $t\bar{t}$

The possible background processes to $W \to \mu\nu$ are W$\to \tau\nu$, $Z \to \mu\mu$, Z $\to \tau\tau$, diboson decays, photon induced background and top processes. The Electroweak and $t\bar{t}$ background can be accurately modeled by Monte Carlo simulation. [21] The background from W$\to \tau\nu$ comes mainly from leptonic tau decays $\tau \to \mu\nu\nu$. In the case one of the muons from the $Z \to \mu\mu$ process is outside the detector acceptance range, this muon will contribute to the $E_{\mathrm{T}}^{\mathrm{miss}}$ and imitate a signal $W \to \mu\nu$ event. The process Z $\to \tau\tau$ contributes to the background when one of the tau decays leptonically $\tau \to \mu\nu\nu$. The production of top-anti-top pairs $t\bar{t}$ in its leptonic decay channel contributes a smaller background due to its lower production cross section. [78] The photon induced background $\gamma\gamma \to \mu\mu$ has similarly two muons in the final state. In the case one of the muons is outside the detector acceptance range, the photon induced process can be mis-identified as a $W \to \mu\nu$ event.

The uncertainties on the background come from their cross section estimation. The cross section uncertainty of W$\to \tau\nu$, $t\bar{t}$, $Z \to \mu\mu$ and Z $\to \tau\tau$ is around 5%. The uncertainties of WW production cross section is about 10%. For ZZ and WZ, the uncertainty are around 2% and 4% respectively. The photon induced process has about 40% uncertainty on their cross section estimation. [21]

The same event selection is applied to background Monte Carlo as is also applied to the data and signal Monte Carlo selection described in Sec. 5.1.1. The detailed cut flow for all the Electroweak and $t\bar{t}$ backgrounds is shown in Tab. 5.3. The number of selected events shown in Tab. 5.3 are not scaled to the data luminosity. The number of selected background events, scaled to the data luminosity, is shown in Tab. 5.5. The event selection efficiency is shown in Tab. 5.4 with the number of selected events, which is again not scaled to the data luminosity.

The $W \to \mu\nu$ events selection efficiency for data is about 13% and the efficiency for signal Monte Carlo is around 32%. All the dominate backgrounds have enough events after selection to avoid statistical fluctuations.

5.2.2 Multi-jet background

The so-called multi-jet background has contributions from a variety of processes such as the semileptonic decays of b- and c-quarks, or in-flight decays of pions or kaons within the tracking region. One example Feynman diagram is shown in Fig. 5.2. The long-lived hadrons passing through the calorimeter can also fake the muon signal and become a source of background. The isolation cut on the muons can help to reject this type of background.

The multi-jet background estimation cannot be perfectly predicted by Monte Carlo and therefore a fully data driven method has to been used.

The multi-jet background template is constructed from a jet-enriched control region in data by reversing or relaxing the muon isolation requirements. The control region is basically the same as $W \to \mu\nu$ signal selection described in Sec. 5.1.1 but with a different isolation selection. The detailed methodology of selecting the control region and how to obtain the normalisation factor for the multi-jet template is described in [11]. The muon triggers used for the

cuttype	$W^+ \rightarrow \tau^+\nu$	$W^- \rightarrow \tau^-\bar{\nu}$	ZZ	WW	WZ	$Z \rightarrow \mu\mu$ veto μ	$Z \rightarrow \mu\mu$ 1μ	$Z \rightarrow \mu\mu$ 2μ	$Z \rightarrow \mu\mu$ $20 < M < 60$	$Z \rightarrow \mu\mu$ $8 < M < 20$
All	3999494	2994896	245000	2499890	999998	2993896	14996072	49150709	9888382	2969991
N$_{trk}$	3989515	2987951	244417	2492494	997395	2984200	14881170	48790392	9796095	2964844
Trigger	56865	44413	71035	721878	283191	17	7845429	42549926	2465351	929035
One Muon	56865	44411	71035	721860	283189	17	7845307	42549913	2465350	929035
p_{T}^{μ}	46466	36604	69661	690957	273055	10	7245107	41969397	1959040	795160
η_μ	45539	36025	69038	681606	270041	10	6989444	41749771	1932501	784645
Medium+	45490	35984	68999	680794	269754	9	6983816	41731009	1930240	783715
Muon Trk d0	45242	35774	67284	670526	264929	5	6948483	41684054	1921728	780357
Muon Trk ID	45176	35725	67230	669348	264507	5	6938821	41668743	1919094	779314
Muon Iso.	45053	35613	66523	664174	262339	2	6920659	41638683	1915069	764950
Trig. Matched	45051	35609	59263	658024	251791	2	6920631	35556844	1835306	743895
Jet Cleaning	45026	35583	59099	656502	251171	2	6896807	35513754	1833814	743040
$E_{\mathrm{T}}^{\mathrm{miss}}$	31622	24628	28124	517984	178905	2	5045562	5781568	282096	164243
One W Boson	31622	24628	16651	500042	159573	2	5045558	2792513	246895	143079
Wm_{T}	27915	21490	13884	455309	142126	1	4940978	2461799	191250	111965

cuttype	$t\bar{t}$	$\gamma\gamma \rightarrow \mu\mu$ $7 < M < 20$	$\gamma\gamma \rightarrow \mu\mu$ $20 < M < 60$	$\gamma\gamma \rightarrow \mu\mu$ $60 < M < 200$	Z $\rightarrow \tau\tau$ Np0	Z $\rightarrow \tau\tau$ Np1	Z $\rightarrow \tau\tau$ Np2	Z $\rightarrow \tau\tau$ Np3	Z $\rightarrow \tau\tau$ Np4
All	49973332	500000	499900	500000	5469593	2433994	493996	176700	31700
N$_{trk}$	49967028	465824	447839	469625	5415362	2428559	493643	176661	31698
Trigger	11751821	13582	31724	131746	896101	482611	105693	39984	7560
One Muon	11751701	13582	31724	131745	896092	482608	105691	39984	7560
p_{T}^{μ}	11314851	10667	23843	122424	751497	425966	94912	36405	6911
η_μ	11256254	10497	23421	121161	739732	419993	93613	35938	6828
Medium+	11239657	10488	23394	121076	738926	419487	93496	35889	6821
Muon Trk d0	10810208	10426	23282	120670	642033	343427	74221	27468	5092
Muon Trk ID	10787403	10408	23252	120584	641006	342807	74080	27426	5082
Muon Iso.	10449422	10313	23228	120494	639657	341688	73598	27132	5005
Trig. Matched	10292567	10226	22359	107651	627532	336350	72311	26634	4887
Jet Cleaning	10274280	10200	22323	107395	627042	335923	72181	26569	4870
$E_{\mathrm{T}}^{\mathrm{miss}}$	8921687	1641	3356	30248	173397	152138	43279	18439	3679
One W Boson	8549340	1593	3146	26000	169680	147202	41613	17663	3537
Wm_{T}	6976230	1294	2605	25055	157340	78569	17934	6700	1242

Table 5.3: Cut flow for $W \rightarrow \mu\nu$ selection for Electroweak and $\bar{t}t$ background samples

Samples	Effieiency	Evts.Selected	/ All Events
Data	0.1317	87630430	/ 665629213
$W^+ \rightarrow \mu^+\nu$ PowhegPythia8	0.3235	7399537	/ 22871956
$W^- \rightarrow \mu^-\bar{\nu}$ PowhegPythia8	0.3235	5074241	/ 15687566
$W \rightarrow \mu\nu$ Sherpa	0.3180	12698664	/ 39936634
$W^+ \rightarrow \tau^+\nu$	0.0070	27915	/ 3999494
$W^- \rightarrow \tau^-\bar{\nu}$	0.0072	21490	/ 2994896
$t\bar{t}$	0.1396	6976230	/ 49973332
ZZ	0.0567	13884	/ 245000
WW	0.1821	455309	/ 2499890
WZ	0.1421	142126	/ 999998
$Z \rightarrow \mu\mu\ veto - \mu$	0.0000	1	/ 2993896
$Z \rightarrow \mu\mu\ \ 1\mu$	0.3295	4940978	/ 14996072
$Z \rightarrow \mu\mu\ \ 2\mu$	0.0501	2461799	/ 49150709
$Z \rightarrow \mu\mu\ 20 < M < 60$ GeV	0.0193	191250	/ 9888382
$Z \rightarrow \mu\mu\ 8 < M < 20$ GeV	0.0377	111965	/ 2969991
$\gamma\gamma \rightarrow \mu\mu\ 7 < M < 20$ GeV	0.0026	1294	/ 500000
$\gamma\gamma \rightarrow \mu\mu\ 20 < M < 60$ GeV	0.0052	2605	/ 499900
$\gamma\gamma \rightarrow \mu\mu\ 60 < M < 200$ GeV	0.0501	25055	/ 500000
Z $\rightarrow \tau\tau$ Np0	0.0288	157340	/ 5469593
Z $\rightarrow \tau\tau$ Np1	0.0323	78569	/ 2433994
Z $\rightarrow \tau\tau$ Np2	0.0363	17934	/ 493996
Z $\rightarrow \tau\tau$ Np3	0.0379	6700	/ 176700
Z $\rightarrow \tau\tau$ Np4	0.0392	1242	/ 31700

Table 5.4: $W \rightarrow \mu\nu$ event selection efficiency for all the data, signal MC and background MC which is used in this analysis. The event efficiency is defined as the events passing the selection cuts over the all events. The efficiency for data is about 13% and the efficiency for signal Monte Carlo is around 32%.

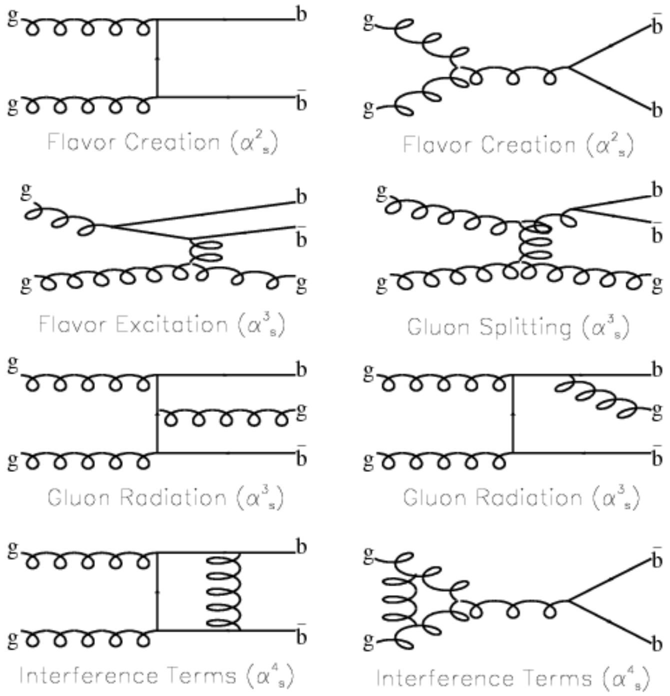

(a) Multi-jets background

Figure 5.2: Examples of the multi-jets background process are shown in eight Feynmann diagrams. [6]

signal selection have an intrinsic isolation requirement. In order to relax the isolation from the trigger, another trigger without an isolation requirement is used for the multi-jet background template selection (`EF_mu24_tight`). The trigger and isolation requirements for the template is as follow:

- `EF_mu24_tight` or `EF_mu36_tight`
- $0.14 < I_{\mu} < 0.18$

The non-isolated trigger `EF_mu24_tight` is prescaled by a factor of 10 after the data period A, i.e. only one tenth of the data was triggered by `EF_mu24_tight` if the event run number was larger than 201556. The trigger `EF_mu36_tight` is un-prescaled in all data periods. [26] Therefore in order to obtain the corresponding event number after the selection of the template, the events which only pass the `EF_mu24_tight` trigger but not pass the `EF_mu36_tight` trigger are scaled ten times more.

	W$^+$	xx/data %	W$^-$	xx/data %
Data	51670285.000	(100.000)	35960143.000	(100.000)
$W \rightarrow \mu\nu$	46640853.933	(90.266)	32127397.297	(89.342)
$t\bar{t}$	195286.142	(0.378)	195137.598	(0.543)
Z $\rightarrow \tau\tau$	14883.396	(0.029)	13934.469	(0.039)
$W \rightarrow \tau\nu$	1059582.931	(2.051)	779785.600	(2.169)
$Z \rightarrow \mu\mu$	1624582.725	(3.144)	1447549.326	(4.025)
QCD	1995530.175	(3.862)	1838281.791	(5.112)
Diboson	61988.343	(0.120)	57957.918	(0.161)
$\gamma\gamma \rightarrow \mu\mu$	1353.546	(0.003)	1336.515	(0.004)
AllBkg	4953207.258	(9.586)	4333983.217	(12.052)

Table 5.5: The ratio of signal Monte Carlo, background Monte Carlo and estimated QCD background over data after event selection and with Monte Carlo samples scaled to the data luminosity.

The normalisation factors for the multi-jet background template are determined by fitting the template in three discriminating variables: the $E_{\mathrm{T}}^{\mathrm{miss}}$, m_{T} and the ratio $p_{\mathrm{T}}^{\mu}/m_{\mathrm{T}}$ [11]. The uncertainty will be detailed in Sec 5.4.7.

5.2.3 Background and signal ratio

The total estimated background (Electroweak, $t\bar{t}$ and multi-jet) for $W^+ \rightarrow \mu^+\nu$ is about 9% and for $W^- \rightarrow \mu^-\bar{\nu}$ is about 12% of the selected data. The dominating background is multi-jet background forming 3.86% of data for $W^+ \rightarrow \mu^+\nu$ and forming 5.11% for $W^- \rightarrow \mu^-\bar{\nu}$. $Z \rightarrow \mu\mu$ is the second largest background for $W \rightarrow \mu\nu$ events. The amount of each background as a fraction of data is shown in Table 5.5.

The total number of the $Z \rightarrow \mu\mu$ background of $W^+ \rightarrow \mu^+\nu$ is around 3% higher than $W^- \rightarrow \mu^-\bar{\nu}$. The positive and negative muons have different η_μ distributions because of the Z boson decays forward backward asymmetry [19]. Negative muons from Z boson decays have a broader η_μ distribution than positive ones, therefore more negative muons are cut by the $|\eta| < 2.4$ requirement.

Fig. 5.3 shows the ratio of the estimated number of backgrounds events over selected data in bins of the muon pseudorapidity. In the lower muon pseudorapidity region, the multi-jet background dominates. In the higher muon pseudorapidity region, $Z \rightarrow \mu\mu$ is the largest background. $W \rightarrow$

$\tau\nu$ is the third largest background and distributed evenly over all muon pseudorapidity regions.

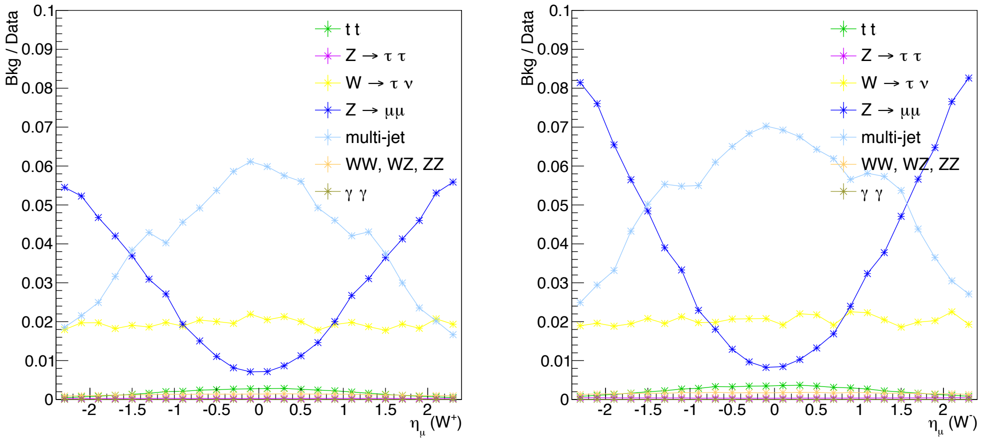

(a) WPlus (b) WMinus

Figure 5.3: The background ratio (number of the events from background over the number of the events from data after $W \to \mu\nu$ event selection) as a function of the muon pseudorapidity.

5.3 Corrections to the Detector Description in Simulations

The Monte Carlo prediction is simulated under various conditions which do not necessarily fully reflect those under which the data was recorded. The Monte Carlo prediction must therefore be reweighted to correct for these various effects. The weights are derived from comparison of the prediction with data and are applied at the truth level (and therefore also affect the reconstruction level).

5.3.1 Pile-up reweighting

The level of pileup in each event is quantified by the average number of inelastic interactions per bunch crossing, μ. It can be estimated by using the instantaneous luminosity, the inelastic pp cross-section and the corresponding beam parameters for the relevant luminosity blocks. All Monte Carlo samples are reweighted in μ to reflect the pile-up conditions of the data-set which is used for this measurement. In addition, the value of μ is scaled in data by a factor ~ 0.92 due to the 9% error (1/1.09) from the comparison between number of primary vertices and the average number of inelastic interactions per bunch crossing of Monte Carlo. [14].

5.3.2 Reweighting of the z position of primary vertex

The simulation of the beam spot in Monte Carlo samples is rather different from the actual beam spot in 2012 data. This difference affects the modelling of the angular acceptance as well as the lepton reconstruction. In order to exclude possible problems from the differing data/Monte Carlo distributions, the Monte Carlo was reweighted using the information from the z-coordinate of the hard interaction ($zpos$). [16]

Comparisons between data and signal PowhegPythia Monte Carlo for the distribution of the z-coordinate of the hard interaction after reweighting are presented in Fig. 5.4. The agreement between reweighted Monte Carlo and data is good but not perfect, because the shape of the distribution has a small dependence on the applied selection.

5.3.3 Trigger efficiency

The efficiency of triggering (number of triggered muons over all muons) was estimated in Monte Carlo before the data taking according to the previous year's collision runs. Therefore the efficiency of triggering in data and Monte Carlo may not be the same. The efficiency predicted by Monte Carlo therefore is corrected using trigger scale factors to match data. Trigger scale factors are derived using the "tag-and-probe method". $Z \to \mu\mu$ events are used for the tag-and-probe method as a very low-background sample can be selected. A "tag" muon of $Z \to \mu\mu$ is required to be trigger-matched. The other muon from the same $Z \to \mu\mu$ event is used as a "probe" muon which is checked if it also was trigger matched. The ratio of matched probes to total probes is the trigger efficiency. The trigger scale factors are then defined as the ratio between the data and Monte Carlo trigger efficiencies. Two sets of trigger scale factors are developed by the ATLAS muon performance group (MCP) [26] and the High Mass Drell-Yan analysis group (HMDY) [62]. The

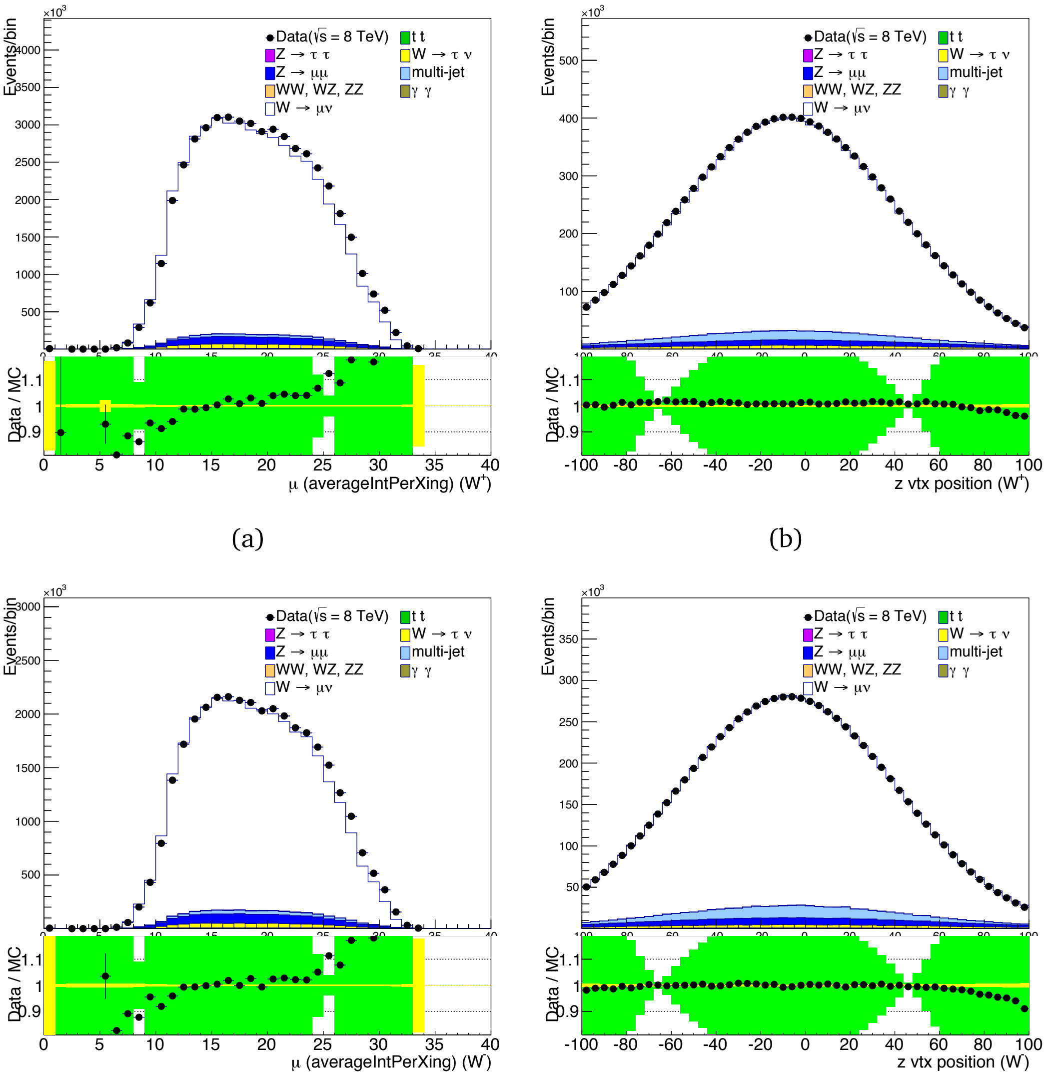

(a) (b)

(c) (d)

Figure 5.4: Data-Monte Carlo comparison plots of the pile-up variable $< \mu >$ and Z vertex position distribution for WPlus and WMinus events to check the pileup reweighting and z position of primary vertex reweighting. The green bands in the ratio distributions correspond to the total systematic uncertainty, and the yellow bands are the Monte Carlo statistical uncertainties.

Systematic Type	W^+ Variation(%)	W^- Variation(%)
HMDY TrigDown	-0.411	-0.114
MCP TrigDown	1.728	1.737
HMDY TrigUp	0.397	0.108
MCP TrigUp	-1.728	-1.737

Table 5.6: The systematic uncertainty variation for W^+ and W^- by applying different trigger scale factors. It is about 4 time higher uncertainty after applying MCP trigger scale factor than applying the HMDY trigger scale factor for $W^+ \to \mu^+\nu$, and is about 15 times higher for $W^- \to \mu^-\bar{\nu}$.

systematic uncertainties of the cross-section measurement is significantly smaller using the trigger scale factors developed by the High Mass Drell-Yan analysis group. Tab. 5.6 shows the difference of the associated systematic uncertainties for the two different trigger scale factors sets. The agreement between data and Monte Carlo in the muon η_μ distribution is much better after applying the HMDY scale factors than the MCP trigger scale factors, as shown in Fig. 5.5. Therefore the trigger scale factor developed by High Mass Drell-Yan analysis group is used in this analysis.

5.3.4 Momentum scale and resolution

The muon momentum scale and momentum resolution in Monte Carlo samples are corrected to data using an externally provided muon momentum correction tool [25]. This calibration has been done by using the Z boson mass. The muon four vector is constructed using the corrected transverse momentum, muon η and ϕ and the mass of the muon which is provided from the Particle Data Group (PDG) [83].

There is one source of muon momentum scale uncertainty provided, and two sources of muon momentum resolution uncertainty:

- momentum scale up/down, by scaling up and down the muon transverse momentum within its 1 σ uncertainty.
- ID resolution up/down, by scaling up and down the muon track transverse momentum measured in the inner detector within its 1 σ uncertainty.

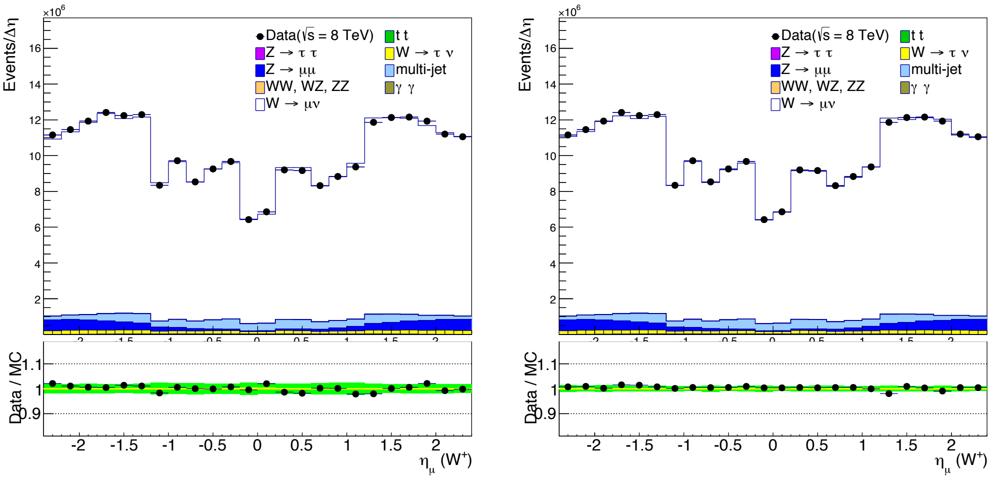

(a) MCP Trigger SF $W^+ \to \mu^+\nu$ (b) HMDY Trigger SF $W^+ \to \mu^+\nu$

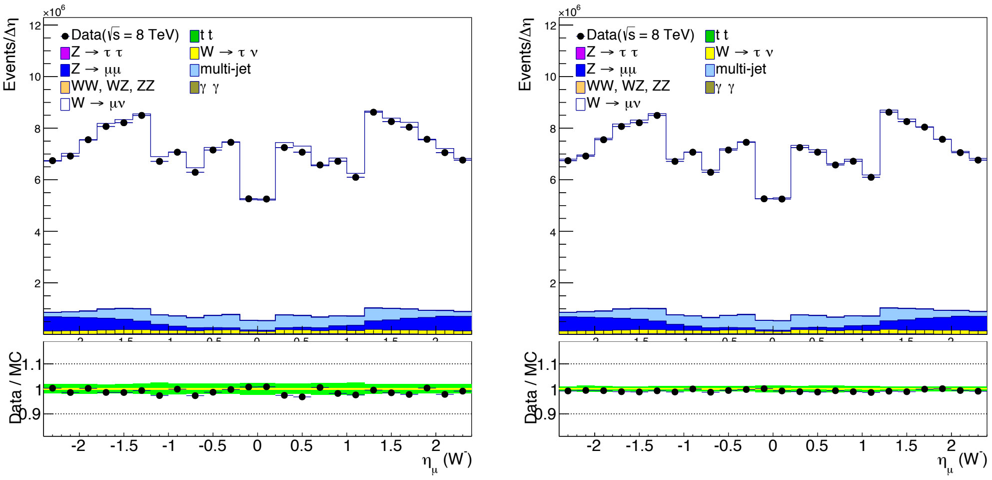

(c) MCP Trigger SF $W^- \to \mu^-\bar{\nu}$ (d) HMDY Trigger SF $W^- \to \mu^-\bar{\nu}$

Figure 5.5: The muon η_μ distribution in data and Monte Carlo with the MCP (SFs are provided by Muon Combined Preference group) Trigger SFs (left) and HMDY (SF used for High Mass Drell Yan analysis) trigger SFs (right) applied. The MCP trigger scale factors has a larger associated systematic uncertainty (the green band) than the HMDY trigger scale factors. A better data and Monte Carlo agreement can be also observed after the HMDY trigger scale factors are applied.

- MS resolution up/down, by scaling up and down the muon track transverse momentum measured in the muon spectrometer within its 1 σ uncertainty.

5.3.5 Muon reconstruction and isolation efficiency

Muon reconstruction efficiency and isolation correction scale factors, which were provided by MuonEfficiencyCorrections tool [24], are applied to muons in Monte Carlo samples to correct for differences in reconstruction efficiencies between data and Monte Carlo. A similar "tag-and-probe method" as used for muon trigger efficiency is used for the muon reconstruction and isolation efficiency correction. [20]

Muon momentum scale, jet energy scale and soft term related corrections are applied by smearing their four vectors. The other corrections of muon trigger efficiency, reconstruction and isolation efficiency, pile-up reweighting and Z vertex position reweighting are applied in the event weight. The event weights, applied for reconstructed information (SF_{evt}) are calculated as:

$$SF_{evt} = SF_{trig} \cdot SF_{rec} \cdot SF_{iso} \cdot SF_{zpos} \cdot SF_{<\mu>}, \tag{5.9}$$

where SF_{trig} is a trigger efficiency correction scale factor, SF_{rec} is the reconstruction efficiency correction factor, SF_{iso} is the isolation efficiency correction factor, SF_{zpos} is the Z vertex position correction factor for the collision and $SF_{<\mu>}$ is the pile-up reweighting correction.

5.3.6 Control plots

The event selection, the estimation of the background contribution and the model corrections are tested by producing data-Monte Carlo comparison distributions for various parameters of interest (so-called control plots). The electroweak and multi-jet background contaminations are added to the signal Monte Carlo in order to be able to perform a comparison with data. The background components were extracted with the methods described in Sec. 5.2. The number of multi-jet background events was extracted over all bins and the shape is taken from a data-driven background template (Sec 5.2.2).

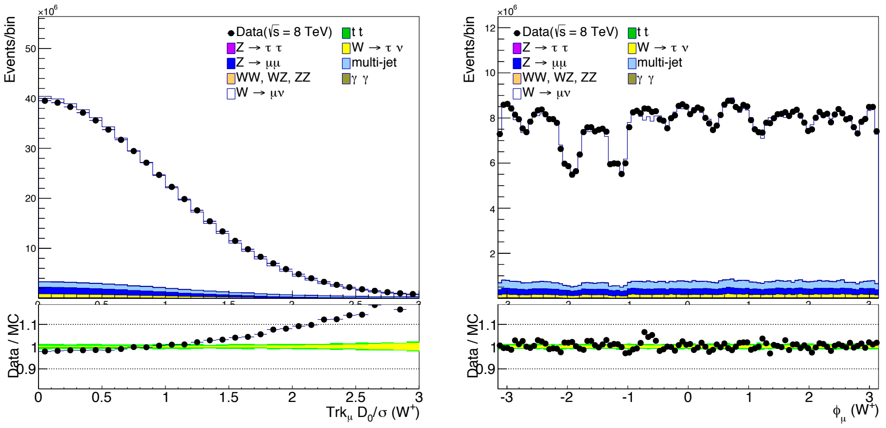

(a) Muon Track d_0 (b) Muon ϕ

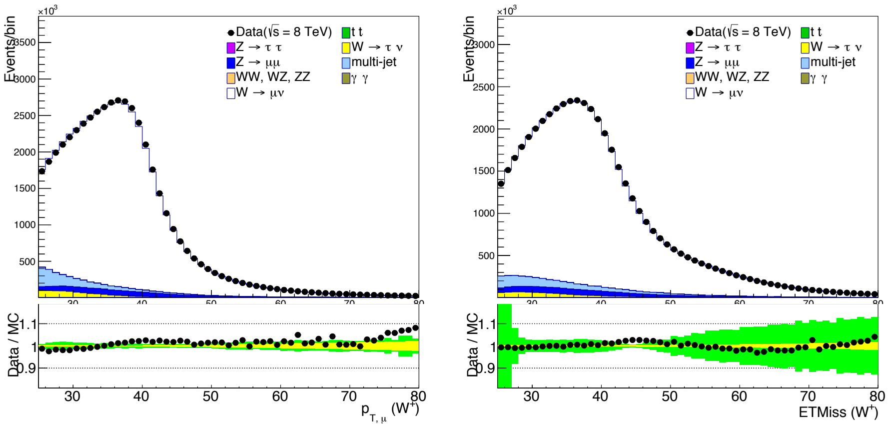

(c) Muon p_{T} (d) $E_{\mathrm{T}}^{\mathrm{miss}}$

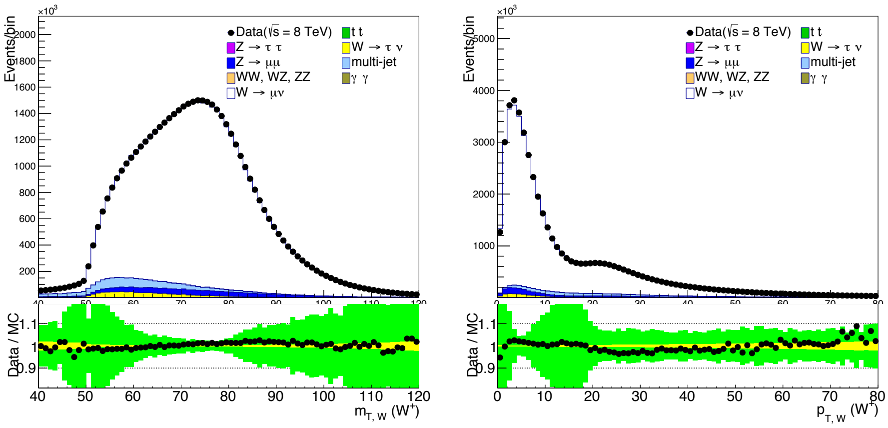

(e) $m_{T,w}$ (f) $p_{T,w}$

Figure 5.6: The control plots for $W^+ \to \mu^+\nu$ events. The green bands in the ratio distributions correspond to the total systematic uncertainty, and the yellow bands are the Monte Carlo statistical uncertainties. The two dips structure in the muon ϕ plot are the supporting structures of the ATLAS detector. And the bump in the W p_{T} plot is a consequence of the jet selection for the $E_{\mathrm{T}}^{\mathrm{miss}}$ hard term.

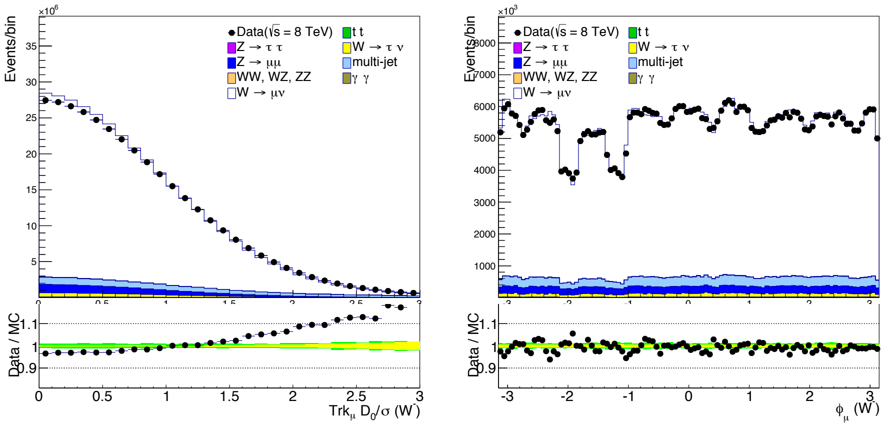

(a) Muon Track d_0

(b) Muon ϕ

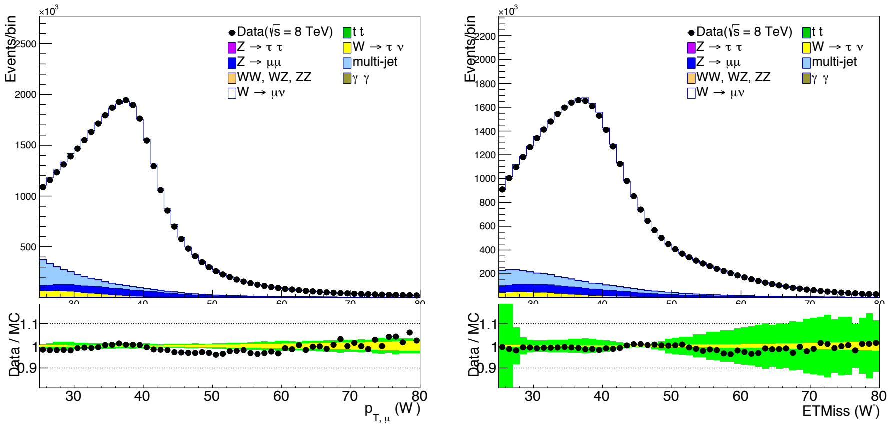

(c) Muon p_{T}

(d) $E_{\mathrm{T}}^{\mathrm{miss}}$

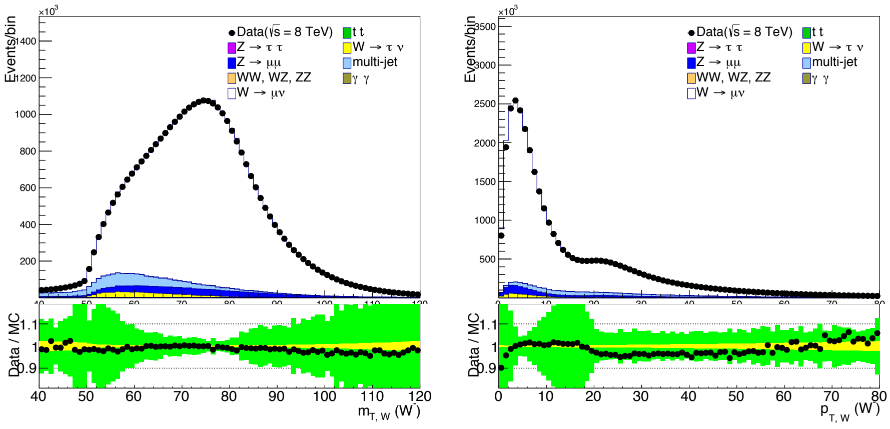

(e) $m_{T,w}$

(f) $p_{T,w}$

Figure 5.7: The control plots for $W^- \rightarrow \mu^-\bar{\nu}$ events. The green bands in the ratio distributions correspond to the total systematic uncertainty, and the yellow bands are the Monte Carlo statistical uncertainties. The distributions are similar to $W^+ \rightarrow \mu^+\nu$.

The main control plots are shown for $W^+ \to \mu^+\nu$ in Fig. 5.6 and for $W^- \to \mu^-\bar{\nu}$ in Fig. 5.7. The distribution of the muon transverse angle ϕ_μ (top right Fig. 5.6 and Fig. 5.7) shows two regions with fewer events around $\phi_\mu = -1$ and $\phi_\mu = -2$ where the supporting structures of the muon spectrometer are. A better agreement in the lower kinematics range of the muon transverse momentum, missing transverse momentum and W boson transverse momentum distributions are observed. The bump in the W boson transverse momentum is due to the cut on the jet transverse momentum in the hard term of the missing transverse momentum. All presented plots demonstrate reasonable agreement between data and Monte Carlo simulation.

The total statistical and systematic uncertainties are plotted on the data-Monte Carlo comparison plots in Fig. 5.6, Fig. 5.7 and Fig. 5.8. The green bands in the ratio distributions correspond to the total systematic uncertainty, and the yellow bands are the Monte Carlo statistical uncertainties. The difference between data and simulation in all the distributions are covered by the uncertainties.

5.3.7 The choice of the binning

The charge asymmetry of the W boson is measured as a function of the pseudorapidity of the decay muon, η_μ . The choice of the binning is determined by the level of agreement of the data and prediction within the statistical and systematic uncertainties. Firstly the choice of the binning is driven by the statistics available for the selected signal events and related backgrounds. It also depends on the binning of the scale factors which are applied to correct for detector effects. For example, the trigger scale factors can only be applied if the bin size in η_μ is greater than 0.2.

Three different binnings have been tested within this thesis:

- The fine binning (from η_μ of -2.4 to 2.4 in steps of 0.1)

- The coarse binning (from η_μ of -2.4 to 2.4 in steps of 0.2)

- The absolute η_μ binning using the same bin edges as the $\sqrt{s} = 7$ TeV analysis (0, 0.21, 0.42, 0.63, 0.84, 1.05, 1.37, 1.52, 1.74, 1.95, 2.18, 2.4)

The distributions of the muon pseudorapidity η_μ of W^+ and W^- candidates after the final selection are shown in Fig. 5.8 with three different binnings choices. The coarse binning in steps of 0.2 on the top row of Fig. 5.8 shows almost perfect agreement between data and Monte Carlo. The fine binning plots in steps of 0.1 in the middle row of Fig. 5.8 have good data/Monte Carlo agreement but there is some fluctuation from statistics and effects that the coarse trigger scale factors cannot capture. The same binning as the 7 TeV analysis [22] shown in the bottom row of Fig. 5.8 also has very good data and Monte Carlo agreement.

A second factor which the binning choice is assessed upon is the fraction of reconstructed events falling in the same η_μ bin as the truth events, the so-called "purity" of the binning. A higher purity provides more reliable results when using a bin-by-bin unfolding technique. Fig. 5.9 shows the purity using three different binning of η_μ .

The purity of the binning in steps of 0.2 and the absolute binning of 7 TeV is above 99%. The purity of the binning in steps of 0.1 is slightly smaller, but still over 98%. As the purity is high enough, it shows the bin-by-bin correction is suitable to be used in this analysis and a more sophisticated unfolding technique such as Bayesian iterative unfolding is not needed.

Fig. 5.10 shows the results of the muon charge asymmetry with these three different binnings. All the systematic and statistical uncertainties are included for these three different binnings and are shown as the blue band in the plots. For both coarse and the absolute η_μ binnings, the muon charge asymmetry follows the same trend and has a reasonable total uncertainty. The scattered data points observed in the fine binning plot is due to the fact that the 0.1 step binning is finner than the default binning of the trigger scale factors. In order to gain more physics information and avoid a bias from the trigger scale factors, the coarse binning with 0.2 steps is chosen for all the following analysis.

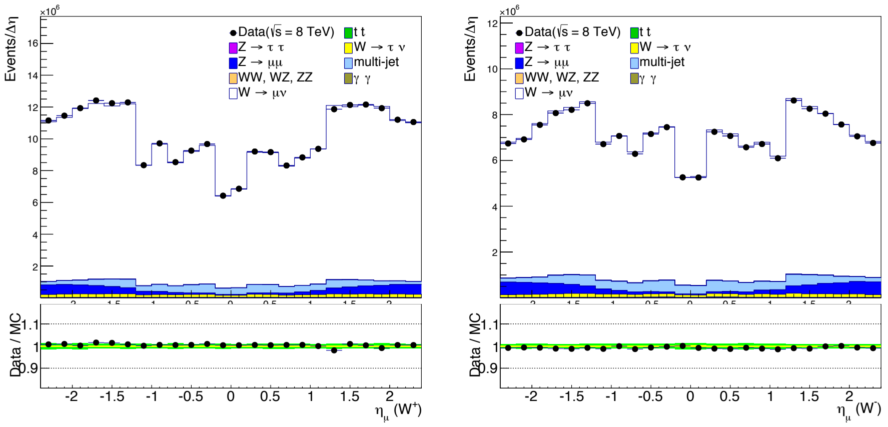

(a) η_μ $W^+ \rightarrow \mu^+\nu$

(b) η_μ $W^- \rightarrow \mu^-\bar{\nu}$

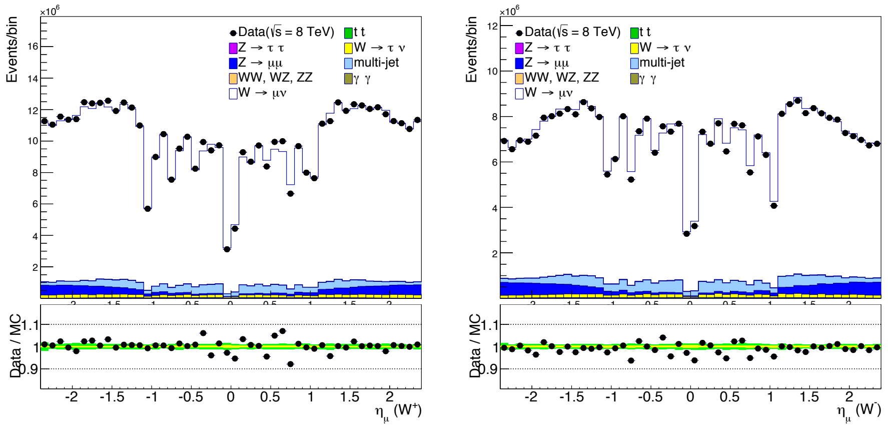

(c) η_μ Fine Binning W^+

(d) η_μ Fine Binning W^-

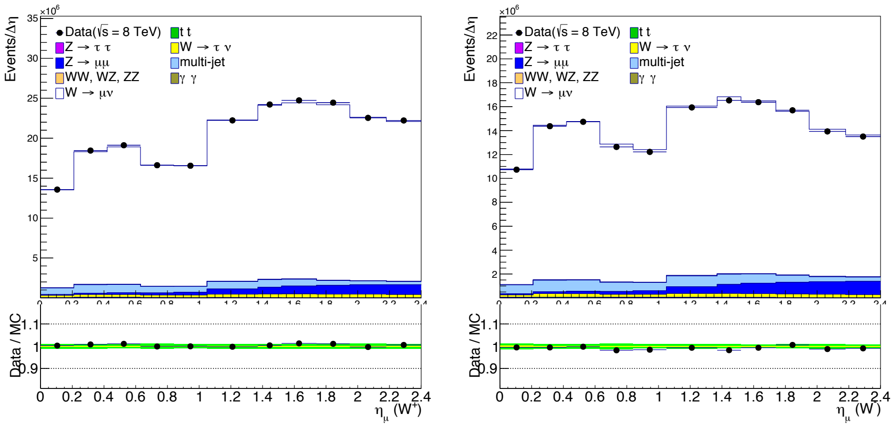

(e) η_μ 7TeV Binning W^+

(f) η_μ 7TeV Binning W^-

Figure 5.8: The control plots of the muon η_μ distribution for $W^+ \rightarrow \mu^+\nu$ and $W^- \rightarrow \mu^-\bar{\nu}$ events. Three different binnings of muon η_μ are shown. The η_μ distributions with the finest binning have some fluctuation with around 10% data / Monte Carlo difference.

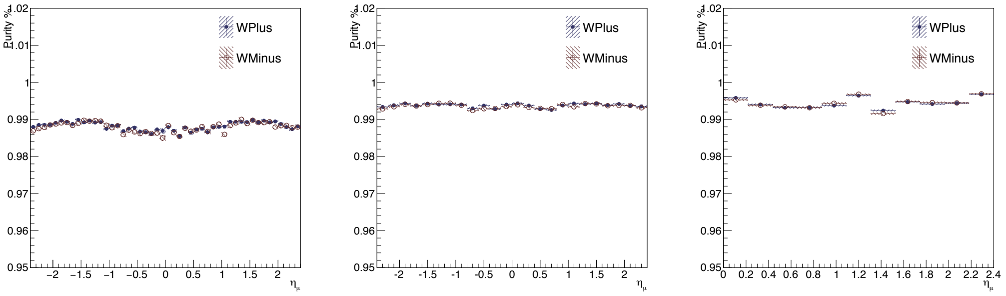

(a) Binning 0.1 Step (b) Binning 0.2 Step (c) Binning $\sqrt{s}$ = 7 TeV

Figure 5.9: The purity of muon pseudorapidity with three different binning, the fine binning in steps of 0.1, the coarse binning in steps of 0.2 and the binning the same as the $\sqrt{s}$ = 7 TeV analysis.

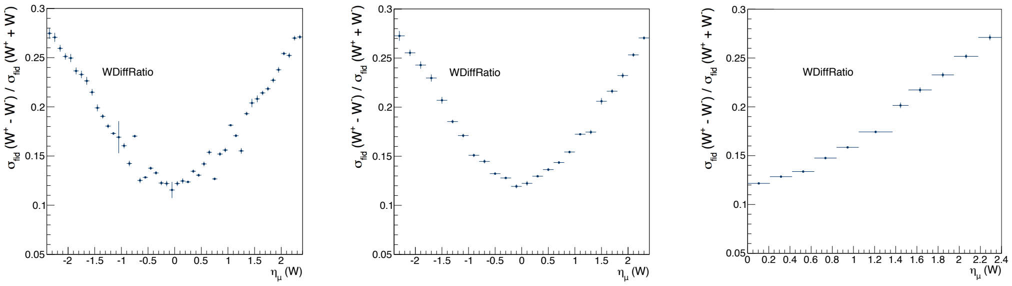

(a) Binning 0.1 Step (b) Binning 0.2 Step (c) Binning $\sqrt{s}$ = 7 TeV

Figure 5.10: The muon charge asymmetry distribution as a function of the η_μ with three different binning, the fine binning in steps of 0.1, the coarse binning in steps of 0.2 and the binning the same as the $\sqrt{s}$ = 7 TeV analysis.

5.4 Systematic and statistical uncertainties

In addition to the statistical uncertainty arising from the limited number of events in data, several sources of systematic uncertainties are also considered in this analysis.

The cross-section and W boson charge asymmetry measurements rely on various corrections, which were applied to the Monte Carlo prediction. Each of these corrections has statistical and systematic uncertainties, which need to be propagated to the measured cross sections and W boson charge asymmetry.

The method which is used to propagate the uncertainties is the so-called offset method. In the offset method, Monte Carlo corrections are varied up and down everywhere by the systematic uncertainty under study. The distributions are calculated for up and down variations of the corresponding Monte Carlo correction, and then cross-sections σ^{up} and σ^{down} are calculated using this information. The systematic uncertainty is defined as the average of the absolute up variation $\Delta = |\sigma^{\mathrm{up}} - \sigma^{\mathrm{nominal}}|$ and the absolute down variation $\Delta = |\sigma^{\mathrm{nominal}} - \sigma^{\mathrm{down}}|$. [35] [29]

Statistical uncertainties are always considered as uncorrelated between the bins in which they were derived.

The experimental uncertainties for the presented analysis mostly come from mis-modelling of the detector or beam conditions during a run. The experimental uncertainties of muon reconstruction, $E_{\mathrm{T}}^{\mathrm{miss}}$ reconstruction, pile-up and z position of the primary vertex will be presented in the following sections.

5.4.1 Statistical uncertainties

Both data and Monte Carlo predictions have limited events which are selected which introduces some statistical uncertainties. The statistical uncertainty is estimated by assuming the event counts follows a Poisson distribution. For the non-weighted events, like data, the statistical uncertainty is equal to the square root of the event counts. For the weighted events, like the Monte Carlo prediction with corresponding corrections, the statistical uncertainty is estimated by the sum of weights squared in the bin.

5.4.2 Muon related uncertainties

For each of the muon related corrections described in Sec. 5.3, there is an associated systematic uncertainty:

- Muon momentum scale and resolution
- Muon reconstruction efficiency

- Muon isolation efficiency
- Muon trigger efficiency

Each of the corrections is provided with one statistical and one systematic uncertainty. Since the statistical uncertainties are very small, both uncertainties are summed and propagated with the offset method as one source. The biases related to the tag and probe procedure are included for the muon reconstruction, isolation and trigger efficiencies. The extrapolation of the scale factors to very high or low transverse momentum is a source of systematic uncertainty for the muon resolution and isolation efficiencies. [20]

5.4.3 Jet energy scale for the hard term of the $E_{\mathrm{T}}^{\mathrm{miss}}$ reconstruction

The $E_{\mathrm{T}}^{\mathrm{miss}}$ is reconstructed from the vector sum of the transverse momenta of high $\mathrm{p_T}$ physics objects and the track soft term, as described in Sec. 4.4. The estimated uncertainty on the energy scale of jets is propagated into the $E_{\mathrm{T}}^{\mathrm{miss}}$. The uncertainty on the muon hard term is not considered separately in the $E_{\mathrm{T}}^{\mathrm{miss}}$, as it is expected to be small with respect to the uncertainty on the signal muon from the W boson decay, and covered by the uncertainty on the muon which is from the W boson decay. There are very rare contributions from the other high $\mathrm{p_T}$ physics objects of, e.g. electrons, photon and tau in the $W \rightarrow \mu\nu$ events. Therefore the uncertainties from the other physics objects are considered negligible for the $E_{\mathrm{T}}^{\mathrm{miss}}$ reconstruction.

5.4.4 Track soft term scale and resolution of the $E_{\mathrm{T}}^{\mathrm{miss}}$ reconstruction

A systematic uncertainty is assigned to cover the disagreement between data and simulation in the distribution of the momentum balance in the transverse plane between the soft and hard terms in $Z \rightarrow \mu\mu$ events. The transverse momentum of the track soft term is decomposed along the hard term in the perpendicular and longitudinal directions. The parallel component is sensitive to scale and resolution differences between data and simulation because the soft term should balance the hard term of the transverse momentum in the $Z \to \mu\mu$ events. The perpendicular component is only sensitive to differences in resolution. [28] The uncertainties on the track soft term combine to form the largest uncertainty in many η_μ bins in this analysis.

5.4.5 Pile-up correction

As described in Sec. 5.3.1 a correction is applied to Monte Carlo such that the distribution of μ (average number of interactions per bunch crossing) better reflects that seen in data. The uncertainty on the correction is simply obtained by the difference of turning the correction on and off.

5.4.6 Correction of the z position of primary vertex

As described in Sec. 5.3.2 a correction is applied to Monte Carlo such that the distribution of the z position of the primary vertex better reflects that seen in data.

The uncertainty on the correction is obtained by the difference of turning the correction on and off.

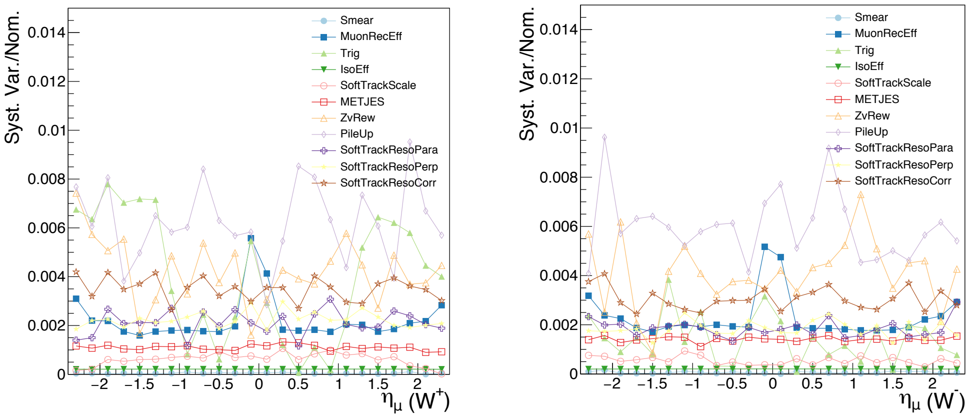

(a) $W^+ \to \mu^+\nu$

(b) $W^- \to \mu^-\bar{\nu}$

Figure 5.11: The ratio of the various systematic variations over the nominal values as a function of η_μ for the $W^+ \to \mu^+\nu$ and $W^- \to \mu^-\bar{\nu}$ decay channels. The muon momentum scale and resolution uncertainty is labelled as “Smear” in the plots.

Systematic Type	W^+ Variation(%)	W^- Variation(%)
Muon momentum scale Down	0.000	-0.001
Muon momentum scale Up	-0.002	0.004
Muon Rec Eff Down	0.215	0.223
Muon Rec Eff Up	-0.215	-0.223
Muon Trig Eff Down	-0.410	-0.114
Muon Trig Eff Up	0.396	0.108
Muon Iso Eff Down	0.021	0.020
Muon Iso Eff Up	-0.021	-0.020
Z vtx Rew Off	-0.320	-0.328
PileUp Off	0.628	0.593
MET JES Up	0.103	0.129
MET JES Down	-0.116	-0.153
Soft Trk Scale Down	-0.057	-0.057
Soft Trk Scale Up	0.061	0.052
Soft Trk Reso Para	0.211	0.185
Soft Trk Reso Perp	0.223	0.182
Soft Trk Reso Corr	0.352	0.304
Total systematics	0.969	0.839

Table 5.7: The contributions from each systematic uncertainty source on the W+ and W- inclusive cross section. The total systematic for $W^+ \to \mu^+\nu$ is 0.969% and for $W^- \to \mu^-\bar{\nu}$ is 0.839%. Muon trigger efficiency (Muon Trig Eff) is the dominate uncertainty from muon. Muon momentum scale is the sum of the muon momentum scale and resolution.

5.4.7 Multi-jet background

Three kinematic distributions m_{T}, $E_{\mathrm{T}}^{\mathrm{miss}}$ and $p_{\mathrm{T}}^{\mu}/m_{\mathrm{T}}$ are used to normalize the multi-jet background with respect to data, which is extracted from muon anti-isolation requirements. To test also different background compositions (events coming from different sources) that form the multi-jet background distributions, two fitting regions were used:

- relaxed m_{T} and $E_{\mathrm{T}}^{\mathrm{miss}}$ cuts
- relaxed m_{T} and $E_{\mathrm{T}}^{\mathrm{miss}}$ cuts but with a $p_{T(W)} < 30$ GeV cut applied

The correlation of m_{T}, $E_{\mathrm{T}}^{\mathrm{miss}}$ and $p_{\mathrm{T}}^{\mu}/m_{\mathrm{T}}$ variables v.s. muon anti-isolation requirement was taken into account by moving the multi-jet control region cuts and extrapolating the results to the signal region. This leads to the fact that these six multi-jet estimates (three variables times two fitting regions) approximately. The remaining difference between these six results is taken as a systematic on the method.

5.4.8 Summary of systematic uncertainties

A summary of the systematic uncertainties from the measurement of the W boson inclusive cross section is presented in Tab. 5.7. The single dominant uncertainty is the trigger efficiency which is around 4%. The second most dominant uncertainty comes from the $E_{\mathrm{T}}^{\mathrm{miss}}$ soft term. As the $E_{\mathrm{T}}^{\mathrm{miss}}$ is constructed from the jets, the uncertainty propagated from jets to the $E_{\mathrm{T}}^{\mathrm{miss}}$ also provides a sizeable contribution to the total uncertainty. The combination of all the uncertainties from the $E_{\mathrm{T}}^{\mathrm{miss}}$ is larger than the uncertainty of the trigger efficiency.

The total systematic uncertainty on the $W^{+} \rightarrow \mu^{+}\nu$ fiducial cross section is 0.969% and on the $W^{-} \rightarrow \mu^{-}\bar{\nu}$ fiducial cross section is 0.839%. Most of the systematics uncertainties are constant as a function of muon η_{μ} .

	$W^+ \to \mu^+\nu$	$W^- \to \mu^-\bar{\nu}$
	value ± stat ± syst ± lumi	
Signal	44553017 ± 7007 ± 457028 ± 932936	30259816 ± 5851 ± 296950 ± 650464
C_w	0.7027 ± 0.0068	0.6951 ± 0.0058
A_w	0.4471 ± 0.0080	0.4427 ± 0.0067
σ_{tot} [pb]	7133.51 ± 1.12 ± 73.17 ± 149.37	4946.56 ± 0.96 ± 48.54 ± 106.33
σ_{fid} [pb]	3189.55 ± 0.50 ± 32.72 ± 66.78	2189.85 ± 0.42 ± 21.48 ± 47.07

Table 5.8: The fiducial and total production cross sections for $W^+ \to \mu^+\nu$ and $W^- \to \mu^-\bar{\nu}$.

5.5 Fiducial Cross Section

The measurement of $W^+ \to \mu^+\nu$ and $W^- \to \mu^-\bar{\nu}$ fiducial production cross sections is based on 51670285 $W^+ \to \mu^+\nu$ and 35960143 $W^- \to \mu^-\bar{\nu}$ candidates which were produced in $\sqrt{s} = 8$ TeV proton-proton collisions at the LHC and corresponds to a total integrated luminosity of approximately 20.28 fb^{-1}.

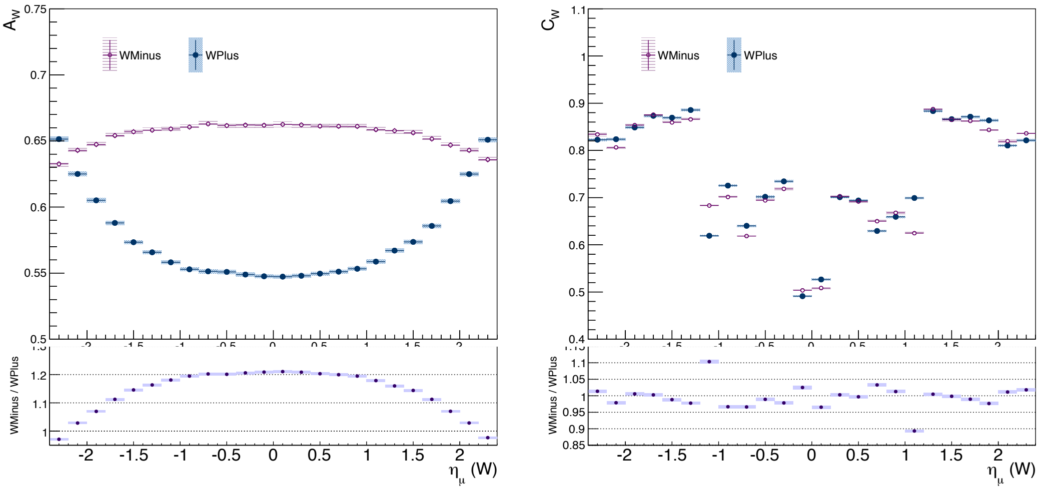

(a) Acceptance

(b) Correction Factor

Figure 5.12: The fiducial phase space acceptance (A_w) and the correction factor as a function of the muon η_μ for $W^+ \to \mu^+\nu$ and $W^- \to \mu^-\bar{\nu}$.

All the elements necessary to calculate the cross section defined in Eq. 5.4 are listed in Tab. 5.8. The number of signal events in the table are the number of the observed candidate events with the number of expected background events subtracted. The correction factor (C_w) is estimated using

PowhegPythia W signal samples with the fiducial phase space described at the beginning of the chapter.

The advantage of measuring the fiducial cross section is that it has smaller theoretical uncertainties than the total cross section, as the theoretical uncertainties primarily impact the acceptance (A_w). The uncertainty of the acceptance in Tab. 5.8 is estimated by the difference between the Sherpa and PowhegPythia predictions.

The ratio of the fiducial production cross section, $\sigma_{\text{fid}^{W+}}/\sigma_{\text{fid}^{W-}}$ is 1.46 which could provide a good constraint of PDF uncertainties. [86]. For the ratio of $\sigma_{\text{fid}^{W+}}/\sigma_{\text{fid}^{W-}}$, most of the experimental uncertainties cancel and the accuracy of the experimental result is comparable to the PDF uncertainties.

The fiducial production cross section, differential in η_μ , is shown in Fig. 5.13. The bin-by-bin differential fiducial cross section is derived using the bin-by-bin correction factors shown in Fig. 5.12. The production cross section of $W^- \to \mu^-\bar{\nu}$ is from around 55% to 80% of the $W^+ \to \mu^+\nu$ cross section, depending on the muon η_μ bin. More W^+ bosons are observed in higher rapidity region than W^- as expected from theory. A non-zero charge asymmetry is observed for the production rate of W^+ and W^-. The charge asymmetry studies based on the fiducial cross sections follows in Sec. 5.7.

5.6 Total Cross Section

The method to calculate the inclusive total production cross section is similar to the way used to calculate the fiducial cross section, the only difference is to divide by the acceptance described in Eq. 5.1.

The ratio of the total production cross section, $\sigma_{\text{tot}^{W+}}/\sigma_{\text{tot}^{W-}}$ is 1.44.

The total production cross section, differential in η_μ , is shown in Fig. 5.14. The bin-by-bin correction factors (C_w^i) and acceptance factors (A_w^i) which are needed to derive the differential total cross section are shown in Fig. 5.12. The ratio plot under the acceptance distribution shows that the acceptance of $W^+ \to \mu^+\nu$ in the central η_μ range is around 20% higher than $W^- \to \mu^-\bar{\nu}$. The correction factors are similar between $W^+ \to \mu^+\nu$ and $W^- \to \mu^-\bar{\nu}$ over all η_μ bins. The correction factors at η_μ bin ± 1.1 has around 10% difference

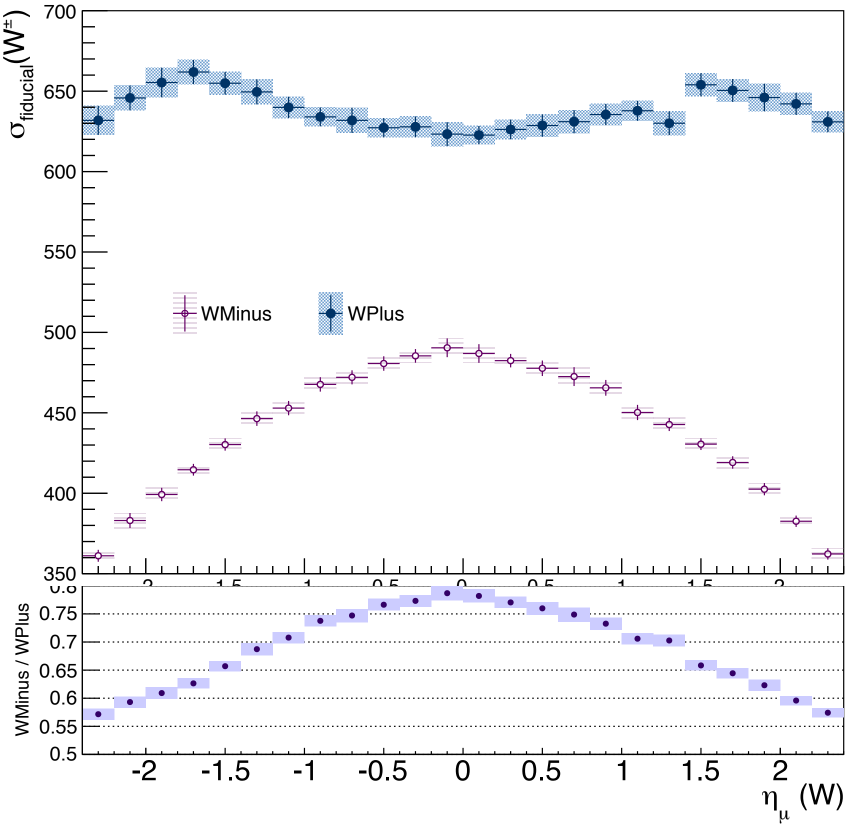

(a) $W \to \mu\nu$ Fiducial Cross Section

Figure 5.13: The fiducial production cross section (in units of pb) as a function of the muon η_{μ} for $W^{+} \to \mu^{+}\nu$ and $W^{-} \to \mu^{-}\bar{\nu}$.

between $W^{+} \to \mu^{+}\nu$ and $W^{-} \to \mu^{-}\bar{\nu}$, the exact reason is due to the lack of the trigger scale factors in bins of muon p_{T} .

Both the total and fiducial production cross sections were measured at the Born level which means correcting the decay lepton not only for detector effects but also for all QED final state radiation. All the measured cross sections are shown with their total uncertainty, which is calculated as the quadratic sum of statistical uncertainties and all systematic uncertainties. A luminosity uncertainty of 2.8% is not included in any of the plots.

5.7 Measurement of Muon Charge Asymmetry from W Boson

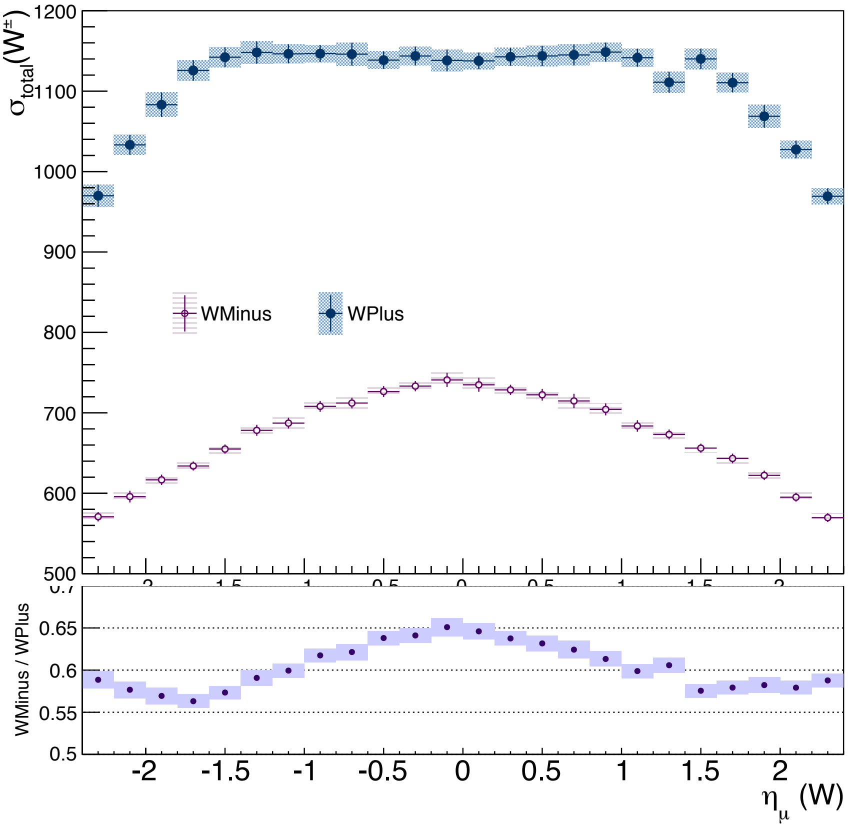

(a) $W \to \mu\nu$ Total Cross Section

Figure 5.14: The total production cross section (in units of pb) as a function of muon η_μ for $W^+ \to \mu^+\nu$ and $W^- \to \mu^-\bar{\nu}$.

5.7.1 Results and Comparison to Theory

The total muon chage asymmetry in the fiducial phase space is:

- $\mathrm{A}_\mu = 0.18263 \pm 0.00147(\mathrm{syst.}) \pm 0.00021(\mathrm{stat.})$

The total systematic uncertainty is 0.8% of the central value. A breakdown of the contribution of the individual uncertainty sources to the total systematic is listed in Tab. 5.9.

Most of the systematic uncertainties are considered as correlated between plus and minus charged W bosons, except multi-jet background, luminosity and statistical uncertainties which are considered as un-correlated.

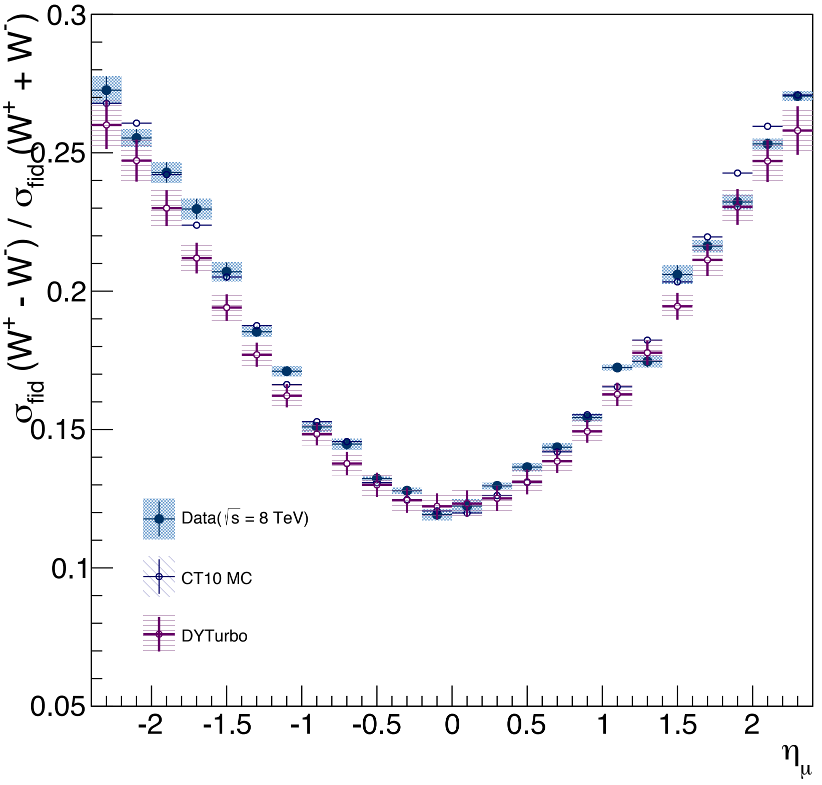

(a)

Figure 5.15: The muon charge asymmetry distribution as a function of η_μ in steps of 0.2. The dark blue dots are data with statistical and systematic uncertainty in blue bands. Data is compared to the theoretical prediction from DYTurbo (red cross) and CT10 (blue cross). The DYTurbo prediction is shown with theoretical uncertainties (pink band), but CT10 is only shown with its statistical uncertainty (light blue band).

The measured differential muon charge asymmetry in steps of 0.2 in η_μ from -2.4 to 2.4 is shown in Fig. 5.15. Each systematic variation of the fiducial cross section is input for the corresponding muon charge asymmetry calculation and is propagated to the muon charge asymmetry variables differential in η_μ using the offset method. The quadratic sum of all systematic variation differences between the nominal value of the muon charge asymmetry is the total systematic uncertainty. The quadratic sum of statistical and systematic uncertainties is the total uncertainty for each η_μ bin. The luminosity uncertainty is not included in the plot, but is anyway negligible as it is fully correlated between W^- and W^- cross section measurements.

Systematic Type	δA$^{\mu}$	1- δA$^{\mu}$/Nominal (%)
Muon Iso Eff Down	0.00000	0.002
Muon Iso Eff Up	-0.00000	-0.002
MET JES Down	0.00018	0.096
MET JES Up	-0.00013	-0.068
PileUp Off	0.00017	0.095
Muon Rec Eff Down	-0.00004	-0.020
Muon Rec Eff Up	0.00004	0.020
Muon momentum scale Down	0.00001	0.003
Muon momentum scale Smear Up	-0.00003	-0.016
Soft Trk Reso Corr	0.00023	0.126
Soft Trk Reso Para	0.00012	0.066
Soft Trk Reso Perp	0.00020	0.107
Soft Trk Scale Down	0.00000	0.000
Soft Trk Scale Up	0.00004	0.022
Muon Trig Eff Down	-0.00143	-0.774
Muon Trig Eff Up	0.00139	0.756
Z vtx Rew Off	0.00004	0.020
Total systematics	0.00147	0.796

Table 5.9: A break down of the sources of uncertainty considered on the muon charge asymmetry. The largest uncertainties come from the $E_{\mathrm{T}}^{\mathrm{miss}}$ soft term and the trigger scale factors

The theoretical prediction using Sherpa with the default PDF CT10 is shown for comparison. Another theoretical prediction generated using DYTurbo [43] is shown together in the Fig. 5.15 for another comparison. DYTurbo is a NNLO (next-to-next-to-leading order) Monte Carlo generator including resummation at NNLL (next-to-next-to-leading-logarithmic order). [65] The predictions are calculated using the same fiducial phase space as the fiducial production cross section analysis. Only the statistical uncertainty is included on the Sherpa+CT10 prediction. The uncertainty band on the DYTurbo prediction contains contributions from varying the factorisation and renomalisation scales as well as from the choice of PDF (default is CT14).

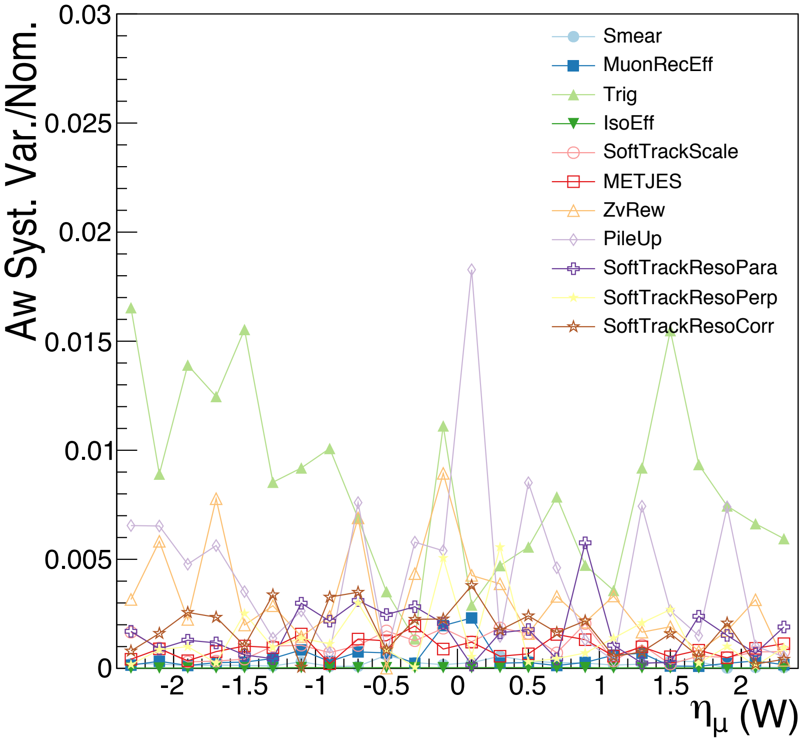

(a)

Figure 5.16: The systematic uncertainty on the muon charge asymmetry distribution as a function of muon η_μ , separated into the major contribution sources.

The data and predictions are in reasonable agreement and follow the same trends. The asymmetry increases by a factor of 2.5 from the central to the forward η_μ bins. The positive η_μ range has a smaller uncertainty on the muon charge asymmetry than the negative η_μ range. This is due to some detector chamber defects during the early data taking periods with the ATLAS detector. As the measurement of the muon charge presented in this thesis is more precise than the theory predictions, the difference between data and prediction is key to improving PDFs and validating Monte Carlo generators.

5.7.2 Comparison with the 7 TeV result

Following the measurement procedure from the previous sections, a measurement is made of the differential charge asymmetry using the same η_μ binning as for the $\sqrt{s}$ = 7 TeV analysis. The correction factors and the fiducial production cross section in bins of η_μ is shown in Figure 5.17. Due to the low statistics for the $\sqrt{s}$ = 7 TeV analysis, a broader η_μ binning was chosen in order to reduce the statistical uncertainty. For the $\sqrt{s}$ = 8 TeV analysis here, the statistics are higher and therefore finer bins are used. The choice of the binning was described in Section 5.3.7.

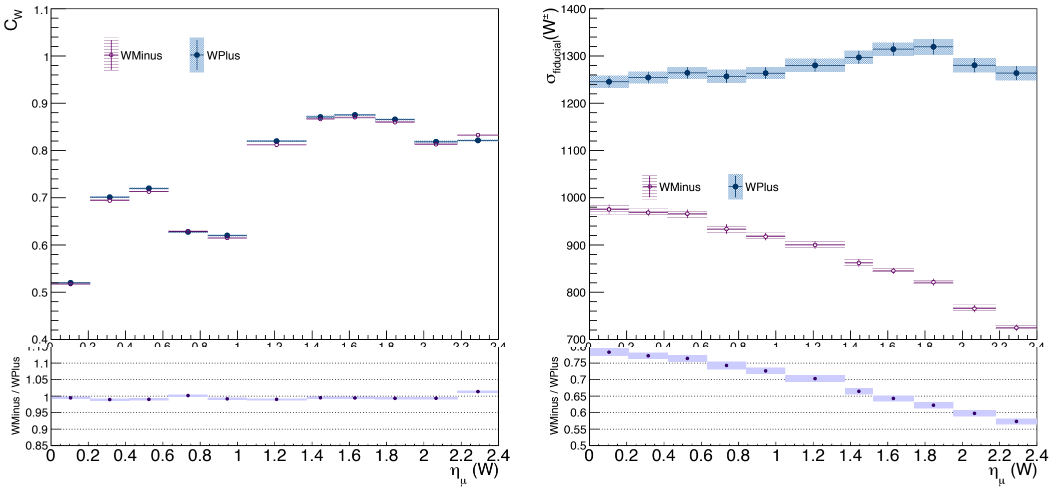

(a) Correction Factor (b) Fiducial Cross Section

Figure 5.17: The correction factor (C_W) and the fiducial cross section using the same binning as the $\sqrt{s} = 7$ TeV analysis.

The muon charge asymmetry for the $\sqrt{s}$ = 7 TeV and $\sqrt{s}$ = 8 TeV analyses (using the 7 TeV η_μ binning) is shown in Figure 5.18. The measured result from $\sqrt{s}$ = 8 TeV is compared to the prediction of Sherpa, using three different PDF sets, CT10, MSTW2008NLO68cl and CT14 NNLO [40]. The default Sherpa sample is produced with the CT10 set and the other two predictions are obtained by a reweighting technique implemented in the package LHAPDF6. [40] Sherpa is used here, rather than PowhegPythia8 as PowhegPythia8 is known to have a bug in its truth level information. The CT10 theoretical prediction is shown only with the statistical uncertainty included. For the MSTW2008 NLO 68cl and CT14 NNLO predictions, the systematic uncertainties are extracted from the $\sqrt{s} = 7$ TeV analysis. The uncertainties for the current analysis are in a good agreement with the theoretical prediction and are comparable to the previous analysis.

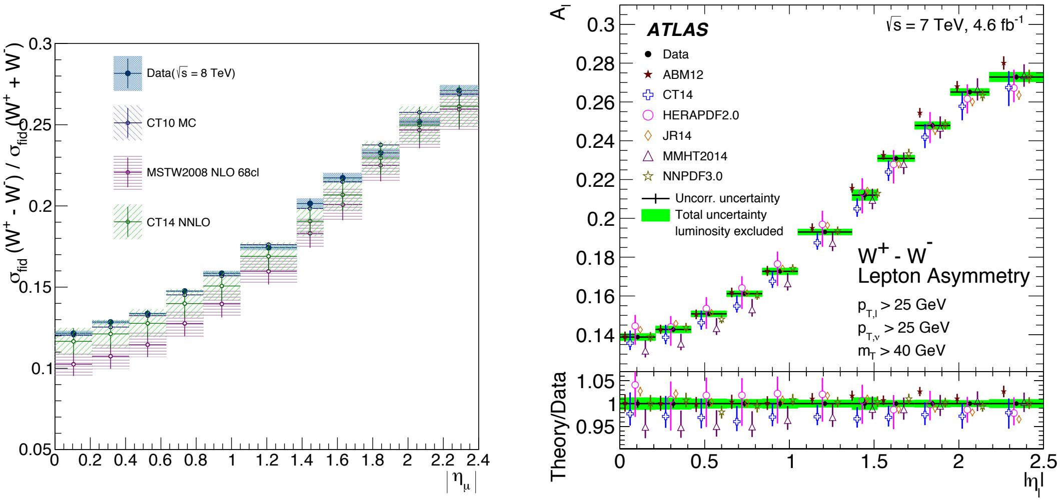

(a) $\sqrt{s} = 8$ TeV (b) $\sqrt{s} = 7$ TeV [78]

Figure 5.18: The muon charge asymmetry of the W boson of the $\sqrt{s} = 7$ TeV and $\sqrt{s} = 8$ TeV analyses presented using the same binning of the absolute values of the muon pseudorapidity. The $\sqrt{s} = 7$ TeV plot shows the combined results of the electron and muon channel.

To directly compare the $\sqrt{s} = 7$ TeV and $\sqrt{s} = 8$ TeV results, Fig.5.19 shows the data and theory prediction of DYTurbo using the same absolute muon η binning. In order to compare the similar uncertainties for both $\sqrt{s} = 7$ TeV and $\sqrt{s} = 8$ TeV analyses, only the uncorrelated and statistical uncertainties from $\sqrt{s} = 7$ TeV analysis are included. The double ratio of the theory over data between $\sqrt{s} = 7$ TeV and $\sqrt{s} = 8$ TeV shows that there is agreement between the two centre of mass energy results to within 4% and has a χ^2/ndf of around 1.74. This corresponds to a probability of 5%, i.e. indicates a reasonable agreement between the two measurements.

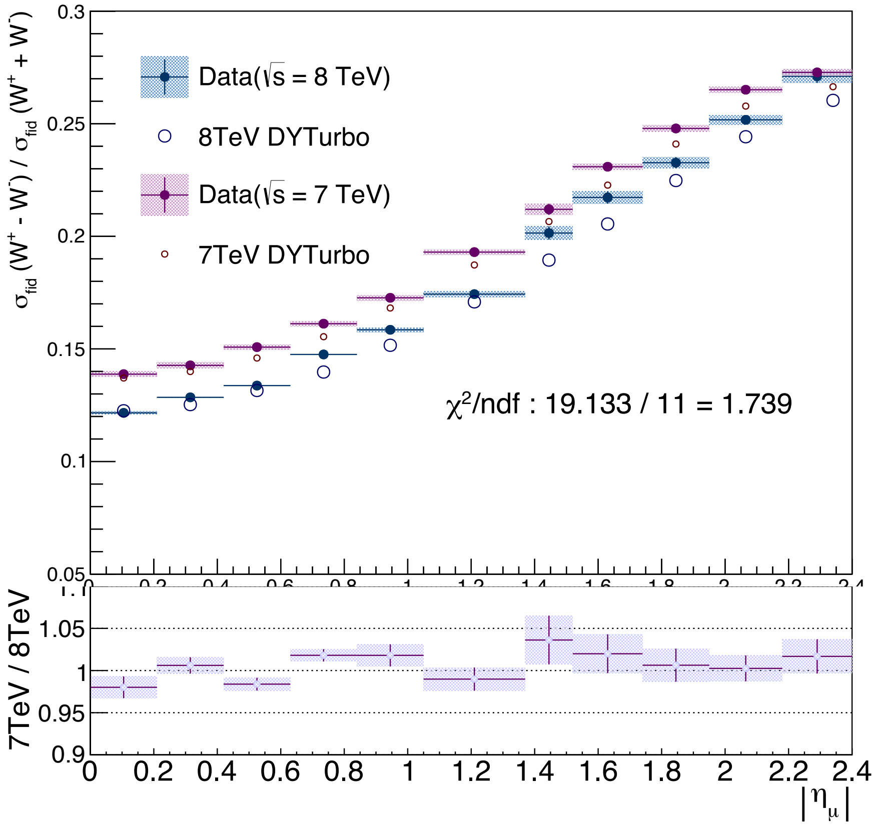

(a)

Figure 5.19: A comparison of the results from the $\sqrt{s}$ = 7 TeV and $\sqrt{s}$ = 8 TeV data measurements and the DYTurbo theory prediction. The bottom plot shows the double ratio of the theory over data between $\sqrt{s}$ = 7 TeV and $\sqrt{s}$ = 8 TeV.

6

Developments and Tests of a Prototype Detector towards the ATLAS Muon Spectrometer Upgrade Project

The upgrade of the LHC (High Luminosity LHC) scheduled to be completed in 2023 will increase its instantaneous luminosity to ten times more than the current luminosity. Correspondingly, the particle flux rate will increase 5 times more for the ATLAS muon detector. The small wheel directly behind the toroid magnets will suffer from higher occupancy and its performance will be degraded. The higher pile-up condition make the upgrade of the ATLAS muon spectrometer necessary. This chapter details the construction and testing of two prototype detectors using micromegas technology, which were then tested in order to optimize the design of the detector and to quantify its performance.

The installation of an upgrade of the ATLAS muon detector is expected in 2018. The high luminosity run of the LHC can further improve the precision of the W boson charge asymmetry measurement. The expected interaction rate at the high luminosity LHC will cause many more W boson events to be produced. Higher statistics of W boson production will allow analyses to filter for W boson events without any hadronic activity in order to get clearer signals. The upgrade of the end-cap region of the ATLAS detector allows the analyses to extend more into the forward region and thus reduce significantly polarization and PDF uncertainties.

6.1 The Upgrade of the ATLAS Muon Spectrometer

Several phases of the upgrade of the LHC are scheduled in order to extend the physics program. The accelerator luminosity is expected to reach $(2 -$

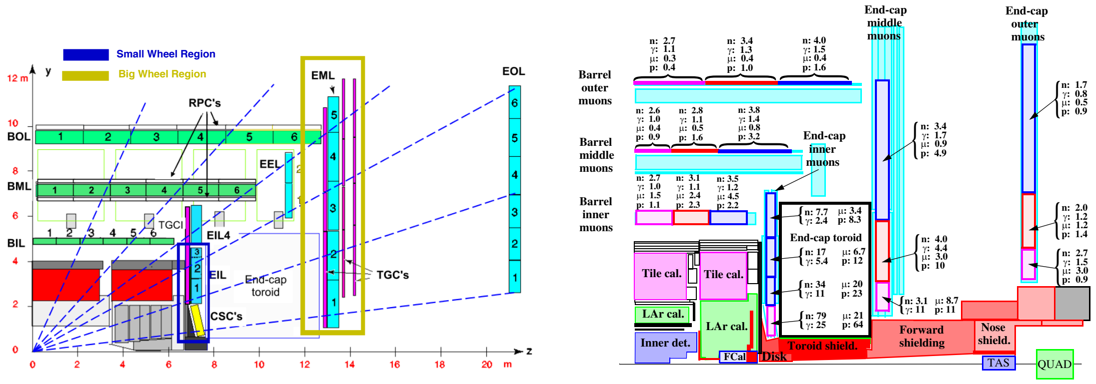

(a) Small Wheel Region (b) Particle Flux

Figure 6.1: The z-y view of a quarter of the ATLAS detector to show the location of the current small wheel and the simulated particles flux with high luminosity conditions. Particle fluxes in the various muon spectrometer stations at high luminosity (10^{34} $\mathrm{cm}^{-2}\mathrm{s}^{-1}$) are as predicted by GCALOR. [99] The neutron and photon fluxes are in units of kHz/cm^2 and the muon and proton fluxes in Hz/cm^2 [85]

3×10^{34} $\mathrm{cm}^{-2}\mathrm{s}^{-1}$) and allow ATLAS to collect approximately 100 fb^{-1} per year after the second long shutdown (LS2) in 2018. The particle flux in the muon spectrometer is simulated in the high luminosity conditions shown in Fig. 6.1(b). The corresponding upgrade of the ATLAS muon spectrometer focuses on the end-cap region with a η coverage of $1.0 < |\eta| < 2.7$ as the following two issues would otherwise limit the ATLAS performance:

- The high occupancy in the forward muon chambers with the upgrade of the high luminosity LHC will degrade the performance of the small wheel especially for the spatial resolution and its efficiency based on the observation of the tracking performance from an extrapolation of the 2012 run data.

- From an analysis of the 2012 data, approximately 90% of events selected by a muon trigger are fake in the end-cap region. [67] The fake triggering is due to the low energy particles, mainly protons, which are generated in the material located in the Small Wheel and are registered in the end-cap trigger chambers at a similar angle to the real high p_T muons. [67]

Therefore the New Small Wheel (NSW) has been proposed to replace the present muon Small Wheels with pseudorapidity coverage $1.3 < |\eta| < 2.7$

(see Fig. 6.1(a)). This would have a set of precision tracking and trigger detectors which is capable to work at high rate with accordingly real-time spatial and time resolution.

The New Small Wheel project is composed of a high rate capable Micromegas tracking detector and Thin Gap Chamber (TGC) triggering detectors. Two prototype Micromegas detectors (MICRO Mesh GAseous Structures Detector Small Wheel, MMSW) were constructed to study the performance and its capability for the NSW upgrade.

6.2 MICRO Mesh GAseous Structures Detector

MICRO Mesh GAseous Structures (Micromegas) are gaseous parallel plate detectors consisting of two asymmetric electric field regions, the drift and amplification region, separated by a thin metallic mesh. [73]

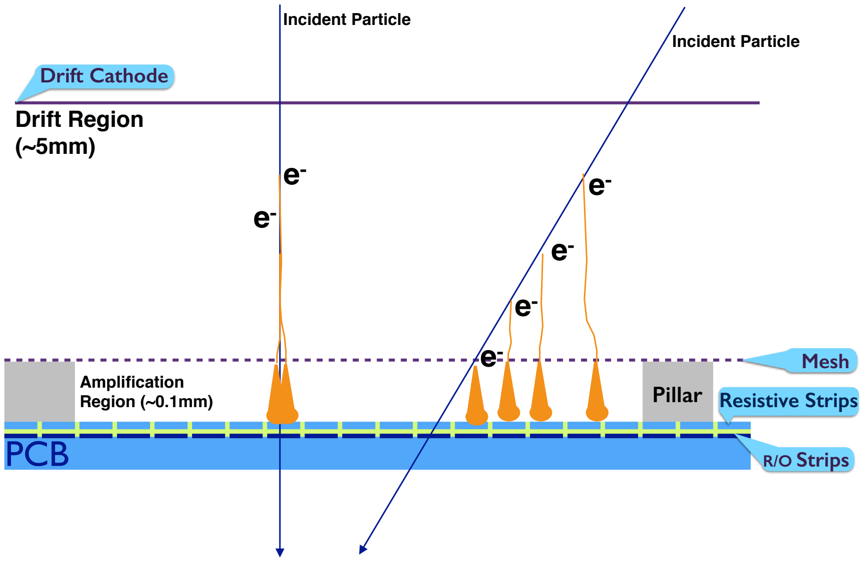

(a)

Figure 6.2: The plot shows the principle function of the gas detector when a charged particle passes through the drift region and amplification region of the detector.

Fig. 6.2 shows the typical layout of a Micromegas detector. A planar drift electrode and a readout electrode are separated by a gap of a few mm. While the drift electrode is covered uniformly with a conducting layer, e.g. copper, the readout electrode is usually made of a PCB board with uniform structure of conductors, separated by isolating material. The strip width and the distance between them is variable and depends on the final application.

The gap between the two electrodes is filled with an ionization gas, e.g. a 93:7 mixture of Argon and CO2. A metal mesh is placed at 50-100 μm above the readout electrode, defining two regions on the detector. The region between the drift electrode and the mesh is called the drift region.

In order to create the drift and amplification environment, two external voltages are applied to the drift cathode and the resistive strips. The drift and amplification regions are separated by a metal mesh. A typical electric field in the drift region is $\approx$ 600 V/cm. A significant higher electric field strength of $\approx$ 50 kV/cm is reached in the amplification region, defined as the region between the mesh and the readout-electrodes.

This high electric field in the amplification region might lead to sparking, which leads to dead-time and could potentially damage the detector and the subsequent readout-system. Therefore, the readout strips are covered with a resistive protection layer [8] that consists of a thin insulator with a resistive paste. The resistive protection layer has a resistance in the order of $\approx$ MΩ/cm and usually matches the geometry of the readout electrodes, in order to minimize a charge spread over the several readout strips.

A charged particle that enters the drift volume ionizes gas atoms and generates ionization electrons. These electrons drift with a typical velocity of $\approx$ 5 cm/μs along the electric field to the mesh. The mesh appears transparent to the drift electrons due to the larger electric field strengths in the subsequent amplification region. Once the drift electrons reach the high electric field strength in the amplification region, they get accelerated sufficiently fast to cause a cascade of secondary electrons (avalanche) leading to an amplification factor of $\approx$ 104 in 1 ns. These secondary electrons reach the resistive layer and induce a signal in the readout electrodes, by capacitively coupling to resistive strips. A detailed introduction to the signal formation in Micromegas detectors can be found in [53]. [73]

6.3 Design Steps of the MMSW Detector

In the detector layout adopted by the ATLAS NSW upgrade, a layer of resistive strips is cladded by spattering on top of the readout strips for spark tolerance. The construction and first performance studies of two $0.5\,\mathrm{m}^2$ Micromegas quadruplets is performed. These prototypes serve the purpose of evaluating the detector design and construction towards the production of the Micromegas detectors that will be installed in the ATLAS Small Wheels.

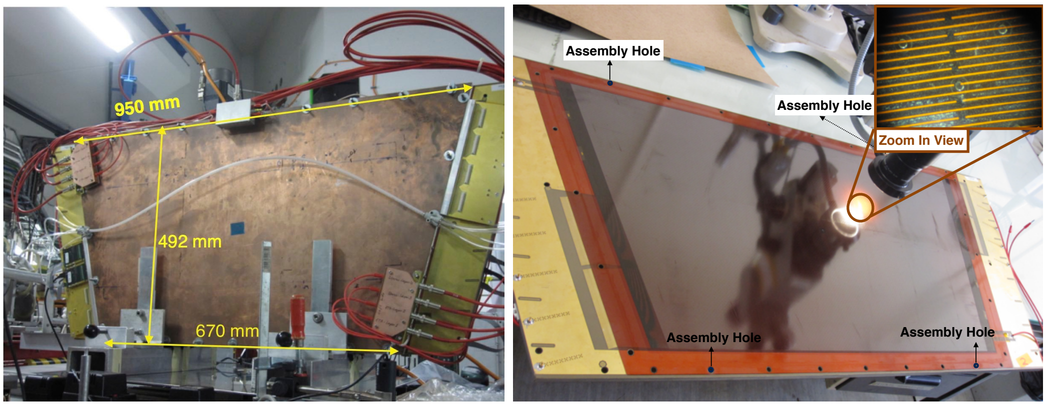

(a) The prototype picture of MMSW

(b) View of Readout Panel

Figure 6.3: The prototype picture of the MMSW is shown on the left with its detailed dimensions. The readout panel is shown on the right and a zoom in of the resistive strips is shown in the top right corner.

A schematic drawing of the prototypes is shown in Fig. 6.4. Each quadruplet consists of three drift and two readout panels with a trapezoidal shape. The readout panels are 20 cm longer than the drift panels, in the upper and lower base, in order to host the readout electronics. The readout panels are formed by two back-to-back FR4 printed circuit boards (PCB) with aluminum honeycomb in between and surrounded by an aluminum profile as a supporting structure. Each readout PCB hosts 1024 readout strips with a width of 300 μm and a pitch of 415 μm. Two readout layers have strips parallel to the trapezoidal base for the reconstruction of the precision coordinate, while the other two have strips inclined by a $\pm 1.5^o$ with respect to other layers for the reconstruction of the precision and second coordinate [93]. This strip pattern allows for a precise measurement of the spatial resolution.

The drift panels have a similar structure to the readout panels but instead of the readout strips they are clad with a copper layer to serve as a cathode for the drift region.

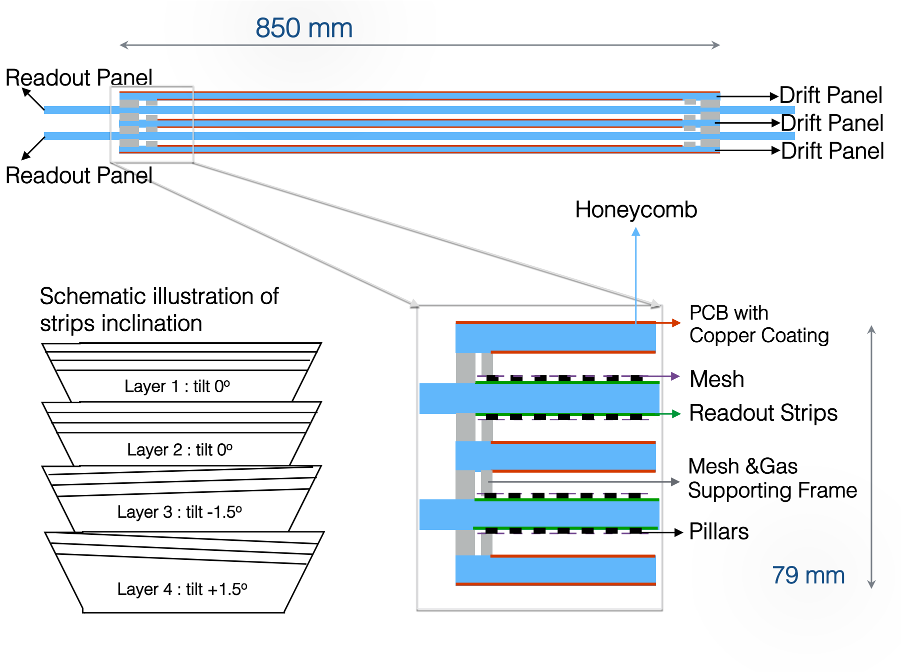

(a)

Figure 6.4: The layout design of the MMSW detector is summarized on the plot. The upper plot is the bottom view of the chamber, two readout panels are between three drift panels and are 20 cm longer to hold the electronics. The bottom left plot indicates the geometry of the readout strips with parallel strips in the first two layers and a tilt of ± 1.5 degrees for the third and fourth layers. The detailed cut-away view is shown in the bottom right plot.

6.3.1 The Dimensions of the MMSW

The layout of the New Small Wheel is designed and optimized to have one precise dimension which is taken directly from the information of the strips ID (η strips, from the first and the second layer of the prototype detector) and another dimension which would be reconstructed by the tilted strips (Stereo strips, from the third and fourth layers). The tilted angle of the third and fourth layers was optimized by testing the asymmetric and symmetric cases. A tilt of $\pm 1.5^o$ symmetrically was chosen.[63]

The precision dimension is defined as the x-dimension and the other dimension as the y-dimension. The strip ID for the i-layer is defined as η_i, and the

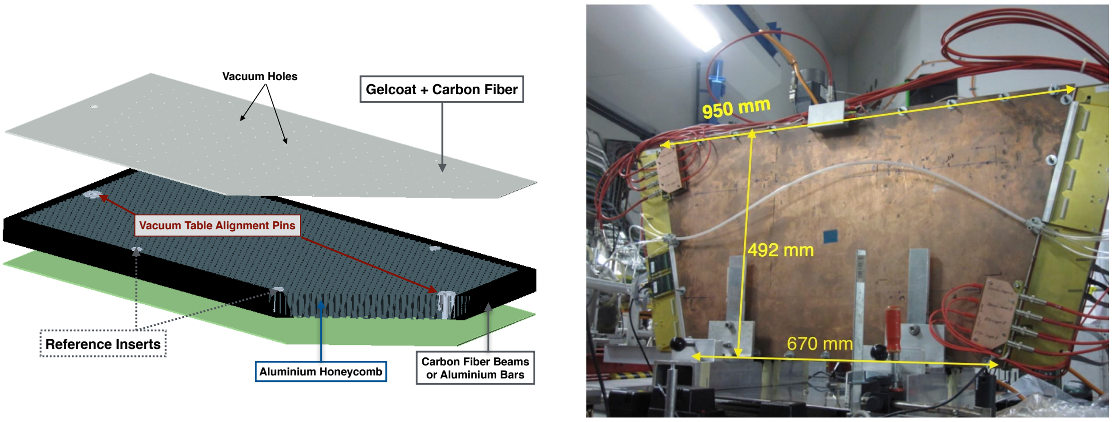

Figure 6.5: Schematic view of the vacuum table (left) and a photo of the one final assembled detector quadruplet equipped with electronics. (right)

tilted strip angles for the 3rd and 4th layers are labelled $+\theta$ and -θ. The reconstructed x- and y- coordinates are as following:

$$\begin{aligned} x_{3,4} &= \frac{\eta_3 + \eta_4}{2\ \cos\theta} \\ y_{3,4} &= \frac{\eta_3 - \eta_4}{2\ \sin\theta} \end{aligned} \tag{6.1}$$

The design of the layout with two stereo layers with strips symmetrically tilted at an angle provides one extra piece of information for the precision layer which can make in-chamber tracking possible and also provide information for the other dimension which has less precise requirements.

6.4 Detector Construction

High planarity of the drift and the readout panels is needed in order to reach the required detector performance. Any non-parallel panels will make the reconstruction of the particle track imprecise and worsen the spatial resolution. For this reason, two vacuum tables were built to construct the panels. The drift and the readout panels were glued in a sandwich structure with aluminium honeycomb in-between as a supporting structure and surrounded by an aluminium profile. Details of the construction are described in [72], [64], hence a brief summary is given in the following.

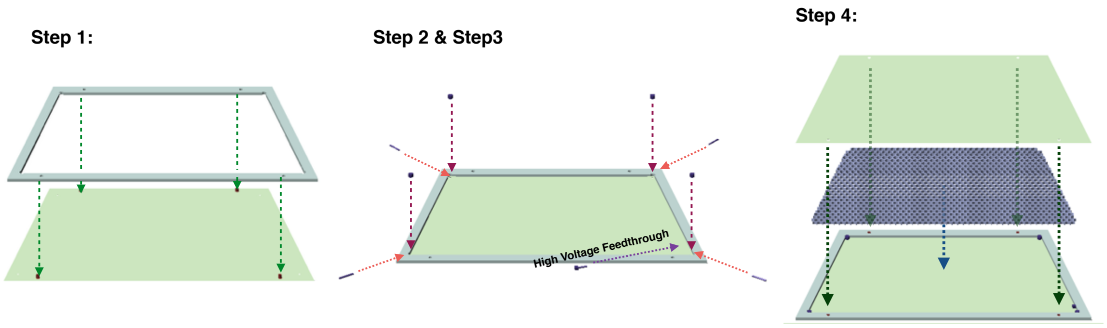

Figure 6.6: Schematic illustration of the drift panel construction.

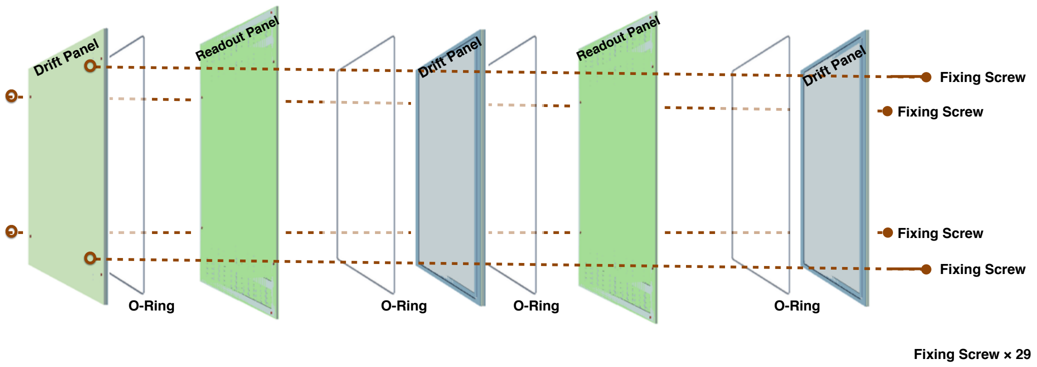

Figure 6.7: Schematic illustration of the panel assembly procedure. The assembly of the two detector quadruplet was done vertically.

The vacuum tables are made of 60 mm perforated aluminium honeycomb, to provide the required stiffness of the table-structure and surrounded by two 3 mm thick skins of carbon fibre (Fig. 6.5 (left)). One of the table surfaces is coated by a 0.5 mm thick gel-coat layer. The carbon fibre skin together with the gel-coat layer have been prepared and cured on a high-precision granite table transferring the granite table flatness to the vacuum table. The vacuum holes on the tables are drilled with a diameter of 1 mm with a regular pattern within the same trapezoidal shape of drift panels.

The panel construction is illustrated in Fig. 6.6 and described in the following. It is to a large extent identical for the drift and readout panels. In a first step, the aluminium frame is glued to the FR4 skin of the panel. Before the aluminium honeycomb is glued in the space surrounded by the frame, gas connectors and one high voltage feedthrough are attached to the frame of the drift PCB (not for the readout PCB). Then the second PCB is glued on the top of the frame and honeycomb structure to close the drift panel. The mesh frame and the gas gap frame together with two gas tubes are also glued onto the top of the drift panels. In a last step, a uniformly stretched mesh is assembled on the drift panel structure. The assembly sequence of the final detector quadruplet is illustrated in Fig. 6.7. The gas tightness is ensured by four O-rings, which are inserted between the drift and readout panels around the mesh frames. The distance between the panels is defined by special gas gap spacers, consisting of four 5 mm thick precision-machined bars with assembly holes. One final assembled detector quadruplet is shown in the right of Fig. 6.5.

6.4.1 Design Improvements

During the construction of MMSW-1, several difficulties in the construction had been encountered, leading to an improved design for the construction of MMSW-2.

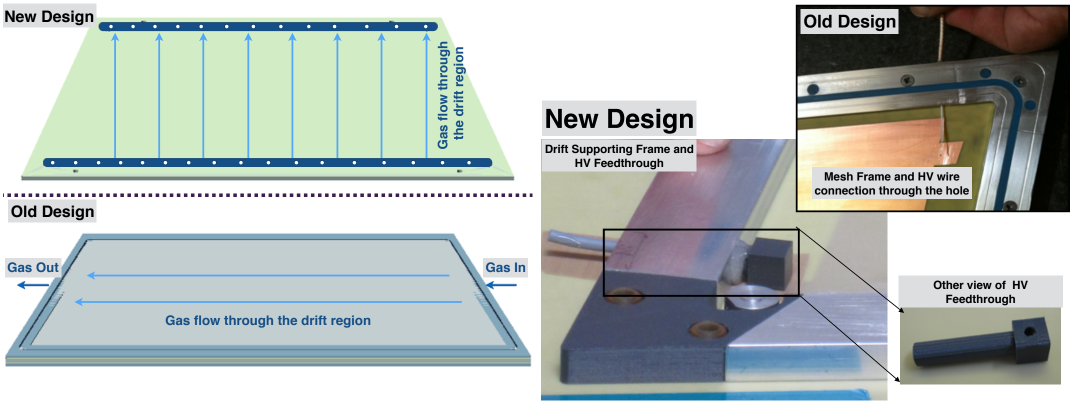

(a) Gas Pipe Design (b) High Voltage Feed Through Routing

Figure 6.8: The improved design from the first prototype to the latest prototype. The old design of the gas system had only two gas inlets and outlets which is improved by two parallel gas pipes with holes in between. And the new design of high voltage feedthrough also makes the routing better protected and stronger.

The first vacuum tables were constructed with aluminum plates which may be deformed by small temperature changes in the environment. However if the temperature in the environment is kept constant the aluminium based vacuum can still be operated stably. An alternative choice to use are vacuum tables constructed with carbon fibre. These are sensitive to the environment humidity but are less sensitive to temperature changes and as such are the preferred choice in the PRISMA laboratory where the humidity is stable but the temperature is unstable.

The gas is injected through the drift panel. The first version of the gas distribution system had only one inlet and one outlet which took longer to let the gas uniformly fill the gas chamber. An updated design foresees that the gas feed-throughs in the four corners of the drift panel frame have been produced by 3D printing and are part of the panel frame.

Before gluing the mesh, the gas distribution pipes are mounted. They are held in place by junction pieces that are glued at both sides to the feed-throughs and the gas pipes which have a better gas distribution within a reasonable time frame, as shown in Fig. 6.8(a).

The drift electrode is connected to the HV by an insulated wire, soldered to the Cu layer outside the active area. The wire is routed through a hole in the PCB into the panel and through another opening in the panel frame to the outside and sealed with Araldite, see Fig. 6.8(b).

6.5 Readout and Signal Characteristics

The MMSW detectors have been read out through the RD51 Scalable Readout System (SRS) [79, 80]. Since the final electronics for the NSW micromegas are not yet available, APV25 (Analogue Pipeline Voltage chips with $0.25\,\mu$m CMOS technology) [74] hybrid cards are used instead. The APV hybrid cards are mounted on intermediate (mezzanine) boards that are connected to the readout panels through Zebra connectors[1]. Each mezzanine hosts four APV25 boards and covers 512 strips.

The APV25 chip has 128 channels and delivers analogue CR-RC shaped signals sampled at 40 MHz. The analogue signals from the APV25 are transmitted via HDMI cables to the SRS ADC card where they are digitised and transmitted to the data acquisition PC. Here, a zero suppression algorithm is applied with a factor of 0.8 of the baseline background to ensure a clearer signal and reduce the data size. Since the APV25 chip had been developed

---

[1] The APV hybrid cards carry 130-pin connectors, not compatible with the Zebra connection scheme chosen for the MMSW.

for the readout of silicon detectors it uses a short integration constant that is not optimised for the micromegas with a longer charge collection time. Another drawback is the limited dynamic range of the chip. The chip is used in a mode that samples the integrated charge over up to 27 time bins of 25 ns. An example of the APV25 output for a single electronics channel, after zero suppression is given in Fig. 6.9. It shows the development of the integrated charge in 25 ns bins. From these data, for each channel, the signal charge and a time stamp are extracted. The signal charge is defined as the maximum of the integrated charge samples. The time stamp is taken as the maximum of the first derivative of the rising edge of the signal (or the half rising time). The signal event registered in the four layers of the detector is shown in Fig. 6.10.

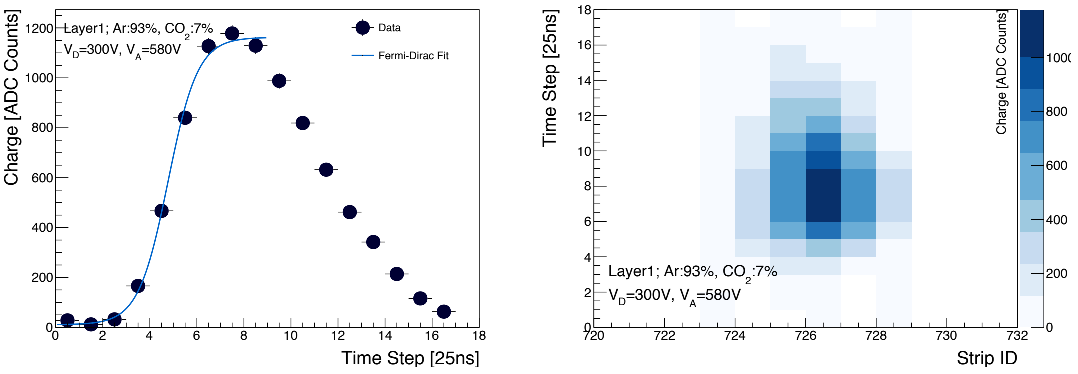

(a) Charge Integration over Time (b) Charge Integration over Time among Strips

Figure 6.9: A typical event readout from the detector. The plot on the left shows the charge integration over 18 time steps for a signal strip. The plot on the right shows the all the strips (strip ID in x-axis) register the integration charge (represented in colour in z-axis) over time (time steps in y-axis).

The basic signal characteristics are shown in Fig. 6.10 (left), the plot from each layer shows the signal shape of a cluster. A cluster is defined as the group of the strips from one event and the charge of each strip is the maximum charge over all time steps. The number of the strips in a cluster is called the cluster size. The sum of maximum charge from the each strip is the cluster charge. The cluster charge shows the behaviour of the energy of the incident particle. Fig. 6.11 show the cluster size, number of clusters per event and cluster charge from the cosmic ray measurement with different amplification voltages.

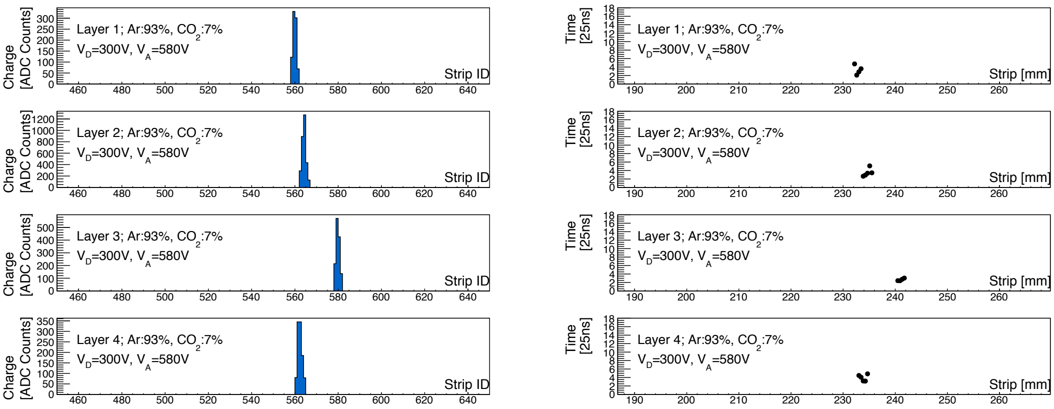

Figure 6.10: A typical event shows the signal over four layers of the detector. The plot on the left shows all strips were hit for one event with the maximum charge over all time steps. The plot on the right shows all strips were hit for one event with the time step which registered the maximum charge.

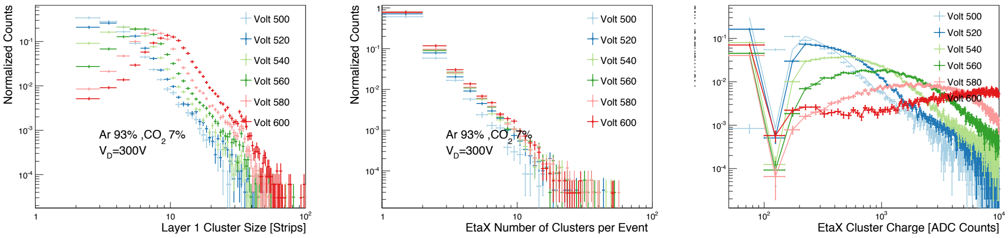

(a) Cluster Size (b) Number of Clusters (c) Cluster Charge

Figure 6.11: The plots shows the cluster size distribution (left), number of clusters per event (middle) and cluster charge (right). The average cluster size increases with higher amplification voltage and up to 10 strips while 600 V is applied. The average number of clusters is one over all the amplification voltages under cosmic ray tests. There is peak in front of the main peak of the cluster charge, which represents the noise of the detector system.

6.6 Cosmic Ray Measurements

The performance of the detector can be tested by cosmic ray measurements. These measurements are used to test the uniformity of the detector as the cosmic rays are incident over the whole detector and can be easily tested everywhere.

The performance studies based on cosmic muons were performed in the ATLAS cosmic ray stand in the RD51 Collaboration [44] laboratory at CERN. Two layers of twelve plastic scintillator slabs with an active area of $2.5 \times 1.1\,\mathrm{m}^2$ in each plane at a distance of 2 m have been used as a coincidence trigger. The MMSW has been operated with a gas mixture of Ar:CO_2 (93:7) at atmospheric pressure, amplification voltages ranging from $V_\mathrm{A} = 500\,\mathrm{V}$ to $V_\mathrm{A} = 600\,\mathrm{V}$, and a fixed drift voltage of $V_\mathrm{D} = -300\,\mathrm{V}$.

6.6.1 Event Selection

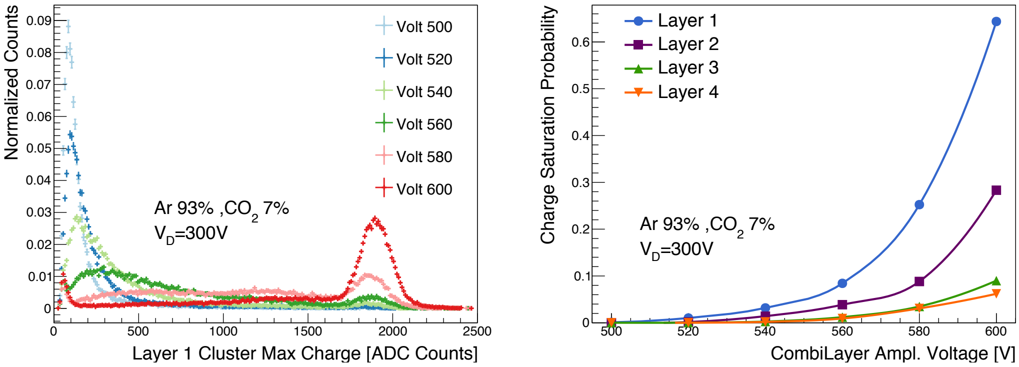

(a) Maximum Charge Plot of Clusters (b) Charge Saturation Probability

Figure 6.12: The left plot shows the distribution of the maximum charge per event with different amplification voltages. The saturation peaks becomes more pronounced with the higher amplification voltages applied. If the saturation behaviour is defined as the maximum charge over 1800 ADC counts, the saturation probability is shown on the right plot. The layers that register incoming particles first contain more saturated charge clusters.

In order to distinguish the signal from the noise, several event selections are applied for the measurement:

- **Cluster size**, a good event should have more than one strip that is hit

- **Number of clusters**, if there are many clusters for one event, for example more than 20 clusters appear at the same time within one layer, it is most likely to be electronic noise. Events such as these are removed.

- **Requirement on cluster charge**, the distribution of the cluster charge has a Landau distribution. The peak in the low cluster charge region is usually noise. Cutting out this peak helps distinguish the signal from the noise. The two peak structures can be seen in Fig. 6.11(c)

The distributions using the selection criteria above are shown in Fig. 6.11. In order to determine the detector efficiency, high quality hits in the reference layer is needed to suppress background. Two selection criteria are introduced here, the tight selection for the reference layers to make sure good events are selected for tracking and the nominal selection for the target layer. If all the reference layers registered good events, the nominal selection in the target layer can determine the tracking of the event.

The nominal selection criteria are:

- the missing strips (without registering any hit) in a cluster are less than or equal to 2 strips

- more than or equal to 2 strips in a cluster

- less than 20 clusters per event

- cluster charge more than 150 ADC counts

The tight selection criteria includes the nominal selection criteria but requires in addition:

- more than or equal to 3 strips in a cluster

- only one good cluster per event

The cutflow of the event selection for the cosmic ray measurement is shown in Fig. 6.13 with two different amplification voltages applied. The selection rates are different for different layers and with different amplification voltages. The events registered in the first layer which is the upper-most layer are more than in the other layers. The number of registered events reduces as the number of layers that the particle passed through increases.

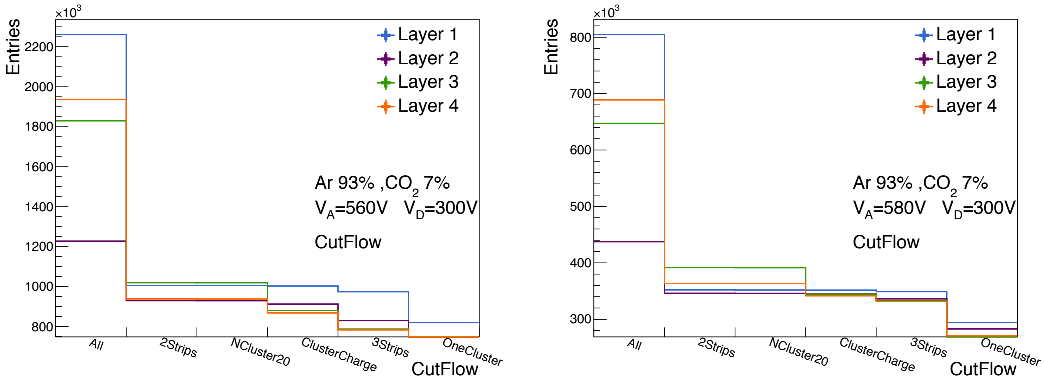

(a) Cut Flow with 560V

(b) Cut Flow with 580V

Figure 6.13: The cut flow with different stages of the event selection for four layers of the detector and two different amplification voltages 560V on the left and 580V in the right.

6.6.2 Detector Performance

Two main performance characteristics which are tested with cosmic rays are the basic features of the clusters and the efficiency with respect to the applied amplification voltages, the so-called “gain” of the detector.

Cluster Features

The size of the cluster increases when a higher amplification voltage is applied. The trend for the increasing size of the cluster with respect to the amplification voltage is shown in Fig. 6.14(a). The average size of the cluster is also larger for the upper layers. For the two stereo layers, the average cluster behaviour is similar. The energy of the incident particles is proportional to the cluster charge (sum of the strips’ charge over a cluster, SumQ). Observing the cluster charge over different layers with the same amplification voltage shows how the energy is lost over layers. Fig. 6.14(b) shows the behaviour of the cluster charge for four layers as a function of amplification voltage.

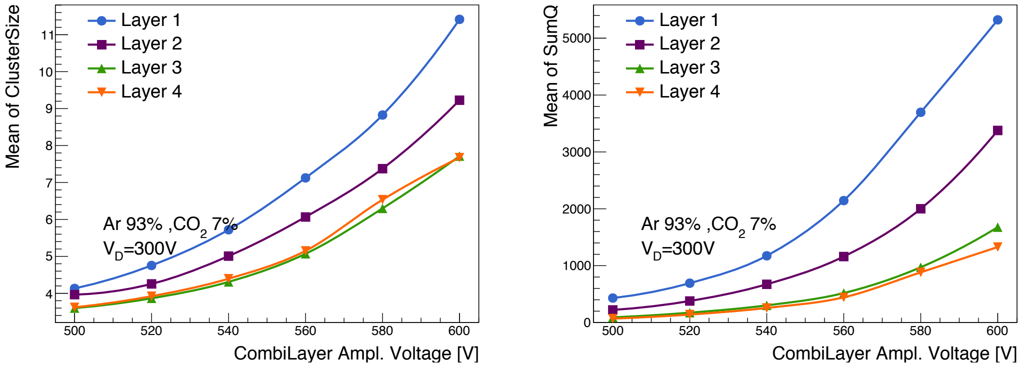

(a) Cluster Size as a function of amplifiaction voltage (b) Cluster Charge as a function of amplification voltage

Figure 6.14: The features of the cluster with different amplification voltages. The higher amplification voltages have bigger cluster sizes and larger cluster charges.

The cluster position is defined as the charge-weighted average position of all strips of the cluster. This definition, strictly speaking, holds true only for perpendicular incoming particles. However, the corresponding systematic uncertainties for incoming particles under different angles can be neglected for the following studies.

The number of clusters as a function of the readout strip position for the four detector layers is shown in Fig. 6.15 for $V_\mathrm{A} = 560\,\mathrm{V}$ and $V_\mathrm{A} = 580\,\mathrm{V}$ with $V_\mathrm{D} = -300\,\mathrm{V}$, respectively. A similar count rate is observed for all layers at $V_\mathrm{A} = 580\,\mathrm{V}$, while the full efficiency for the layers 2-4 is not yet reached at $V_\mathrm{A} = 560\,\mathrm{V}$. The periodic drops feature at the strip ID with multiples of 128 is due to the edge effect of the APV chips.

The increase of the number of clusters with increasing strip number in all four layers is a geometrical effect. About half of the effect comes from the length increase of the readout strips, the other half can be attributed to the efficiency of the scintillators used for triggering. The efficiency of the triggering of the scintillator is shown in Fig. 6.16

Efficiency

To study the efficiency of the prototype detector, three out of the four readout layers are defined as reference layers and the remaining layer as the target

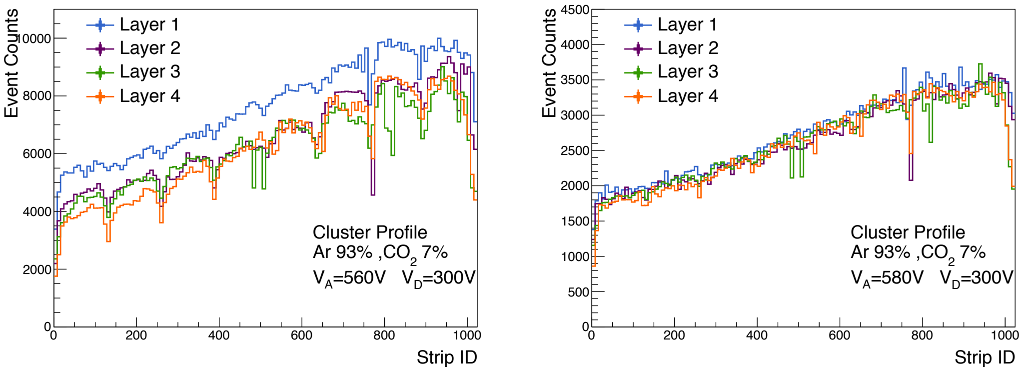

(a) Cluster Profile with 560V (b) Cluster Profile with 580V

Figure 6.15: The cluster profile with four layers and two different amplification voltages. The increase of the number of clusters with increasing strip number in all four layers is a geometrical effect. The efficiency of the scintillators used for triggering also affects the cluster profile.

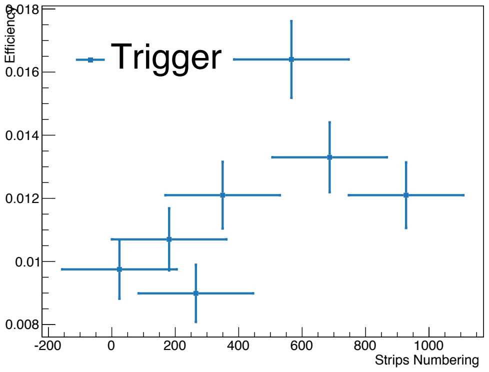

Figure 6.16: The trigger efficiency of the cosmic test stand with the same geometry as the MMSW detector. The trigger is less efficient in the lower strip numbering area. This is due to the aging of the scintillator.

layer. The tight selection which was described in Sec. 6.6.1 is applied on the reference layers to ensure that good clusters are selected to perform the tracking. And the loose selection is applied on the target layer to check that the event is registered. A cluster is defined as correctly reconstructed if its position is within 2.5 mm of the predicted position which is extrapolated from the track of the reference layers.

The dependence of the detector efficiency on the amplification voltage and the efficiency vs. the strip ID for $V_\mathrm{A} = 580\,\mathrm{V}$ is shown in Fig. 6.17. Full efficiency is reached at 560 V for the first layer, at about 570 V for second layer, and at 580 V for the third and fourth layers. For amplification voltages higher than $V_\mathrm{A} = 580\,\mathrm{V}$, the reconstruction efficiency is above 95% for all layers and uniform across all readout strips.

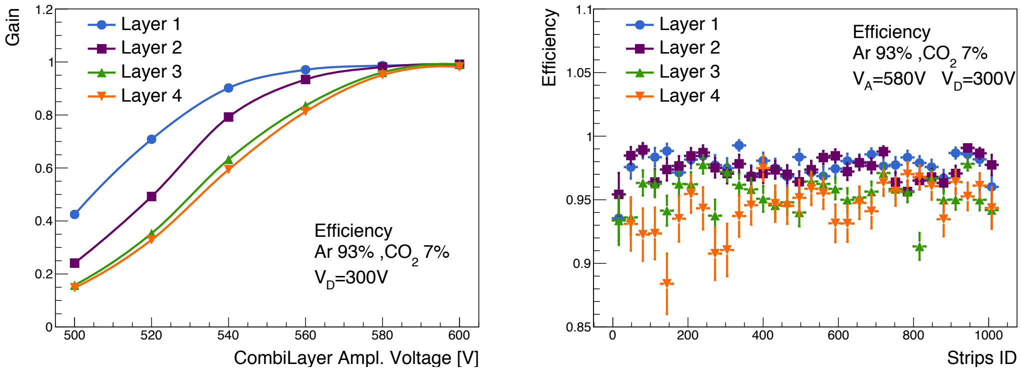

(a) Reconstruction Efficiency as a function of Amplification Voltage

(b) Reconstruction Efficiency with Strip Numbering for 4 Layers

Figure 6.17: The plot on the left shows the reconstruction efficiency of the four detector layers as a function of the amplification voltages. And the plot on the right shows the reconstruction efficiency along the detector with respect to the strips numbering. For amplification voltages higher than 580 V, the reconstruction efficiency is above 95% for all layers and uniform across all readout strips.

The detector efficiency in the fourth layer for $V_\mathrm{A} = 560\,\mathrm{V}$ and $V_\mathrm{A} = 580\,\mathrm{V}$ is shown in a two-dimensional representation of the detector surface in Fig. 6.18. The inefficiencies at the boundaries are the results of inclined strips (28 on the top, and 17 on the bottom), which are shorter at the edge and results in corners which are not covered by the parallel strips. While a higher efficiency is observed in the top part compared to the lower part of the detector for $V_\mathrm{A} = 560\,\mathrm{V}$, a fully homogeneous detector efficiency is found for $V_\mathrm{A} = 580\,\mathrm{V}$.

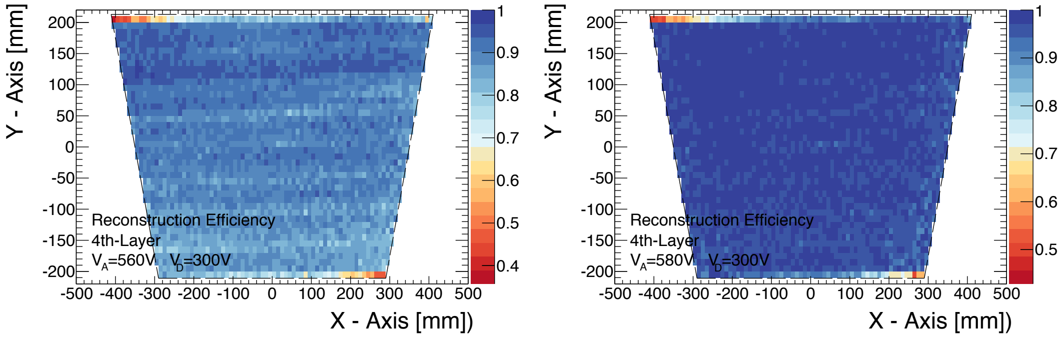

(a) Reconstruction Efficiency with 560V (b) Reconstruction Efficiency with 580V

Figure 6.18: The detector efficiency in the fourth layer for 560 V and 580 V is shown in a two-dimensional representation of the detector surface. The inefficiencies at the boundaries are the results of the inclined strips (28 on the top, and 17 on the bottom), leading to regions that are not covered by both layers of the stereo strips.

6.7 Test-Beam Measurements at MAMI

The performance studies for the resolution of the detector can be well measured with a test beam as it allows a higher energy than cosmic rays and a focused beam for the tracking which can reduce the effect of multiple scattering.

6.7.1 MAMI Test Beam

Test-beam measurements were conducted in August 2014 at the MAMI accelerator facility [66] at the Johannes Gutenberg-University Mainz for a study of the spatial resolution of the MMSW-1 detector. The MAMI accelerator delivers a quasi-continuous electron beam with energies up to 1.5 GeV. For the measurements presented here the beam energy was set to 855 MeV. Following the previous studies, an Ar:CO_2 gas mixture of 93:7 and drift- and amplification voltages of $V_D = -300$ V and $V_A = 550$ V were used. The MMSW detector was placed in several different orientations in order to study its performance for different incident angles of primary particles. A small $10 \times 10\,\text{cm}^2$ micromegas chamber with two-dimensional readout and a spatial resolution of $70\,\mu$m was operated at a distance of 30 cm behind the MMSW detector. Details of this reference chamber are summarized in [73]. This chamber served for reference measurements.

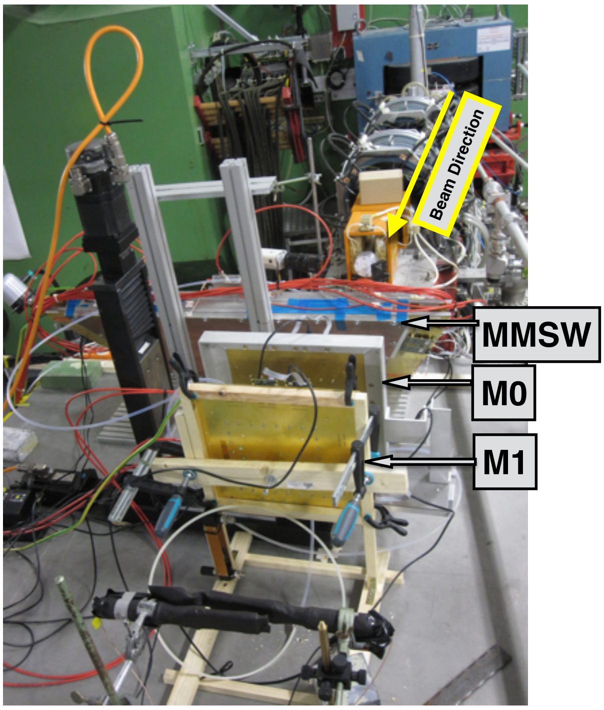

Figure 6.19: The set up for the test at the MAMI accelerator facility.

6.7.2 Detector Performance

The main performance studies for the test beam measurement are the resolution for both coordinates of the prototype detector.

Spatial Resolution

The strip direction of the first and second layer of the MMSW is defined to be the y-axis. The spatial resolution in the x-direction of these two layers can therefore be estimated by comparing the reconstructed position of perpendicular incident particles in both layers on an event-by-event basis. Figure 6.20 shows the difference of the reconstructed track positions in Layers 1 and 2.

The width of the distribution σ_{Diff} is given by

$$\sigma_{\mathrm{Diff}} = \sqrt{\sigma_1^2 + \sigma_2^2 + \sigma_{\mathrm{BD}}^2 + \sigma_{\mathrm{MS}}^2}$$

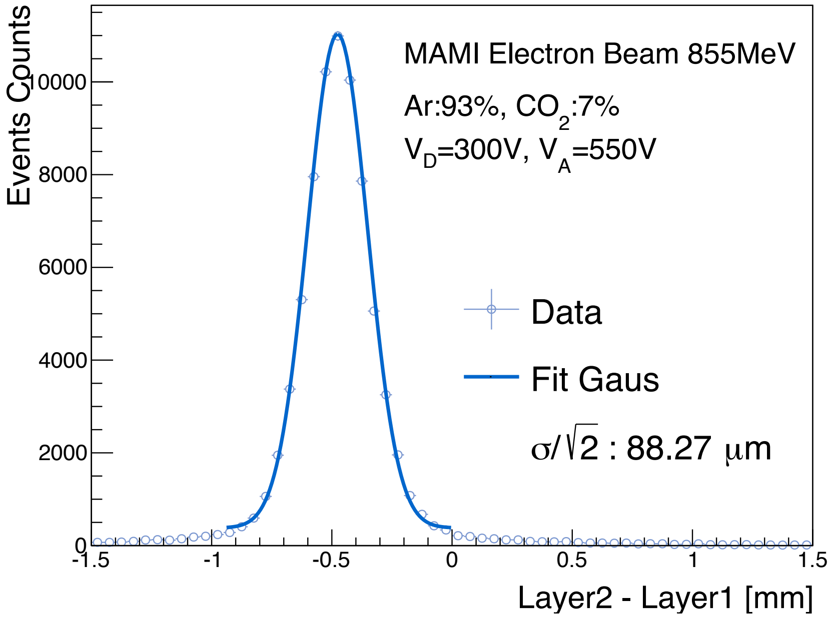

Figure 6.20: The distribution of position difference of same particle track passing through two η layers of the MMSW detector is shown. The sigma of this distribution divided by squared root of the degree of the freedom can be defined as spatial resolution. Spatial resolution of 88 μm in the precision coordinate, which is within the requirements of the ATLAS muon upgrade project.

where σ_i is the spatial resolution of the i-th layer, σ_{MS} is the contribution from multiple-scattering and σ_{BD} the contribution of the beam divergence. The offset of the observed distribution is an effect of the chamber orientation with respect to the beam. The contributions to the measured resolution from multiple scattering and the average opening angle of the electron beam are negligible compared to σ_i. The distribution can be described by a gaussian fit. Assuming that the intrinsic resolution is the same for both layers, a spatial core resolution of σ_i^{core} =88 μm is found, which is within the requirements of the ATLAS muon upgrade project.

The strips of the 3rd and 4th layer of the MMSW detector are inclined by $1.5°$ and hence allow for the reconstruction of the y coordinate. The spatial resolution of the y-coordinate measurement via the 3rd- and 4th-layer was estimated via a simultaneous reconstruction of events in the small 10×10 cm reference chamber with two-dimensional readout.

It is essential to subtract the contribution from the multiple scattering as the material between the small reference chambers and the prototype detector for the measurement of the y-coordinate are more than the measurement of the x-coordinate. The contribution from multiple scattering is estimated using several experimental methods which are described below. The small reference chamber (TMM) is needed for this measurement, which is a two-dimensional readout chamber using Micromegas technology. The difference of the precision coordinate (x-) between TMM and MMSW is used as the resolution after multiple scattering, as shown in Fig. 6.21(a). And the difference of the precise coordination between reconstructed two stereo layers is the resolution without multiple scattering between two chambers, shown in Fig. 6.21(b). Comparing the two resolutions with and after the multiple scattering subtraction, the resolution is worse by 1.76 mm due to the effects of multiple scattering.

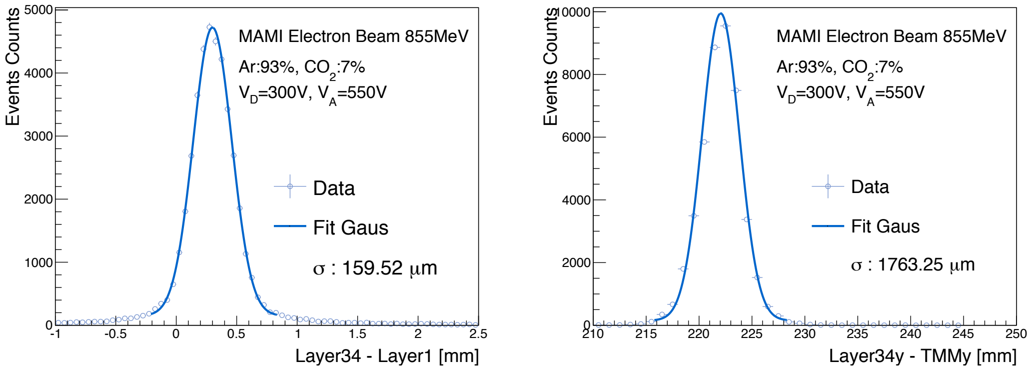

(a) The difference of the position of the reconstructed 3rd + 4th layers and 1st layer

(b) The difference of the position of the TMM and reconstructed 3rd + 4th layers of MMSW

Figure 6.21: Using the TMM reference chamber to estimate the position resolution of the stereo-layers. Multiple scattering estimation from the difference of the precision coordinate within MMSW and between TMM and MMSW. The resolution is worse by 1.76 mm due to the effects of multiple scattering.

The difference in the reconstructed position of the small chamber and the y-position measurement of the MMSW is shown in Fig. 6.22. The width of this distribution has to be corrected for multiple scattering, which has been measured to be $1.76\,$mm, leading to a final y-reconstruction precision of the MMSW chamber of $\sigma_{\mathrm{y}} = 2.3\,$mm. This value is also in accordance with the ATLAS upgrade requirements.

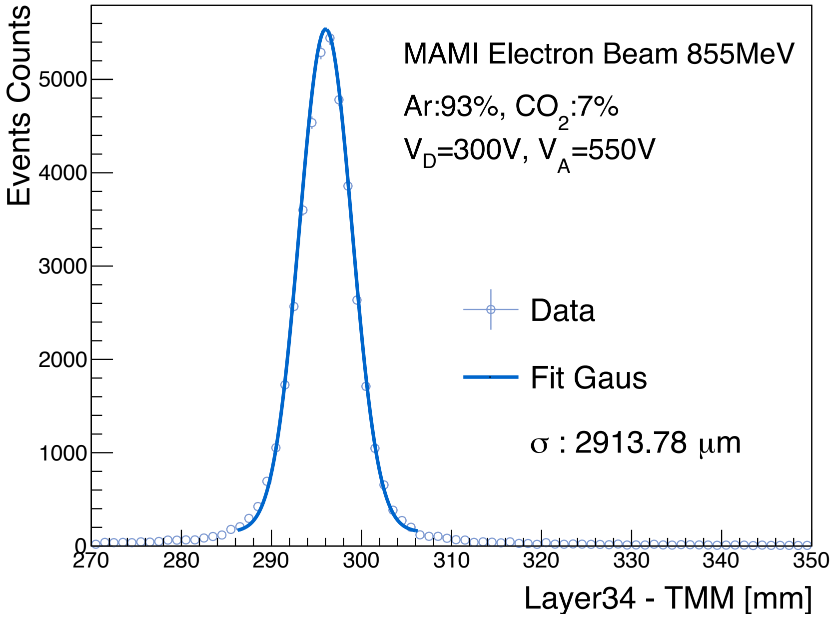

Figure 6.22: Spatial resolution in the pependicular axis of the precision coordinate. The measured width is 2.9 mm. Taking into account multiple scattering, the resulting resolution is 2.3 mm.

6.8 Radiation Hardness Measurements at GIF++

The high luminosity from the upgrade of the LHC will produce a ten times higher particle background for gas-based muon detectors. Therefore it is necessary to test the tolerance, stability and the radiation hardness of the prototype. The aging and the high rate tests can be performed with the new gamma irradiation facility at CERN.

6.8.1 Gamma Irradiation Facility (GIF++)

In the new Gamma Irradiation Facility (GIF++) at CERN [12], detectors can be exposed to the photons from a ^{137}Cs source and to a high-energy muon beam at the same time. The ^{137}Cs isotope will have have only a very small decrease in photon rate over the expected lifetime of GIF++ as its half-life is 30.08 years. The source activity was 13.5 TBq in March 2016. The measurement took place in May 2016. The muon beam is generated

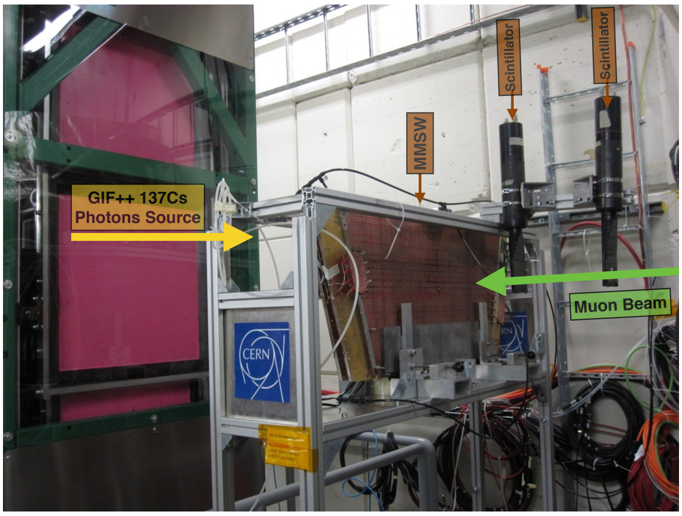

Figure 6.23: The set up for the test at GIF++.

from the decay of pions and kaons produced from the impact of the SPS proton beam on a production target. The spill of the muon beam is in the period of 4.8 seconds and with a maximum momentum of 400 GeV/c. The GIF++ irradiation and its filter systems can deliver 24 different nominal attenuation factors of the irradiation by switching and combining the filters. Photon currents of up to 5×10^7 photons per cm^2 per second are available at a distance of 1m from the source. Between 33% to 54% of the photon current comes from unattenuated photons with an energy of 662 keV. [85]

Nominal Attenuation	Filter Combination	Dose Rate [mGy/h]	Dose Attenuation
1	A1 B1 C1	470.00	-
2.2	A1 B1 C2	211.00	2.2
10	A2 B1 C1	55.00	8.8
100	A3 B1 C1	6.50	72.3

Table 6.1: The measured dose rate and the dose attenuation according to the nominal attenuation with the filter combination of the GIF++[85]

Ten different attenuation factors (0 (source off), 1, 2.2, 5, 10, 22, 69, 100, 220, 2200) were used to test the prototype detector in different high rate environments. The corresponding dose rate is summarized in Tab. 6.1

6.8.2 Detector Performance

The performance for the MMSW prototype detector under different dose rates is shown in Fig. 6.24. The number of the clusters decreases while the photons flux reduces from 10 good clusters per event to two clusters. The average size of the clusters also gets smaller when the photons flux reduces from around 20 strips width to 5 strips. Hence the cluster selection algorithm has to be improved by including track-based information for the future high rate environment.

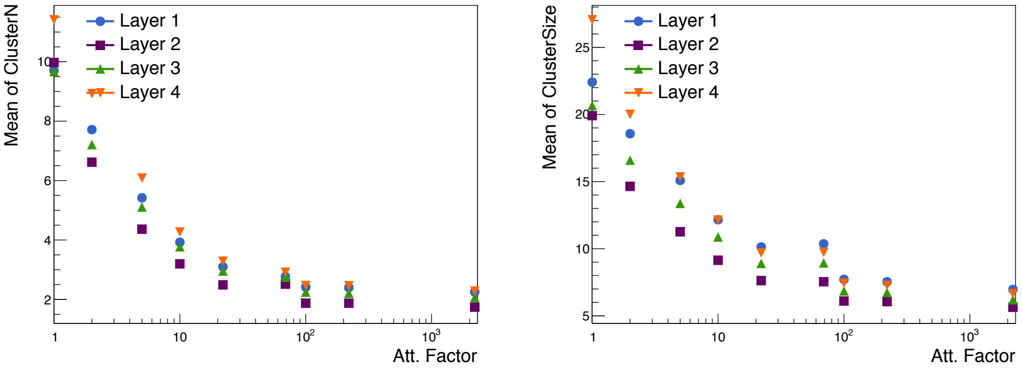

(a) Number of Clusters with Different Attenuation Factors

(b) Size of the Clusters with Different Attenuation Factors

Figure 6.24: The features of the clusters with different attenuation factors in the GIF++ measurement. The higher attenuation gives a smaller clusters size, and fewer clusters.

6.9 MMSW Prototype Tests in the ATLAS Cavern

In order to test the operation of the prototype detector and its readout system in a real high energy experiment, the MMSW prototype detector and its readout system were installed and operated in the ATLAS cavern for testing while the LHC delivered proton-proton collision at $\sqrt{s} = 13$ TeV in October 2016. The data was taken during the ATLAS run 311321 with a centre of energy energy $\sqrt{s} = 13$ TeV proton-proton collisions at the LHC.

The connection scheme for the MMSW prototype detector, its trigger and readout system is shown in Fig. 6.25(a). The prototype detector system

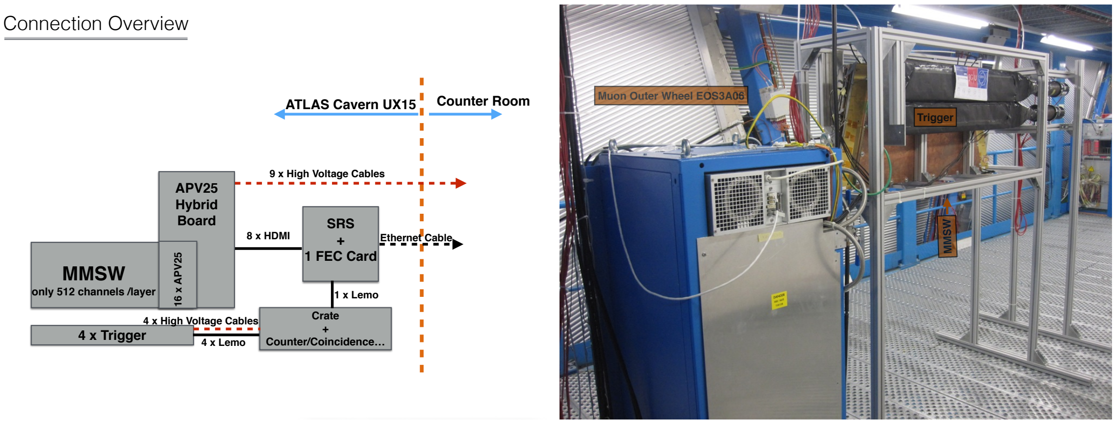

(a) Connection Scheme

(b) MMSW in ATLAS Setup

Figure 6.25: The cable connection and the operation scheme for the prototype test in the ATLAS cavern (left plot). And the set up for the test of MMSW in the ATLAS cavern (right plot).

was installed in the scaffolding structure at the ATLAS cavern wall in the forward direction, seven floors above the beam pipe (ATLAS HO-A7). Muons produced from the collision were expected to hit the prototype detector at 20^o angle with respect to the beam pipe. This incident angle was chosen to optimise the μTPC method which is under development for the angle analysis for the Micromegas detectors.

The MMSW prototype detector was tested in a location 186 cm behind the MDT detectors End-Cap outer wheel (EOS3A06 and EOL3A05) in ATLAS. The MDT occupancy (EOL3A05) during the same time as the data taking of the MMSW prototype detector was about 4 to 5 hits per events per lumiblock. The set up picture of the MMSW prototype tested in the ATLAS cavern is shown in Fig. 6.25(b). The MMSW prototype detector system was operated in the ATLAS cavern for 50 days and was taking data for around 8 hours during stable beam. All analyses which have been performed on the recorded data suggest a stable performance in compliance with the ATLAS requirements.

A simulated muon event is shown in Fig. 6.26 with a track passing through the ATLAS detector and the MMSW prototype detector.

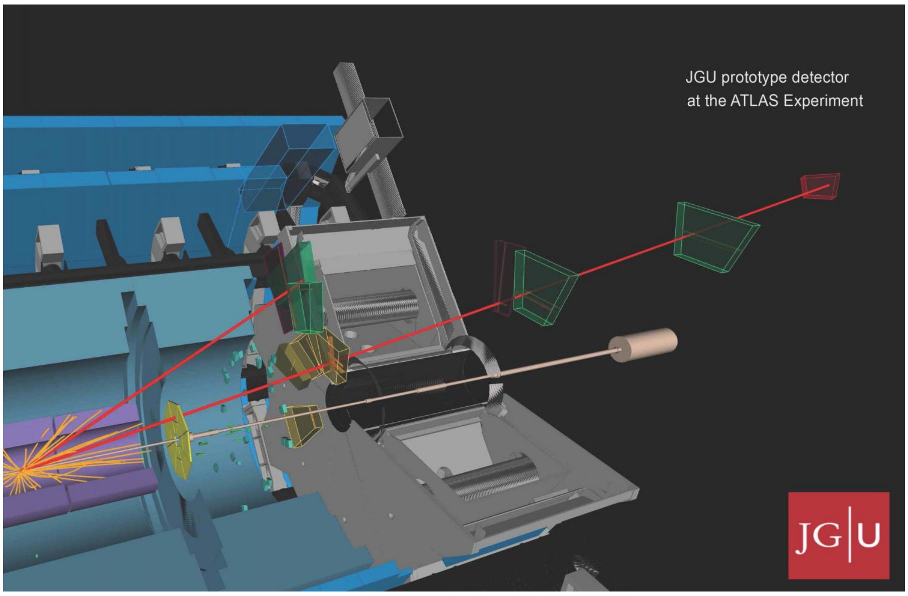

Figure 6.26: A simulated event which with track passing the ATLAS muon detectors and the prototype detector MMSW.[54]

Outlook and Conclusion

7

Within this thesis, several reconstruction algorithms for the hadronic recoil in vector boson events at the LHC have been developed and studied. The track-based transverse momentum (METRefFinal_TST) with optimised jet selection shows a better pile-up independence and response in vector boson events than the cluster-based algorithm (`MET_RefFinal`). The track and cluster associated method also provides stable response and good resolution. Further study of the systematic uncertainties is needed for it to be used in the physics analysis.

The measurement of the muon charge asymmetry from the W boson in proton-proton collisions at a centre of mass energy of 8 TeV is based on an integrated luminosity $L = 20.3\text{fb}^{-1}$ of data recorded with the ATLAS detector at the LHC. The fiducial cross sections are measured to be:

- $W^+ \rightarrow \mu^+\nu : \sigma_{\text{fid}}[pb] = 3189.55 \pm 0.50(\text{stat.}) \pm 32.72(\text{syst.}) \pm 66.78(\text{lumi.})$
- $W^- \rightarrow \mu^-\bar{\nu} : \sigma_{\text{fid}}[pb] = 2189.85 \pm 0.42(\text{stat.}) \pm 21.48(\text{syst.}) \pm 47.07(\text{lumi.})$

The theoretical prediction which is compared with the measured data is from the “PowhegPythia8” event generator using the CT10 PDF sets. The measured data and prediction of W boson fiducial cross section are in a good agreement.

The overall muon charge asymmetry of the production of W bosons in proton proton collisions at a centre of mass energy of 8 TeV is measured to be:

- $\text{A}_\mu = 0.18263 \pm 0.00147(\text{syst.}) \pm 0.00021(\text{stat.})$

The high experimental precision of this observable is achieved by the cancellation of several systematic uncertainties in the ratio and hence provide a unique probe of the parton density functions of the proton.

The construction of two detectors based on the Micromegas technology in view of the ATLAS Muon Upgrade projects has been described. It should serve as a starting point for similar detector developments in the future. Each detector has an active area of $0.3\,\mathrm{m}^2$ and four planes of one-dimensional Micromegas readout structures. In two of the four planes the readout strips form a stereo angle of $\pm 1.5^{\circ}$, allowing for the measurement of a second coordinate. Difficulties during the construction of the first detector, have been addressed and improved for the second version.

First performance measurements based on cosmic rays and test beam measurements at the MAMI accelerator give results consistent with the ATLAS Muon System requirements. The response of the detector, operated with an Ar:CO_2 gas mixture, for different amplification voltages has been studied. An average signal reconstruction efficiency of $\geq$98% per layer was found for an amplification voltage V_A $\geq$580 V, homogeneous across the full detector. The intrinsic spatial resolution was determined in an electron beam of 855 MeV to be better than $100\,\mu\mathrm{m}$ in the precision coordinate and 2.3 mm in the second coordinate.

The high rate tests were performed with GIF++ to test the behaviour of the basic cluster features and its tracking algorithm. The installation of one of the prototype detectors in the ATLAS experiment has proved the stability of the readout and data taking of the prototype detector in realistic operating conditions.

In summary, the developed prototype detector built a suitable basis for the ATLAS NSW Upgrade project. Once the upgrade project is successfully completed in 2020, it will allow for further high precision measurements of the W boson production during the high-luminosity phase of the LHC.

References

[1]„A Measurement of WZ Production in Proton-Proton Collisions at $\sqrt{s}$=8 TeV with the ATLAS Detector“. In: (2013) (cit. on p. 32).

[2]Georges Aad et al. „Measurement of the $t\bar{t}$ production cross-section using $e\mu$ events with b-tagged jets in pp collisions at $\sqrt{s}$ = 7 and 8 TeV with the ATLAS detector“. In: *Eur. Phys. J.* C74.10 (2014). [Addendum: Eur. Phys. J.C76,no.11,642(2016)], p. 3109. arXiv: `1406.5375 [hep-ex]` (cit. on p. 32).

[3]Georges Aad et al. „Observation and measurement of Higgs boson decays to WW* with the ATLAS detector“. In: *Phys. Rev.* D92.1 (2015), p. 012006. arXiv: `1412.2641 [hep-ex]`.

[4]Roel Aaij et al. „Observation of $J/\psi\phi$ structures consistent with exotic states from amplitude analysis of $B^+ \to J/\psi\phi K^+$ decays“. In: *Phys. Rev. Lett.* 118.2 (2017), p. 022003. arXiv: `1606.07895 [hep-ex]` (cit. on p. 4).

[5]T. Aaltonen et al. „Search for Standard Model Higgs Boson Production in Association with a W Boson Using a Matrix Element Technique at CDF in $p\bar{p}$ Collisions at $\sqrt{s} = 1.96$ TeV“. In: *Phys. Rev.* D85 (2012), p. 072001. arXiv: `1112.4358 [hep-ex]` (cit. on p. 68).

[6]D. Acosta et al. „Measurements of $b\bar{b}$ azimuthal production correlations in $p\bar{p}$ collisions at $\sqrt{s} = 1.8$ TeV“. In: *Phys. Rev.* D71 (2005), p. 092001. arXiv: `hep-ex/0412006 [hep-ex]` (cit. on p. 72).

[7]S. Agostinelli et al. „GEANT4: A Simulation toolkit“. In: *Nucl. Instrum. Meth. Phys. Res.* A506 (2003), pp. 250–303 (cit. on p. 30).

[8]T. Alexopoulos, J. Burnens, R. de Oliveira, et al. „A spark-resistant bulk-micromegas chamber for high-rate applications“. In: *Nucl. Instrum. Meth.* A640 (2011), pp. 110–118 (cit. on p. 104).

[9]Simone Alioli, Paolo Nason, Carlo Oleari, and Emanuele Re. „A general framework for implementing NLO calculations in shower Monte Carlo programs: the POWHEG BOX“. In: *JHEP* 06 (2010), p. 043. arXiv: `1002.2581 [hep-ph]` (cit. on pp. 11, 30).

[10] Simone Alioli, Paolo Nason, Carlo Oleari, and Emanuele Re. „NLO vector-boson production matched with shower in POWHEG“. In: *JHEP* 0807 (2008), p. 060. arXiv: `0805.4802 [hep-ph]` (cit. on pp. 11, 30).

[11] Nansi Andari, Jean-Baptiste Blanchard, Maarten Boonekamp, et al. „Measurement of m_W with 7 TeV data: W boson mass measurement“. In: ATL-COM-PHYS-2014-1569 (2014) (cit. on pp. 1, 69, 73).

[12] G Apollinari, I Béjar Alonso, O Brüning, M Lamont, and L Rossi. „High-Luminosity Large Hadron Collider (HL-LHC) : Preliminary Design Report“. In: (2015) (cit. on p. 123).

[13] ATLAS Collaboration. „ATLAS Metadata Interface“. In: *ATLAS-AMI* (2017) (cit. on p. 32).

[14] ATLAS Collaboration. „ATLAS Twiki: Extended Pileup Reweighting“. In: *ATLAS-Twiki* (2016) (cit. on p. 75).

[15] ATLAS Collaboration. „Data Preparation Check List For Physics Analysis“. In: *ATLAS-Twiki* (2013) (cit. on p. 62).

[16] ATLAS Collaboration. „EGamma Analysis Tool“. In: *ATLAS-SVN* (2013) (cit. on pp. 52, 75).

[17] ATLAS Collaboration. „HowToCleanJets2011“. In: *ATLAS-Twiki* (2013) (cit. on p. 63).

[18] ATLAS Collaboration. „Jet Energy Scale Tool“. In: *ATLAS-SVN* (2015) (cit. on p. 26).

[19] ATLAS Collaboration. „Measurement of the forward-backward asymmetry of electron and muon pair-production in pp collisions at $\sqrt{s} = 7$ TeV with the ATLAS detector“. In: *JHEP* 09 (2015), p. 049. arXiv: `1503.03709 [hep-ex]` (cit. on p. 73).

[20] ATLAS Collaboration. „Measurement of the muon reconstruction performance of the ATLAS detector using 2011 and 2012 LHC protonâproton collision data“. In: *Eur. Phys. J.* C74.11 (2014), p. 3130. arXiv: `1407.3935 [hep-ex]` (cit. on pp. 79, 87).

[21] ATLAS Collaboration. „Measurement of the transverse momentum and ϕ^*_η distributions of Drell–Yan lepton pairs in proton–proton collisions at $\sqrt{s} = 8$ TeV with the ATLAS detector“. In: *Eur. Phys. J.* C76.5 (2016), p. 291. arXiv: `1512.02192 [hep-ex]` (cit. on pp. 68, 69).

[22] ATLAS Collaboration. „Measurement of the W charge asymmetry in the $W \to \mu\nu$ decay mode in pp collisions at $\sqrt{s} = 7$ TeV with the ATLAS detector“. In: *Phys. Lett.* B701 (2011), pp. 31–49. arXiv: `1103.2929 [hep-ex]` (cit. on pp. 59, 83).

[23]ATLAS Collaboration. „Muon Combined Performance Analysis Guidelines 2012“. In: *ATLAS-Twiki* (2013) (cit. on pp. 26, 27).

[24]ATLAS Collaboration. „Muon Efficiency Corrections Tool“. In: *ATLAS-SVN* (2014) (cit. on p. 79).

[25]ATLAS Collaboration. „Muon Momentum Corrections Tool“. In: *ATLAS-SVN* (2014) (cit. on pp. 52, 77).

[26]ATLAS Collaboration. „Muon Trigger Physics Trigger Recommendations 2012“. In: *ATLAS-Twiki* (2013) (cit. on pp. 64, 72, 75).

[27]ATLAS Collaboration. „Muons: release 17.2 and beyond“. In: *ATLAS-Twiki* (2013) (cit. on p. 64).

[28]ATLAS Collaboration. „Performance of missing transverse momentum reconstruction in ATLAS studied in proton-proton collisions recorded in 2012 at 8 TeV“. In: *ATLAS-CONF-2013-082* (2013) (cit. on pp. 46, 88).

[29]ATLAS Collaboration. „Supporting document on electron performance measurements using the 2011 LHC proton-proton collisions“. In: ATL-COM-PHYS-2012-1023 (2012) (cit. on p. 86).

[30]ATLAS Collaboration. „Technical Design Report for the ATLAS Inner Tracker Strip Detector“. In: CERN-LHCC-2017-005. ATLAS-TDR-025 (2017) (cit. on p. 18).

[31]ATLAS Collaboration. „The ATLAS Simulation Infrastructure“. In: *Eur. Phys. J.* C70 (2010), pp. 823–874. arXiv: `1005.4568 [physics.ins-det]` (cit. on p. 30).

[32]ATLAS Collaboration. „Top Group MC12 Common Conventions“. In: *ATLAS-Twiki* (2015).

[33]K Bachas, M Bellomo, F BÃŒhrer, et al. „Measurement and QCD Analysis of Differential Inclusive W+- -> lnu and Z/gamma* -> ll Production and Leptonic Decay Cross Sections with ATLAS“. In: ATL-COM-PHYS-2013-217 (2012).

[34]K Bachas, M Bellomo, F BÃŒhrer, et al. „Measurement and QCD Analysis of Differential Inclusive W+- → lnu and Z/gamma* → ll Production and Leptonic Decay Cross Sections with ATLAS: Analysis STDM-2012-20: W and Z inclusive cross section with 2011 data“. In: ATL-COM-PHYS-2013-217 (2012) (cit. on p. 11).

[35]Massimiliano Bellomo, Felix Buehrer, Stefano Camarda, et al. „Precision measurement and interpretation of inclusive W^+, W^- and Z/γ^* production cross sections with the ATLAS detector: Paper draft for the W,Z 2011 inclusive cross section analysis“. In: ATL-COM-PHYS-2016-818 (2016). Support note https://cds.cern.ch/record/1517987 (cit. on p. 86).

[36]C. F. Berger, Z. Bern, Lance J. Dixon, et al. „Precise Predictions for W + 4 Jet Production at the Large Hadron Collider“. In: *Phys. Rev. Lett.* 106 (2011), p. 092001. arXiv: `1009.2338 [hep-ph]`.

[37]M. Bianco, S. Martoiu, O. Sidiropoulou, and A. Zibell. „Development and test of the DAQ system for a Micromegas prototype to be installed in the ATLAS experiment“. In: *Journal of Physics: Conference Series* 664.8 (2015), p. 082056.

[38]R. K. Bock. „Data analysis techniques for high-energy physics experiments“. In: *Camb. Monogr. Part. Phys. Nucl. Phys. Cosmol.* 11 (2000). Ed. by H. Grote, D. Notz, and M. Regler, pp. 1–434 (cit. on p. 22).

[39]Andy Buckley et al. „General-purpose event generators for LHC physics“. In: *Phys. Rept.* 504 (2011), pp. 145–233. arXiv: `1101.2599 [hep-ph]` (cit. on p. 12).

[40]Andy Buckley, James Ferrando, Stephen Lloyd, et al. „LHAPDF6: parton density access in the LHC precision era“. In: *Eur. Phys. J.* C75 (2015), p. 132. arXiv: `1412.7420 [hep-ph]` (cit. on p. 98).

[41]J.M. Butterworth, Jeffrey R. Forshaw, and M.H. Seymour. „Multiparton interactions in photoproduction at HERA“. In: *Z. Phys.* C72 (1996), pp. 637–646. arXiv: `hep-ph/9601371 [hep-ph]` (cit. on p. 30).

[42]Matteo Cacciari, Gavin P. Salam, and Gregory Soyez. „The Anti-k(t) jet clustering algorithm“. In: *JHEP* 04 (2008), p. 063. arXiv: `0802.1189 [hep-ph]` (cit. on pp. 26, 52).

[43]Stefano Catani, Leandro Cieri, Giancarlo Ferrera, Daniel de Florian, and Massimiliano Grazzini. „Vector boson production at hadron colliders: a fully exclusive QCD calculation at NNLO“. In: *Phys. Rev. Lett.* 103 (2009), p. 082001. arXiv: `0903.2120 [hep-ph]` (cit. on p. 97).

[44]M. Chefdeville. „RD51, a world-wide collaboration for the development of micro pattern gaseous detectors“. In: *J. Phys. Conf. Ser.* 309 (2011), p. 012017 (cit. on p. 113).

[45]CMS Collaboration. „Introduction to physics objects“. In: *CMS-Lecture* (2012) (cit. on p. 24).

[46]ATLAS Collaboration. „Expected performance of the ATLAS experiment: detector, trigger and physics“. In: (2009) (cit. on p. 17).

[47]ATLAS Collaboration. „Measurement of the muon reconstruction performance of the ATLAS detector using 2011 and 2012 LHC proton–proton collision data“. In: *Eur. Phys. J. C* 74.arXiv:1407.3935. CERN-PH-EP-2014-151 (2014), 3130. 34 p.

[48]ATLAS Collaboration. „Observation of a new boson at a mass of 125 GeV with the CMS experiment at the LHC“. In: *Phys. Lett. B* 716 (2012), p. 30 (cit. on p. 25).

[49]ATLAS Collaboration. „The ATLAS Experiment at the CERN Large Hadron Collider“. In: *JINST* 3 (2008). Also published by CERN Geneva in 2010, S08003. 437 p (cit. on pp. 14, 16–21, 23, 24).

[50]The ATLAS collaboration. „Measurement of the W^+W^- production cross section in proton-proton collisions at $\sqrt{s} = 8$ TeV with the ATLAS detector“. In: (2014).

[51]G. Corcella, I.G. Knowles, G. Marchesini, S. Moretti, K. Odagiri, et al. „HERWIG 6: An Event generator for hadron emission reactions with interfering gluons (including supersymmetric processes)“. In: *JHEP* 0101 (2001), p. 010. arXiv: `hep-ph/0011363 [hep-ph]` (cit. on p. 30).

[52]Sidney D Drell and Tung-Mow Yan. „Partons and their applications at high energies“. In: *Annals of Physics* 66.2 (1971), pp. 578 –623 (cit. on p. 6).

[53]Manolis Dris and Theo Alexopoulos. „Signal Formation in Various Detectors“. In: (2014). arXiv: `1406.3217 [hep-ex]` (cit. on p. 104).

[54]Andreas Duedder. „ATLAS New Small Wheel Construction and $W \rightarrow \nu + \tau$ branch ratio at ATLAS detector at LHC“. In: (2018). will be written in 2018 (cit. on p. 127).

[55]Sayipjamal Dulat, Tie-Jiun Hou, Jun Gao, et al. „New parton distribution functions from a global analysis of quantum chromodynamics“. In: *Phys. Rev.* D93.3 (2016), p. 033006. arXiv: `1506.07443 [hep-ph]` (cit. on p. 10).

[56]Ed Daw. „Rapidity and Pseudorapidity“. In: *ATLAS-Lecture* (2012) (cit. on p. 15).

[57]L.R. Evans. *The Large Hadron Collider: A Marvel of Technology*. Fundamental sciences. Taylor & Francis Group, 2009 (cit. on pp. 17, 22).

[58]Stefano Forte, Lluis Garrido, Jose I. Latorre, and Andrea Piccione. „Neural network parametrization of deep inelastic structure functions“. In: *JHEP* 05 (2002), p. 062. arXiv: `hep-ph/0204232 [hep-ph]` (cit. on p. 10).

[59]Stefano Frixione and Bryan R. Webber. „Matching NLO QCD computations and parton shower simulations“. In: *JHEP* 0206 (2002), p. 029. arXiv: `hep-ph/0204244 [hep-ph]` (cit. on p. 30).

[60]Jun Gao, Marco Guzzi, Joey Huston, Hung-Liang Lai, Zhao Li, et al. „CT10 next-to-next-to-leading order global analysis of QCD“. In: *Phys. Rev.* D89 (2014), p. 033009. arXiv: `1302.6246 [hep-ph]` (cit. on p. 10).

[61]T. Gleisberg, Stefan. Hoeche, F. Krauss, M. Schonherr, S. Schumann, et al. „Event generation with SHERPA 1.1“. In: *JHEP* 0902 (2009), p. 007. arXiv: `0811.4622 [hep-ph]` (cit. on p. 30).

[62]Robert Scot Hickling and Eram Rizvi. „Measuring the Drell-Yan Cross Section at High Mass in the Dimuon Channel“. In: (2014). Presented 12 Nov 2014 (cit. on p. 75).

[63] Georgios Iakovidis, Theodoros Alexopoulos, Sandro Palestini, et al. „Stereo Information in Micromegas Detectors“. In: ATL-COM-MUON-2015-044 (2015). ATL-MUON-PUB-2015-001 (cit. on p. 106).

[64] Paolo Iengo et al. „Construction of a large-size four plane micromegas detector“. In: *PoS* TIPP2014 (2014), p. 058 (cit. on p. 107).

[65] Jan Kretzschmar. „PDF fits and precision W and Z at LHC“. In: *xFitter External Meeting in Oxford* (2017) (cit. on p. 97).

[66] K. H. Kaiser et al. „The 1.5-GeV harmonic double-sided microtron at Mainz University“. In: *Nucl. Instrum. Meth.* A593 (2008), pp. 159–170 (cit. on p. 119).

[67] T Kawamoto, S Vlachos, L Pontecorvo, et al. „New Small Wheel Technical Design Report“. In: CERN-LHCC-2013-006. ATLAS-TDR-020 (2013). ATLAS New Small Wheel Technical Design Report (cit. on p. 102).

[68] David Khatidze. „The Charge Asymmetry in W Bosons Production in pp Collisions at the $\sqrt{s} = 1.96$ TeV using the D0 Detector at the Fermilab Tevatron“. 2009. PhD thesis. COLUMBIA UNIVERSITY, 2009 (cit. on p. 11).

[69] Hung-Liang Lai, Marco Guzzi, Joey Huston, et al. „New parton distributions for collider physics“. In: *Phys. Rev.* D82 (2010), p. 074024. arXiv: `1007.2241 [hep-ph]`.

[70] W Lampl, S Laplace, D Lelas, et al. „Calorimeter Clustering Algorithms: Description and Performance“. In: ATL-LARG-PUB-2008-002. ATL-COM-LARG-2008-003 (2008) (cit. on pp. 26, 42).

[71] „LHC Guide“. 2017 (cit. on p. 13).

[72] Tai-Hua Lin, Paolo Iengo, Matthias Schott, Michele Bianco, et al. „Construction of two large-size four-plane micromegas detectors“. In: *Nucl. Instrum. Meth.* A814 (2016), pp. 117–130. arXiv: `1511.03884 [physics.ins-det]` (cit. on pp. 2, 107).

[73] Tai-Hua Lin, Andreas Duedder, Matthias Schott, et al. „Signal Characteristics of a Resistive-Strip Micromegas Detector with an Integrated Two-Dimensional Readout“. In: *Nucl. Instrum. Meth.* A767 (2014), pp. 281–288. arXiv: `1406.6871 [physics.ins-det]` (cit. on pp. 103, 104, 119).

[74] L.Jones et al. „The APV25 deep sub Micron readout chip for CMS channels detectors“. In: *Proceedings of 5th workshop on Chips electronics for LHC experiments* CERN/LHCC/99-09 (1999), pp. 162–166 (cit. on p. 110).

[75] A. D. Martin, W. J. Stirling, R. S. Thorne, and G. Watt. „Parton distributions for the LHC“. In: *Eur. Phys. J.* C63 (2009), pp. 189–285. arXiv: `0901.0002 [hep-ph]` (cit. on pp. 9, 10).

[76] Alan D. Martin, R. G. Roberts, W. James Stirling, and R. S. Thorne. „Parton distributions and the LHC: W and Z production“. In: *Eur. Phys. J.* C14 (2000), pp. 133–145. arXiv: `hep-ph/9907231 [hep-ph]` (cit. on p. 7).

[77] Verena Ingrid Martinez Outschoorn and J Guimaraes da Costa. „Measurement of the Charge Asymmetry of W Bosons Produced in pp Collisions at $\sqrt{s} = 7$ TeV with the ATLAS Detector“. Presented 19 May 2011. 2011 (cit. on pp. 6, 10).

[78] Verena Ingrid Martinez Outschoorn and J Guimaraes da Costa. „Measurement of the Charge Asymmetry of W Bosons Produced in pp Collisions at $\sqrt{s} = 7$ TeV with the ATLAS Detector“. Presented 19 May 2011. PhD thesis. Cambridge, MA, USA: Harvard U., 2011 (cit. on pp. 68, 99).

[79] S. Martoiu, H. Muller, A. Tarazona, and J. Toledo. „Development of the scalable readout system for micro-pattern gas detectors and other applications“. In: *JINST* 8 (2013), p. C03015 (cit. on p. 110).

[80] S. Martoiu, H. Muller, and J. Toledo. „Front-end electronics for the Scalable Readout System of RD51“. In: *IEEE Nucl. Sci. Symp. Conf. Rec.* 2011 (2011), pp. 2036–2038 (cit. on p. 110).

[81] „Measurement of the total ZZ production cross section in proton-proton collisions at $\sqrt{s} = 8$ TeV in 20 fb$^{-}1$ with the ATLAS detector“. In: (2013) (cit. on p. 32).

[82] E J W Moyse. „Muon identification for the ATLAS experiment“. In: (2009) (cit. on pp. 21, 22).

[83] C. Patrignani et al. „Review of Particle Physics“. In: *Chin. Phys.* C40.10 (2016), p. 100001 (cit. on pp. 11, 77).

[84] E. Perez and E. Rizvi. „The Quark and Gluon Structure of the Proton“. In: *Rept. Prog. Phys.* 76 (2013), p. 046201. arXiv: `1208.1178 [hep-ex]` (cit. on p. 5).

[85] Dorothea Pfeiffer, Georgi Gorine, Hans Reithler, et al. „The radiation field in the Gamma Irradiation Facility GIF++ at CERN“. In: (2016). arXiv: `1611.00299 [physics.ins-det]` (cit. on pp. 102, 124).

[86] Juan Rojo et al. „The PDF4LHC report on PDFs and LHC data: Results from Run I and preparation for Run II“. In: *J. Phys.* G42 (2015), p. 103103. arXiv: `1507.00556 [hep-ph]` (cit. on p. 92).

[87] Thomas Schoerner-Sadenius. „The Large Hadron Collider: Harvest of Run 1“. In: *Springer International Publishing Cham* (2015) (cit. on p. 11).

[88] Matthias Schott and Monica Dunford. „Review of single vector boson production in pp collisions at $\sqrt{s} = 7$ TeV“. In: *Eur. Phys. J.* C74 (2014), p. 2916. arXiv: `1405.1160 [hep-ex]` (cit. on pp. 6, 9).

[89] Steven Schramm. „Searching for Dark Matter with the ATLAS Detector in Events with an Energetic Jet and Large Missing Transverse Momentum“. PhD thesis. Toronto U., 2015-03-15 (cit. on p. 25).

[90] Torbjorn Sjöstrand, Stephen Mrenna, and Peter Z. Skands. „A Brief Introduction to PYTHIA 8.1“. In: *Comput. Phys. Commun.* 178 (2008), pp. 852–867. arXiv: `0710.3820 [hep-ph]` (cit. on pp. 11, 30).

[91] Torbjorn Sjöstrand, Stephen Mrenna, and Peter Z. Skands. „PYTHIA 6.4 Physics and Manual“. In: *JHEP* 0605 (2006), p. 026. arXiv: `hep-ph/0603175 [hep-ph]` (cit. on p. 30).

[92] Helmuth Spieler. *Semiconductor detector systems*. Semiconductor Science and Technology. Oxford: Oxford Univ. Press, 2005 (cit. on p. 17).

[93] „Stereo Information in Micromegas Detectors“. In: ATL-MUON-PUB-2015-001 (2015) (cit. on p. 105).

[94] Mark Thomson. „Modern Particle Physics“. In: *Cambridge University Press* (2013) (cit. on pp. 3, 8).

[95] Ulrik Egede. „Pattern recognition in the Inner Detector“. In: *ATLAS-Thesis* (1998) (cit. on pp. 15, 25).

[96] NGUYEN Thi Hong Van. „Mesure la distribution en impulsion transverse du boson W avec le detecteur ATLAS au LHC“. Presented 9 Sept 2011. PhD thesis. CEA Saclay: Universite Paris Diderot, 2011 (cit. on pp. 8, 9, 34, 56).

[97] Samuel Nathan Webb. „Factorisation of beams in van der Meer scans and measurements of the ϕ^*_η distribution of $Z \rightarrow e^+e^-$ events in pp collisions at $\sqrt{s} = 8$ TeV with the ATLAS detector“. In: (2015-06-01) (cit. on p. 25).

[98] „Wikipedia: Standard Model“. In: (2017) (cit. on pp. 3, 4).

[99] C. Zeitnitz and T. A. Gabriel. „The GEANT - CALOR interface and benchmark calculations of ZEUS test calorimeters“. In: *Nucl. Instrum. Meth.* A349 (1994), pp. 106–111 (cit. on p. 102).

List of Figures

List of Tables

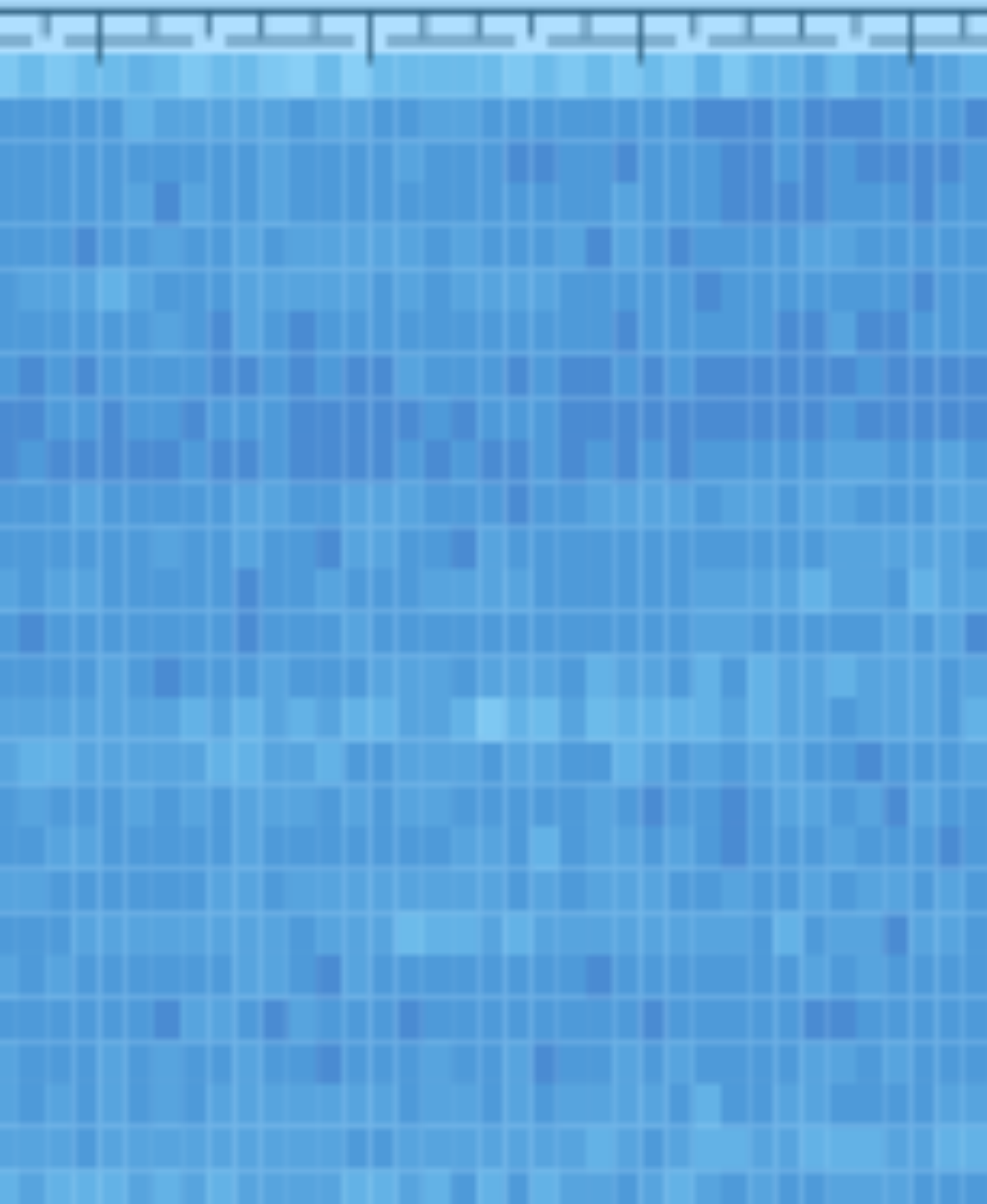

Dissertation
zur Erlangung des akademischen Grades doctor rerum naturalium (Dr. rer. nat.)
im Fach Physik an der
Johannes Gutenberg-Universität Mainz
von
Tai-Hua Lin